A Two Dimensional Speckle Tracking Method Based on Zero Phase Crossing in Ultrasound

A DISSERTATION
SUBMITTED TO THE FACULTY OF THE GRADUATE SCHOOL
OF THE UNIVERSITY OF MINNESOTA
BY

Fei Zheng

IN PARTIAL FULFILLMENT OF THE REQUIREMENTS
FOR THE DEGREE OF
DOCTOR OF PHILOSOPHY

Dr. Emad Ebbini, Advisor

May, 2015

Acknowledgements

I would like to express my deepest gratitude to my advisor Professor Emad Ebbini who introduced me to the fascinating field of medical ultrasound imaging. He has been so supportive all through the years in the coursework, research and various professional training for my Ph.D. study. Without him throughout the process, none of these would have been possible.

I am also thankful to Professor Anand Gopinath, Professor Jarvis Haupt, Professor Panos Stinis, Professor Bert Fristedt for serving on my oral exam committee and final defense committee, reviewing my thesis as well as giving helpful comments and suggestions.

I appreciate all the help from many lab colleagues. I would like to thank Yasaman Adibi for her help in data acquisition of a flow phantom with the ultrasound imaging system, Dr. Mahdi Bayat for fabrication of a uniform phantom and setup of the programmed motor, Dr. Andrew Casper for his help of presentation of the poster in Ultrasonic Symposium in 2012, Heng Zhang for his participation in experimental setup, and Dr. Dalong Liu for his helpful discussions and suggestions.

Finally, I am sincerely grateful to my parents who have been always supportive of my study and whose unconditional love motivates me to pursue my dream.

Dedication

To those who held me up over the years

Abstract

Displacement estimation in ultrasound is a common yet important task for various applications, including tissue/blood motion estimation, elastography imaging, temperature estimation, and shear wave elasticity imaging. A variety of speckle tracking methods have been proposed for displacement estimation using pulse-echo ultrasound. The performance of these estimators, in terms of bias and variance, could greatly impact the reliability of the imaging markers derived from the initial displacement estimate. Therefore, a comparison between these methods in a variety of imaging scenarios is highly significant. In addition to considering several published displacement estimation methods, this theses introduces a new estimator based on the complex two-dimensional (2D) cross correlation. The approach builds on the 1D complex cross correlation which results from the analytic nature of pulse-echo ultrasound data in medical imaging applications.

It is well established that the use of complex cross correlation in 1D displacement tracking allows for sub-sample displacement estimation without the need for interpolation. The complex cross correlation is obtained from the Hilbert transform of the echo data and the sub-sample displacement estimate is obtained by using the zero crossing of the phase in the vicinity of the peak in the correlation amplitude. Recently, this property was extended to 2D by exploiting the coupling between the axial and lateral displacements in the phase of the 2D cross correlation of the analytic ultrasound echo data from multiple A-lines. It was theoretically shown that the maximum magnitude of complex correlation still lies on the zero phase line. The so-called "Phase-coupled 2D speckle tracking (PCST) algorithm" was the first to extend the analytic nature of ultrasound data to two dimensions. However, this algorithm applies geometric methods to finding the sub-sample displacements, which may hinder its efficient real-time implementation.

The main contribution of this thesis is the introduction of a new displacement estimator with sub-sample accuracy in both axial and lateral dimensions. A two-dimensional (2D) zero phase crossing method is derived based on two 2D complex normalized cross correlations (NCCs), i.e., displacement can be estimated by the intersection point of two zero phase lines, one from Hilbert transformation in the axial direction and the other one from Hilbert transformation in the lateral direction. Unlike the 2D PCST, the proposed algorithm lends itself to efficient implementation. Furthermore, comparison of simulation results from flow experiments suggests that the new algorithm produces more accurate estimation in terms of variance. The proposed algorithm was compared with the 2D PCST and other displacement estimators proposed by other groups. In particular, we have compared the performance with algorithms based on parabolic and cosine fitting of the 2D correlation of raw 2D radiofrequency (RF) data.

In addition to the validation studies based on simulation, experimental validation of the new algorithm was carried both *in vitro* and *in vivo*. These results suggest that the new algorithm is applicable in realistic medical imaging scenarios where tissue motion and/or flow may be of interest, e.g. imaging atherosclerosis burden in peripheral vessels.

Contents

List of Tables

List of Figures

Chapter 1

Introduction

1.1 Background

Motion tracking is widely used in clinical and research ultrasound [1, 2]. Measurement of properties of tissue, which varies by spatial locations, gives rise to ultrasound imaging. A sequence of images displaying those properties can be acquired along time. With the help of beamforming techniques and contrast agents, better images can be gained. However, bio-mechanical properties of soft tissues cannot be obtained directly from ultrasound images [3, 4]. Motion tracking is widely used to image changes of the mechanical properties, which often indicate an early warning sign of disease, a way of disease detection [5, 6]. Normal and abnormal tissues can be differentiated by, for example, elastography [7–9], which is a technique of estimating the axial strain by using differential displacement of tissue compression [10]. A lot of investigations have been done on elastography in ultrasound in the past two decades. Different techniques have been suggested in the literature to provide these types of images, for instance, Varghese *et al.* [11] proposes a direct strain estimator.

Some ideas of object motion tracking originate from theory of radar during World War II [12]. The idea of motion tracking in medical ultrasound dates back to two decades ago when several researchers started using block matching techniques where a matching function is calculated and motion is found by minimizing or maximizing the matching function [13,14]. Hein *et al.* [15] summarizes some commonly used techniques.

Because of its central significance, accuracy, precision, and computational cost of

motion tracking are of critical importance. In principle, several imaging modalities can be used in order to estimate the tissue motion for elastography but ultrasound has received the most attention due to its portability, safety, low cost, real-time operation, and easy access to digital data, as opposed to magnetic resonance imaging (MRI) [16] and X-ray computed tomography (CT) [17]. Thus, in this dissertation I focus on the estimation of tissue motion from ultrasound echo signals.

1.2 Ultrasound Imaging

Ultrasound imaging uses high-frequency sound waves to view soft tissues such as muscles and internal organs. The imaging performance of a standard ultrasound system relies on several key components, for instance, transmitter waveform design, aperture design and beamforming, pre- or post-beamforming receive filter design and image processing [18]. The transmitted electrical signals, ranging from 1 MHz to 18 MHz, typically produced by a piezoelectric transducer are transformed to acoustic signals and propagated into the imaging field. The common types of real-time transducer arrays are linear arrays, convex arrays and phased arrays. The echoes partially reflected by the target volume propagate back and then is received by the transducer. On the receiver side, the received echoes are transformed back to electrical signals and filtered before receiver beamforming in certain cases, but it is less often than post-beamforming filtering in commercial scanners due to high complexity. Similar to transmitter beamforming, receiving beamformer acts as a spatial-matched filter for signals from different directions. Advanced beamforming techniques exist to increase imaging resolution. The beamformed data is usually filtered by a post-beamforming filter, such as a simple band-pass filter for better imaging performance. After filtering, the received data is post-processed for better image quality with imaging processing techniques, such as decimation or interpolation, log compression, contrast & edge enhancement, speckle reduction, etc. There are several modes of ultrasound in medical imaging [19]. For example, B-mode (brightness mode) image is generated by envelop detection of RF data and then log compression. Doppler mode comes from the Doppler effect in measuring and visualizing blood flow. M-mode (motion mode) is to collect images along time and thus record the motion between transducer and imaged tissues.

1.3 Speckle Tracking Method

1.3.1 One Dimensional Motion Tracking Methods

With a fine resolution in the direction of beam propagation, i.e., axial direction, motion estimation of the axial component has received the most attention. In literature, motion estimation is also referred to as time delay estimation, since the echo signals are collected as a function with time and if we know the speed of sound in the propagation medium, time delay tracking can be transformed to motion tracking [20,21]. There are two typical ways for motion tracking: the Doppler method [22] and the correlation method [23].

The Doppler method is also called phase-shift estimators, which were initially used for blood flow measurement [24, 25]. Doppler equipment aided with the phase-shift technique is commonly used for detecting and evaluating blood flow in arteries and veins. The Doppler frequency is given by [26]:

$$f_D = \frac{2 f_0 v \cos\theta}{c}, \tag{1.1}$$

where f_0 is the transmitted ultrasound frequency, v is the flow velocity, c is the speed of ultrasound in medium and θ is the angle between the transmitted beam and the flow velocity. However accuracy of this method is highly related to the angle measurement and spectral analysis.

The correlation method is an angle-independent flow measurement [13]. As mentioned above, time-delay estimators typically consist of locating the maximum or minimum of a pattern matching function [27,28], depending on the implemented algorithm. The matching algorithm is implemented to find the best match between a pre-defined window in the reference echo signal and the delayed echo signal. Due to the discrete nature of collected data, the estimation error of the pattern matching methods can be as large as half a sample. Several techniques have been explored in the literature to reduce the estimation error [29–32]. Walker and Trahey [2] have extensively developed the standard deviation of the jitter for any unbiased delay estimator based on the work of Carter [12]. The Cramer-Rao Lower Bound is derived in [2]:

$$\sigma(\Delta t - \Delta\hat{t}) = \sqrt{\frac{3}{2 f_0^3 \pi^2 T (B^3 + 12B)} \left(\frac{1}{\rho^2} \left(1 + \frac{1}{\mathrm{SNR}^2} \right)^2 - 1 \right)}, \tag{1.2}$$

where f_0 is the center frequency, T is the window length, B is the fractional bandwidth, ρ is the correlation coefficient to describe signal changes due to physical process and/or transducer non-uniformities and SNR is the signal to noise ratio. This lower bound is the minimum jitter magnitude achievable from any unbiased time delay estimator. Based on this work, Viola *et al.* [33] compares several subsample estimators under various conditions.

One way of reducing estimation error is to up-sample the echo signal [34, 35] or interpolation. Interpolation or function fitting techniques to the echo signals could result in a continuous pattern matching function, whose maximum or minimum determines the location of the best match. These techniques can be computationally demanding, whereas curve or polynomial fitting to the pattern matching function often has significantly smaller computational cost. Thus, even though they may introduce some bias in the estimation process, they are widely used for motion estimation. Techniques including parabolic fitting [36], spline fitting [27], grid slope [37], and cosine fitting [36] have been thoroughly investigated in the literature.

Many 1D pattern matching interpolation methods have been proposed for 1D axial motion estimation with sub-sample accuracy [14, 38]. Performance comparison between these subsample estimators has been studied by several groups [39–45]. Even though there have been a lot of research in this area , improvement still draws the attention of researchers [46, 47].

Figure 1.1 shows commonly used interpolation techniques to achieve subsample accuracy [27,48]. Technique (a) is the base line without any interpolation and only capable of estimating integer shift. Thus it is more prone a large estimation error. The original reference and delays signals are up-sampled and function fitted by Technique (b) and Technique (c), respectively. The difference lies in the fact that Technique (b) is a discrete estimator while Technique (c) is a continuous estimator. Technique (d.1) and Technique (d.2) both choose to fit the correlation function in order to have a continuous estimator. Furthermore, Technique (d.2) incorporates certain up-sampling of original signals to have a finer estimation at the sacrifice of computational cost. In addition to compute cross-correlation between reference and delays signals, Kim *et al.* [49] proposes combining auto-correlation and cross-correlation functions to improve subsample accuracy.

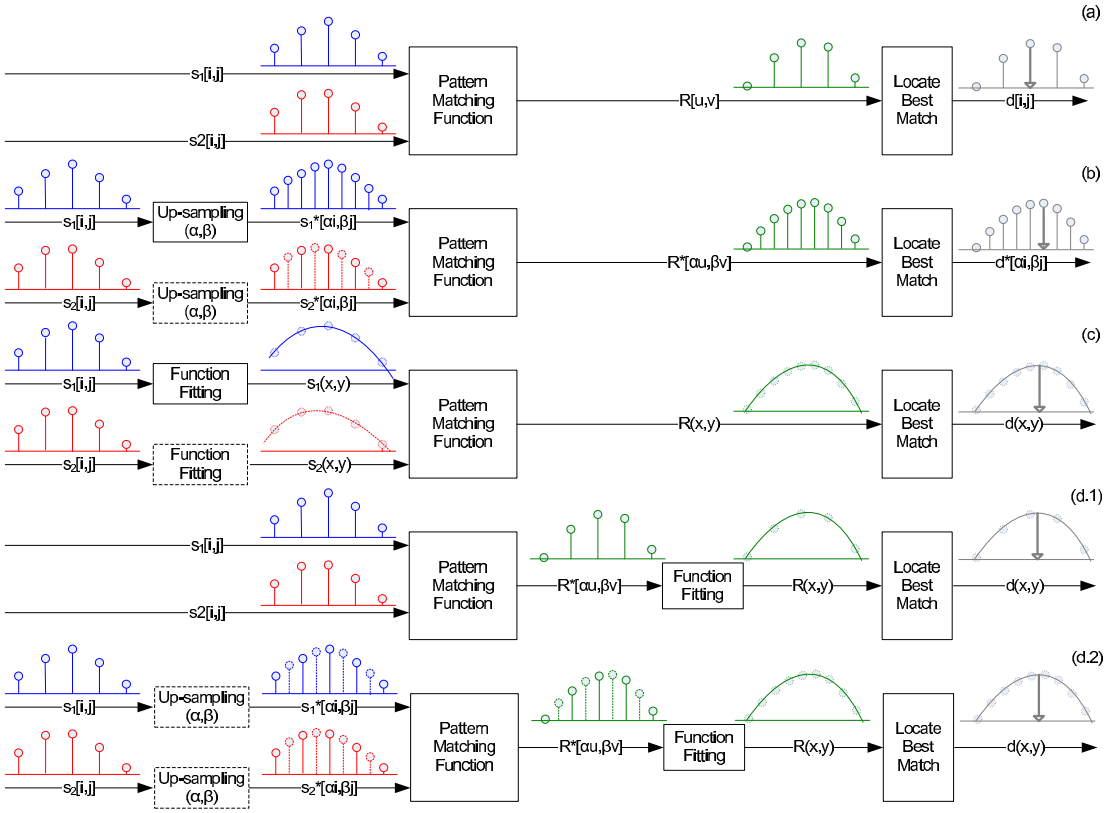

Figure 1.1: Interpolation techniques of subsample estimators.

1.3.2 Two Dimensional Motion Tracking Methods

One dimensional motion tracking imposes limitations for many applications. For example, in the blood flow or tissue motion estimation, motion tracking along beam direction, i.e., the axial direction, results in unknown motion in the lateral direction [50], which could be significant. In the elastography application, loss of strain estimation in the lateral direction comes from incapability of one dimensional displacement estimation to track motion in the lateral direction. Two-dimensional temperature estimation relies on performance of delay estimation in both the axial and lateral directions [51–53]. There is very limited research conducted in the lateral displacement estimation compared to the axial direction, though lateral performance of common estimators has been rigorously addressed in [54]. The effects of key parameters, i.e., lateral displacement, pitch, beamwidth, beam overlap, and interpolation, were studied on performance of lateral displacement estimators.

A 2D speckle tracking based on cross-correlation was first proposed by Trahey *et al.* [13] in 1987, which is calculated by:

$$R(m,n) = \frac{\sum_{i=1}^{I}\sum_{j=1}^{J}(X_{i,j}-\bar{X})(Y_{i+m,j+n}-\bar{Y})}{\sqrt{\sum_{i=1}^{I}\sum_{j=1}^{J}(X_{i,j}-\bar{X})^2(Y_{i+m,j+n}-\bar{Y})^2}}, \tag{1.3}$$

where $\bar{X}$ and $\bar{Y}$ are the average values of the corresponding image regions. As shown, this 2D speckle tracking method is essentially an extension of the 1D case. Therefore, applying the same idea in the axial direction to other dimensions could give rise to estimation in other directions [55]. Techniques based on pattern matching functions, for instance, parabolic fitting, cosine fitting or others, can be easily migrated into a multi-dimensional scenario [56, 57].

A different implementation of tracking the lateral motion is proposed by Ebbini [58]. A new algorithm called the phase-coupled method uses the phase of the 2D complex cross correlation for robust and efficient estimation of displacement from speckle data [58]. The key in this method is that it needs a significantly smaller interpolation factor in the lateral direction in order to achieve a reasonable subsample accuracy.

Since the lateral spectrum of ultrasound signals is centered around zero frequency

(DC) and no lateral phase is available in the original signals, synthetic lateral phase was generated by eliminating the positive or negative half of the lateral spectrum of the analytic signal in [59]. Based on complex signals from synthetic lateral phases, complex cross-correlation functions can be calculated. Applying a linear approximation in the vicinity of the correlation peak, the 2D displacement can be found by locating the intersection of two zero phase lines.

1.4 Contributions of this Thesis Research

The main contribution of this dissertation is extending the 1D speckle tracking method into a more general multi-dimensional method. Specifically, in the axial direction, the zero-crossing method takes advantage of the carrier frequency in this direction and uses the linearity of phase information of the complex normalized cross correlation function. A mathematical model is used to derive this method. A series of comparisons between this method and other methods are investigated since there has been no direct performance study in this area before. Model parameters, for instance, signal to noise ratio (SNR), computational cost are studied to show relative performance among subsample estimators. Deformation factor is also incorporated into simulation to mimic real signals. Bias and standard deviation, which are common criterion of measuring estimators' performance, are calculated under numerous simulations. It is shown that zero phase crossing method is more stable and requires less computation resources. Based on previous study, this idea is also successfully applied to the lateral direction, which lays the foundations of a new 2D speckle tracking method. Similar simulation as in the axial direction is also done in order to validate this idea. Besides, different scattering scenario simulated in FieldII [60] provides a tool to compare performance of various subsample estimators.

More importantly, combining the cases both in the axial and lateral directions gives rise to a new 2D speckle tracking method, called 2D zero phase crossing method. Not only does this method preserve the superior performance in the axial direction thanks to its carrier frequency, but it also provides a relative excellent estimation in the lateral direction. Linearity of zero phase lines around the true displacement can be made without additional computational overhead. Moreover, parallel computation of zero

phase lines in the axial and lateral directions can be decoupled which makes possible real-time implementation of this method. New technologies can be used to facilitate implementation of this method. For example, CUDA programming for GPU makes possible implementation of real-time zero-phase crossing. Phantom with a programmed motor to generate a known displacement is fabricated to experimentally investigate their performance. Finally, a flow phantom with synchronized sensor data severs as a good platform. Dynamic characterization of flow phantom was calculated along with other estimators.

1.5 Applications

Listed are several categorized applications of displacement estimation:

- Elastography has been developed into an effective imaging method of estimating the local elastic properties of biological tissues [61–65]. Cancer detection or classification, a current *in vivo* application, benefits a lot from elastography. For example, these applications include but are not limited to breast cancer detection using strain estimator [66], prostate cancer detection [67, 68], etc. Typically, the elastography image is generated by taking the spatial gradient of the estimated displacement [69, 70]. Therefore, the quality of strain imaging heavily relies on accuracy of the displacement estimation.

- Multi-dimensional velocity estimation [71–73] and tissue motion imaging depends on the displacement estimation [74–79]. Temperature estimation, typically an accumulation along time of spatial derivative of displacement fields, closely ties to the motion tracking algorithm.

- Radiation force imaging is another method of measuring mechanical properties of tissue. Displacement (typically a few micrometers) induced by radiation force has to be estimated for the purpose of depicting stiffness images [80–83].

- Shear wave imaging, a noninvasive and quantitative measurement of shear modulus of tissues, has to measure shear wave velocity, whose accuracy depends on performance of the displacement estimation [84–88].

- Pulse wave velocity provides a measurement of arterial stiffness. For example, the European Society of Hypertension and the European Society of Cardiology have recently recommended the use of the carotid-femoral pulse wave velocity as a favored measure of aortic stiffness for the management of arterial hypertension [89]. The accuracy of pulse wave velocity suffers from errors of distance measurements and time-delay measurements [90].

1.6 Organization of the Thesis

The dissertation is organized in six chapters. Each chapter is presented by an individual introduction, theory, methods and results, conclusions.

Chapter 2 derives the basic theory underlying in ultrasound speckle tracking area. Zero-phase crossing method is proposed with the aid of a simplified mathematical model. Simulation and experiment results validate its feasibility. Chapter 3 essentially applies the same idea from Chapter 2 to a different dimension, the lateral direction. A low-pass baseband signal without carrier is used to derive this method. Comparison of performance is also conducted to explain zero-crossing method's viability. Chapter 4 extends materials from Chapter 2 and Chapter 3 into a 2D problem. Since the simplified model is separable in the axial and lateral directions, estimation in both directions can be decoupled into each individual direction. Computationally speaking, the zero-crossing method consists of two tasks which can be simultaneously deployed to computation in parallel. Uniform phantom is fabricated to compare experimental performance of various subsample estimators with a pre-defined displacement by a programmed motor. Chapter 5 compares the new method with other common 2D subsample estimators and our previously proposed phase-couple method. In addition, the phase-coupled method uses a relatively small factor in the lateral direction. Finally, Chapter 6 summarizes the conclusion and future work related to the 2D zero-crossing algorithm.

Chapter 2

One Dimensional Speckle Tracking Methods in The Axial Direction

2.1 Introduction

Displacement estimation in ultrasound is the first step in several problems with significant practical applications, e.g., tissue elastography [91–94], noninvasive temperature estimation [51, 53], flow estimation [95–97], target tracking during image-guided procedures [98], wall motion [89,99], and many other applications [100–102]. The performance of these applications is in close conjunction with the performance of displacement estimation. For example, ultrasound strain imaging has become a powerful tool for a wide range of biomedical applications. Despite of a direct strain estimator based on spectral shift estimator proposed in [11], a high-quality strain image requires an accurate motion tracking method because strain maps (i.e., spatial derivatives of displacements) are greatly impacted by displacement estimates [103].

As a result of coherent scattering of incident waves by a multitude of point scatters within resolution cell of the imaging system, resemblance between sequential backscattered signals can be utilized to estimate the time-shift or phase-shift of RF echo signals [98]. In addition, with the advance of ultrasound scanner, higher and higher frame

rate has been achieved [104–108]. Thus a more accurate subsample estimator of frame-to-frame displacement is required. There are a number of techniques explored for the displacement estimation. The typical method is pattern matching [15], i.e., finding the subsample which maximizes the correlation function or minimizes sum absolute difference. There are many pattern matching techniques implemented, e.g., normalized and non-normalized cross correlation, autocorrelation [72,74], sum absolute difference (SAD) and sum squared difference (SSD), with different accuracy and complexity [21,37]. Due to the discrete feature of signals, large interpolation factor is generally required [61]. The common interpolation techniques [29, 109] include parabolic fitting, spline fitting, cosine fitting, grid slope [37] and many others [33]. The grid slope technique utilizes both cross correlation and autocorrelation, thus requiring more computational cost. Since the shape of cross correlation function is determined by the point spread function (PSF) of the imaging system and is not necessarily a parabolic, spline nor higher order polynomial function [49], error is introduced. Besides finding the maximum of correlation function, there exists other techniques proposed in [27, 28, 48]. These techniques are fitting the discrete signal by a spline function in the sacrifice of computational cost. An efficient way was shown in [110]. [27] gives details of common strategies of time-delay estimation, including curve fitting of RF echo and cross correlation function. One hybrid method using both autocorrelation and cross correlation was proposed in [49] in order to improve the subsample accuracy. Although there are many other methods in literature [24, 111], we only consider the commonly used pattern matching techniques and recently proposed method in [27]. Literature also gives a lot of comparison of different estimators [33, 42, 43], which are summarized in Figure 2.1. The subsample estimators can be categorized as two main approaches. The first approach is based on RF signals. Various interpolation techniques, or function matching using RF signals belongs to this category. Approaches based on FFT or Hilbert transformation are in the second category.

In this chapter, we introduce a method called the zero phase (ZP) crossing algorithm. In this method, instead of interpolating the magnitude of cross correlation, the subsample estimation is accomplished by finding the crossing of zero phase of complex cross correlation function. The zeros phase crossing can be easily found due to the fact that the phase of cross complex correlation function is linear. The mathematical derivation

of this method is described in Section 2.2. Since the zero phase crossing can be found analytically, this estimator is not subject to sampling quantization and therefore can be categorized as a continuous time-delay estimator. The detailed performance of this method compared with other estimators is presented in Section 2.4 and computational cost is also considered for real-time implementation.

Additional different deformation levels were introduced in order to test the performance of two particular continuous subsample estimators, one in time-domain and the other one in phase domain, called a spline-based algorithm and the algorithm proposed in this paper. The reason is that they have similar property, for instance, low bias and variance, continuous estimates, etc. Simulation in FieldII was also performed to generate more realistic backscattering frames which were then used to evaluate these two subsample estimators. In addition, RF frame of a carotid artery was collected from a commercial ultrasound linear array. Wall motion of the carotid artery is computed from the two subsample estimators.

This chapter is organized as follows: Section 2.2 presents theory of the zero phase crossing algorithm. Simulation and results & discussion are included in Section 2.3 and Section 2.4 respectively. Experimental results are shown in Section 2.5. Finally, conclusions are given in Section 2.6.

2.2 Theory

2.2.1 Zero Phase Crossing Algorithm

In this section, the zero phase crossing algorithm is developed using a one-dimensional (1-D) model. For simplicity, let $s(t)$ be the received signal and $r(t)$ be the displaced received signal which is the replicate of $s(t)$ after certain delay of t_0,

$$s(t) = u(t)\sin(\omega_0 t), \tag{2.1}$$

$$r(t) = u(t - t_0)\sin(\omega_0(t - t_0)), \tag{2.2}$$

where $u(t)$ is the pulse's envelop which is a bandlimited signal, ω_0 is the center frequency, and t_0 is the time delay which needs to be estimated [72, 74]. Figure 2.2 shows the

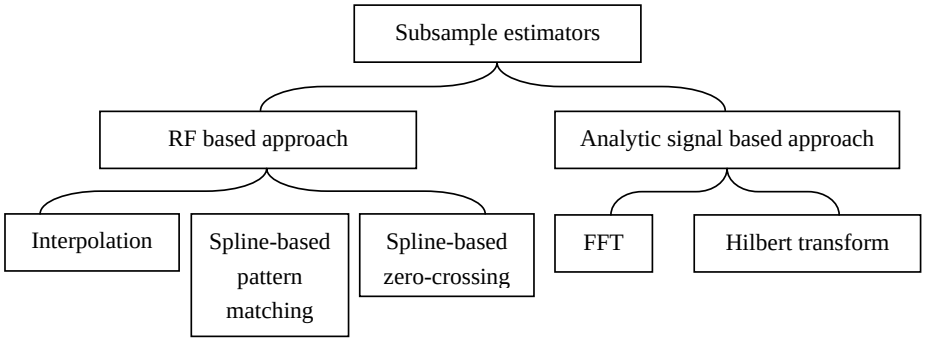

Figure 2.1: Various subsample estimators.

representative reference and delay RF signals (cropped) collected from a commercial ultrasound scanner. Note that due to increasing rate of frame acquisition, displacement of interest is usually less than one sampling resolution.

After taking Hilbert transform and with Bedrosian's theorem, we can have the analytic signals as:

$$s_a(t) = u(t)e^{j\omega_0 t}, \tag{2.3}$$

and,

$$r_a(t) = u(t - t_0)e^{j\omega_0(t-t_0)}. \tag{2.4}$$

The complex normalized cross correlation function (NCC) between $s_a(t)$ and $r_a(t)$ is:

$$R(\tau) = \frac{\int_{-\infty}^{\infty} s_a^*(t) r_a(t+\tau) dt}{\sqrt{\int_{-\infty}^{\infty} |s_a(t)|^2 \, dt \cdot \int_{-\infty}^{\infty} |r_a(t)|^2 \, dt}}. \tag{2.5}$$

By plugging (2.3) and (2.4) into (2.5), the complex normalized cross correlation function will be:

$$\begin{aligned} R(\tau) &= \frac{\int_{-\infty}^{\infty} u(t)e^{-j\omega_0 t} u(t+\tau-t_0)e^{j\omega_0(t+\tau-t_0)} dt}{\sqrt{\int_{-\infty}^{\infty} |u(t)|^2 \, dt \cdot \int_{-\infty}^{\infty} |u(t+\tau-t_0)|^2 \, dt}} \\ &= \frac{\int_{-\infty}^{\infty} u(t)u(t+\tau-t_0) dt}{\sqrt{\int_{-\infty}^{\infty} |u(t)|^2 \, dt \cdot \int_{-\infty}^{\infty} |u(t)|^2 \, dt}} \cdot e^{j\omega_0(\tau-t_0)} \\ &= \frac{\int_{-\infty}^{\infty} u(t)u(t+\tau-t_0) dt}{\int_{-\infty}^{\infty} |u(t)|^2 \, dt} \cdot e^{j\omega_0(\tau-t_0)}. \end{aligned} \tag{2.6}$$

The magnitude of complex normalized cross correlation function in (2.6) is:

$$M(\tau) = \frac{\int_{-\infty}^{\infty} u(t)u(t+\tau-t_0) dt}{\int_{-\infty}^{\infty} |u(t)|^2 \, dt}. \tag{2.7}$$

By Cauchy-Schwarz inequality,

$$\begin{aligned} M(\tau) &\leq \frac{\sqrt{\int_{-\infty}^{\infty} u^2(t) dt \cdot \int_{-\infty}^{\infty} u^2(t+\tau-t_0) dt}}{\int_{-\infty}^{\infty} u^2(t) dt} \\ &= \frac{\sqrt{\int_{-\infty}^{\infty} u^2(t) dt \cdot \int_{-\infty}^{\infty} u^2(t) dt}}{\int_{-\infty}^{\infty} u^2(t) dt} \\ &= 1, \end{aligned} \tag{2.8}$$

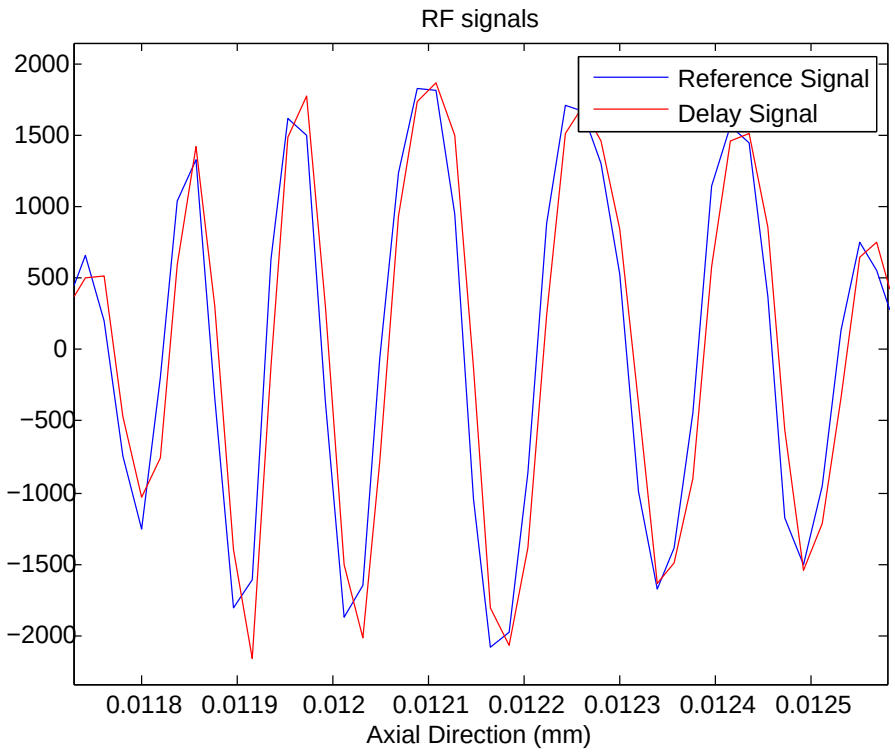

Figure 2.2: Representative reference and delay signals. The time delay between reference and delay signals is smaller than one sample

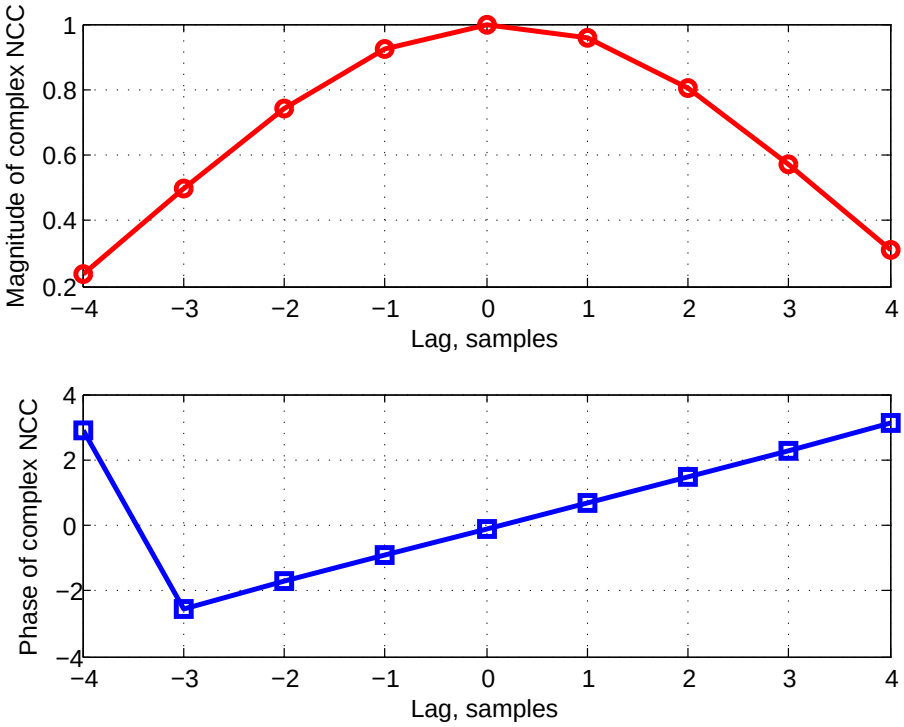

Figure 2.3: Magnitude (top) and phase (bottom) of a complex normalized cross correlation (NCC)

The "=" holds if and only if $u(t)$ is proportional to $u(t+\tau-t_0)$, i.e.,

$$u(t) = Au(t+\tau-t_0), \tag{2.9}$$

which means $A = 1$ and $\tau = t_0$. Therefore, the magnitude of complex normalized cross correlation function is maximized when $\tau = t_0$, i.e.,

$$\arg\max_{\tau} M(\tau) = t_0. \tag{2.10}$$

From (2.6), phase of complex normalized cross correlation function is:

$$P(\tau) = \omega_0(\tau - t_0). \tag{2.11}$$

As shown in (2.11), $P(\tau)$ is a linear function with the slope of ω_0 and

$$P(t_0) = 0. \tag{2.12}$$

Therefore, instead of estimating the subsample τ which maximizes $M(\tau)$, we can estimate the subsample τ by finding the zero phase crossing of $P(\tau)$.

For example, Figure 2.3 shows the magnitude and phase of a complex normalized cross correlation function. Note that the subsample which corresponding to the maximum magnitude (top) lies on the linear phase line (bottom) and the phase corresponding to this subsample is 0. We can tentatively estimate the maximum magnitude lies between 0 and 1 since the magnitude at 1 is slightly larger than that at -1. Interpolation techniques, for instance, parabolic fitting and cosine fitting methods, are trying to fit a specific function of the magnitude curve near the integer maximum magnitude and then analytically solve a optimization problem to find the subsample displacement.

In the noisy environment, the phase will not be a straight line, where a linear fitting technique can be utilized to get the analytic expression of zero phase crossing. Although we only consider the 1D case, extension of this method into the 2D problem has been addressed in [58]. In [58] interpolation factor in the lateral direction can be greatly decreased with the aid of zero phase line in the axial direction. Particularly, given the phase of discrete correlation function, $P(n)$, and n_0 corresponding to the discrete sample, of which the magnitude of complex correlation function is maximum, the zero phase crossing can be found using the following equation:

$$n_{zp} = \frac{-2P(n_0)}{P(n_0+1) - P(n_0-1)} + n_0, \tag{2.13}$$

which shows that only three phases ($P(n_0)$, $P(n_0-1)$, $P(n_0+1)$) are used for estimation of the zero phase crossing.

A general way is to use $N(\geq 3)$ points for linear fitting and find the zero phase crossing accordingly.

2.2.2 Spline-based continuous time-delay algorithm

In [27], given the discrete sent and received signal as $s[n]$ and $r[n]$, respectively, the subsample estimate can be solved analytically by minimizing the sum squared error

$$\varepsilon(t) = \sum_{i=1}^{M} (\hat{s}_i(t) - r(i))^2 = \sum_{i=1}^{M} (f_i(t) - r(i))^2 \tag{2.14}$$

where $\hat{s}_i(t)$ is the cubic spline representation of the discrete sent signal and $f_i(t) = a_i t^3 + b_i t^2 + c_i t + d_i$. Essentially, a_i, b_i, c_i, d_i are spline coefficients between $s[i]$ and $s[i+1]$ and they can be found through a variety of numerical methods, including matrix pseudo-inverses and infinite impulse response filters. Cubic splines are chosen in part because it is convenient and piecewise continuous.

Taking the derivative with respect to t,

$$\frac{d\varepsilon(t)}{dt} = \sum_{i=1}^{M} (2 f_i(t) \frac{df_i(t)}{dt} - 2 s_2[i] \frac{df_i(t)}{dt}) \tag{2.15}$$

After simplification and setting the result equal to zero,

$$\begin{aligned} \frac{d\varepsilon(t)}{dt} = {} & t^5 \sum_{i=1}^{M} 6a_i^2 + t^4 \sum_{i=1}^{M} 10 a_i b_i + t^3 \sum_{i=1}^{M} (8 a_i c_i + 4 b_i^2) \\ & + t^2 \sum_{i=1}^{M} (6 a_i d_i + 6 b_i c_i - 6 a_i s_2[i]) \\ & + t \sum_{i=1}^{M} (4 b_i d_i + 2 c_i^2 - 4 b_i s_2[i]) \\ & + \sum_{i=1}^{M} (2 c_i d_i - 2 c_i s_2[i]) \end{aligned} \tag{2.16}$$

a fifth order polynomial equation of t can be derived. Spline coefficients can be computed from $s[i]$. Among the five roots of this fifth order polynomial equation, the real one

which minimizes the error $\varepsilon(t)$ is chosen as the time delay estimate. The significant portion of computation lies in finding the cubic spline representation of $s[n]$ and solving the fifth-order polynomial. [27] showed a significant improve of performance over other curve fitting methods and also mentioned its heavy computation cost. Besides, [110] proposed some optimization in order to improve the computational speed of this method.

2.2.3 Other Common Algorithms

There are several block matching algorithms in the literature. Following are some common ones.

- Normalized cross correlation, which is similar to Equation 2.5 except that Equation 2.5 is calculated on analytic signals instead of RF signals, is:

$$R(\tau) = \frac{\int_{-\frac{T}{2}}^{\frac{T}{2}} s(t)r(t+\tau)dt}{\sqrt{\int_{-\frac{T}{2}}^{\frac{T}{2}} |s(t)|^2\, dt \cdot \int_{-\frac{T}{2}}^{\frac{T}{2}} |r(t)|^2\, dt}}. \tag{2.17}$$

- Sum absolute differences:

$$R(\tau) = \int_{-\frac{T}{2}}^{\frac{T}{2}} |s(t) - r(t+\tau)|\, dt. \tag{2.18}$$

- Normalized covariance:

$$R(\tau) = \frac{\int_{-\frac{T}{2}}^{\frac{T}{2}} (s(t) - \bar{s})(r(t+\tau) - \bar{r})dt}{\sqrt{\int_{-\frac{T}{2}}^{\frac{T}{2}} |s(t) - \bar{s}|^2\, dt \cdot \int_{-\frac{T}{2}}^{\frac{T}{2}} |r(t) - \bar{r}|^2\, dt}}, \tag{2.19}$$

  where,

$$\bar{s} = \frac{1}{T}\int_{-\frac{T}{2}}^{\frac{T}{2}} s(t)dt, \tag{2.20}$$

$$\bar{r} = \frac{1}{T}\int_{-\frac{T}{2}}^{\frac{T}{2}} r(t)dt. \tag{2.21}$$

- Sum square differences:

$$R(\tau) = \int_{-\frac{T}{2}}^{\frac{T}{2}} (s(t) - r(t+\tau))^2 dt \tag{2.22}$$

Suppose $M(n_0)$ is the maximum magnitude of the discretized cross correlation function with $M(n_0-1)$ and $M(n_0+1)$ being the neighbors. The estimated subsample displacement can be solved by following function fitting methods.

- Parabolic fitting to normalized cross correlation (PF):

$$\hat{\tau} = \frac{M(n_0-1) - M(n_0+1)}{2(M(n_0-1) - M(n_0) + M(n_0+1))} + n_0, \tag{2.23}$$

  which can be derived as follows.

  Let $y = ax^2+bx+c$ be the parabolic fitting function of three points $(-1, M(n_0-1))$, $(0, M(n_0))$, $(1, M(n_0+1))$ and x, y represent the lag and magnitude respectively. So we will have equations:

$$\begin{cases} M(n_0-1) = a - b + c \\ M(n_0) = c \\ M(n_0+1) = a + b + c \end{cases} . \tag{2.24}$$

  Solving a, b, c, the subsample corresponding to the maximum magnitude is $-\frac{b}{2a}$, shown in Equation 2.23, which also takes into account the integer shift.

- Cosine fitting to normalized cross correlation (CF)

$$\hat{\tau} = -\frac{\beta}{\alpha} + n_0, \tag{2.25}$$

  where α and β are coefficients determined by:

$$\begin{aligned} \alpha &= \arccos\left(\frac{M(n_0-1) + M(n_0+1)}{2M(n_0)}\right), \\ \beta &= \arccos\left(\frac{M(n_0-1) - M(n_0+1)}{2M(n_0)\sin\alpha}\right), \end{aligned} \tag{2.26}$$

  which can be derived in a similar manner.

  Let $y = \cos(\alpha x+\beta)$ be the cosine fitting function of three points $(-1, M(n_0-1))$, $(0, M(n_0))$, $(1, M(n_0+1))$ and x, y represent the lag and magnitude respectively.

So we will have equations:

$$\begin{cases} M(n_0-1) = \cos(-\alpha+\beta) \\ M(n_0) = \cos(\beta) \\ M(n_0+1) = \cos(\alpha+\beta) \end{cases} . \tag{2.27}$$

Combining the first and last terms,

$$\begin{aligned} \cos(\alpha)\cos(\beta) &= \frac{\cos(\alpha+\beta)+\cos(-\alpha+\beta)}{2} \\ &= \frac{M(n_0+1)+M(n_0-1)}{2}. \end{aligned} \tag{2.28}$$

Then,

$$\begin{cases} \cos(\beta) = M(n_0) \\ \cos(\alpha) = \dfrac{M(n_0+1)+M(n_0-1)}{2\cos(\beta)} \end{cases} . \tag{2.29}$$

The subsample corresponding to the maximum magnitude is $-\frac{\beta}{\alpha}$, shown in Equation 2.25, which also takes into account the integer shift.

2.3 Simulation

2.3.1 Subsample Estimators

In order to explore the performance of different estimators, a series of simulation was conducted to investigate estimator bias and standard deviation under various conditions. Although there are a lot of subsample estimators in literature discussed in Section 2.1, the zero phase (ZP) crossing algorithm derived in Section 2.2 was compared to the following subsample estimators:

- Viola's continuous time-delay estimator (CTE)
- Parabolic fitting to normalized cross correlation (PF)
- Cosine fitting to normalized cross correlation (CF)
- Spline fitting to normalized cross correlation (SF)

- Grid slope estimator (GS)
- 4th order polynomial interpolation to normalized cross correlation (4PF)

Detailed expressions of these estimators can be found in [27].

2.3.2 Simulation Method

MATLAB (MathWorks Inc., Natick, MA) was used for all the simulations in the paper. The bias and standard deviation which are the functions of center frequency, window length, bandwidth and SNR [2], are the most common merits of performance of the delay estimators and were calculated using Equation 2.31 and Equation 2.32. The default simulation parameters are listed as below.

- center frequency is 5 MHz
- fractional bandwidth is 50%
- sampling frequency is 40 MHz
- signal-to-noise-ratio (SNR) is 30 dB
- subsample displacement is 0.15 sample

Besides the settings above, subsample delays were varied from 0 to 0.95 samples in a step of 0.05 samples, so that a total of 20 different delays were evaluated for each subsample estimator. Essentially, a synthetic broadband ultrasound signal with a specific setting was generated. The reference and delays signals were sampled at the sampling rate with a known displacement between them. But the reference and delay signals were added at a certain SNR level. Then different subsample estimators were applied to calculate the displacement. Statistics was computed in Equation 2.31 and Equation 2.32.

A sinc-shaped rather than the Gaussian-enveloped sinusoid point spread function was chosen and given by [48]:

$$psf(t) = \frac{\sin(\pi B f_0 t)}{\pi B f_0 t} \sin(2\pi f_0 t), \tag{2.30}$$

where B is the fractional bandwidth, and f_0 is the center frequency.

The flow of simulation is listed below.

1. The point spread function $psf(t)$ in (2.30) was sampled from $-1.5/(Bf_0)$ to $1.5/(Bf_0)$ at a frequency of 4GHz, which is 100 times the sampling frequency. The reason of oversampling the $psf(t)$ is to obtain the known subsample displacement as discussed in the third step.

2. The sampled $psf(n)$ was convolved with a 100-point Gaussian random vector with mean of 0 and standard deviation of 1 to generate the base signal.

3. The base signal was down-sampled by a factor of 100. The reference and delayed signals were produced by starting with different samples to have a known subsample delay.

4. The reference and delayed signals were added with a Gaussian white noise to generate echo signals with different SNR.

5. 1000 realizations were run for each subsample displacement of every algorithm. Bias and standard deviation were computed by Equation 2.31 and Equation 2.32.

$$b(\hat{\Delta}) = \frac{1}{1000}\sum_{k=1}^{1000}(\hat{\Delta}[k] - \Delta[k]), \tag{2.31}$$

$$\sigma(\hat{\Delta}) = \sqrt{\frac{1}{1000}\sum_{k=1}^{1000}(\hat{\Delta}[k] - \frac{1}{1000}\sum_{k=1}^{1000}\hat{\Delta}[k])^2}, \tag{2.32}$$

where $\hat{\Delta}[k]$ is the estimated time delay and $\Delta[k]$ is the true time delay.

2.3.3 Deformed PSF

The delayed PSF was deformed at different levels to test the performance of subsample estimators under various situations. The deformed PSF is formulated by:

$$psf_{def}(t) = \frac{\sin(\pi B f_0(1-\alpha)t)}{\pi B f_0(1-\alpha)t}\sin(2\pi f_0(1-\alpha)t), \tag{2.33}$$

where α is the deformation factor. Simulation method is the same to the previous normal PSF except that the reference signal is generated by sampling the convolution of $psf(t)$ in Equation 2.30 with random scatters while the delayed signal was from the convolution of $psf_{def}(t)$ in Equation 2.33 with the same scatters.

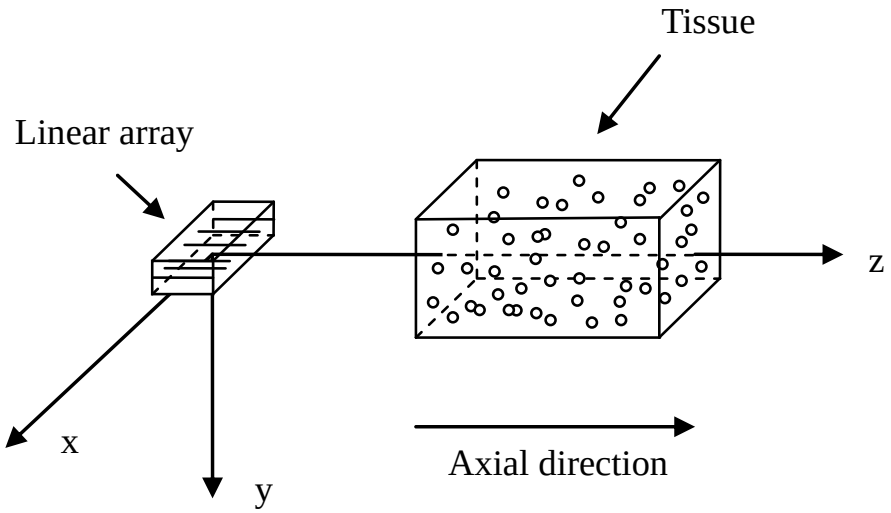

Figure 2.4: Simulation setup in FieldII. Scatters are uniformly distributed in a 80mm * 10mm * 80mm cuboid.

2.3.4 Simulation in FieldII

To simulate ultrasonic echo data, the FieldII [60] acoustical simulation program was used to generate a point spread function (PSF). Parameters of the simulation are as follows: a 196-element linear array transducer with 64 channels both in transmitter and receiver; the center frequency is 5 MHz and the sampling frequency is 100 MHz; the transmit pulse has a Gaussian envelop with a 60% bandwidth; The transmit beam was focused at a distance of 40 mm; and the speed of sound in tissue is assumed to be equal to 1540 m/s; height of element is 5 mm and width is λ (0.3mm).

To simulate ultrasonic scatters in tissue, 94626 scatters (approximately 10 scatters per resolution cell [112]) with amplitude of a Gaussian random variable were uniformly distributed in a cuboid with the dimension 80mm * 10mm * 80mm. In the uniform motion scenario, scatters were moving along the axial direction at the same speed. Nevertheless, scatters were moving at a linear increasing speed along the axial direction in the non-uniform scenario. Once we simulate the RF frame, Gaussian white noise can be added in order to create different SNR. Figure 2.4 shows the setup of simulation in FieldII.

Up to now, only subsample estimation, i.e., below one sample, was considered. In order to study the performance of subsample estimators in a more general way, multiple integer plus subsample displacement was also performed in MATLAB and FieldII. The setup of simulation was the same except that the displacement is above subsample.

2.4 Results and Discussion

Figure 2.5 shows the bias of the proposed algorithm and other subsample estimators as a function of the subsample displacement. The method of generating a known subsample displacement was presented in Section 2.3. The proposed algorithm outperforms other estimators across the entire range of subsample displacement, including the continuous time-delay estimator in [27]. 3-point spline curve interpolation provides a competitive estimation in certain range of subsample displacement, i.e., from 0-0.1 and from 0.65-0.8. Other curve fitting estimators, e.g., cosine fitting, parabolic fitting, exhibit comparable performance more or less. The competitive continuous time-delay estimator has a

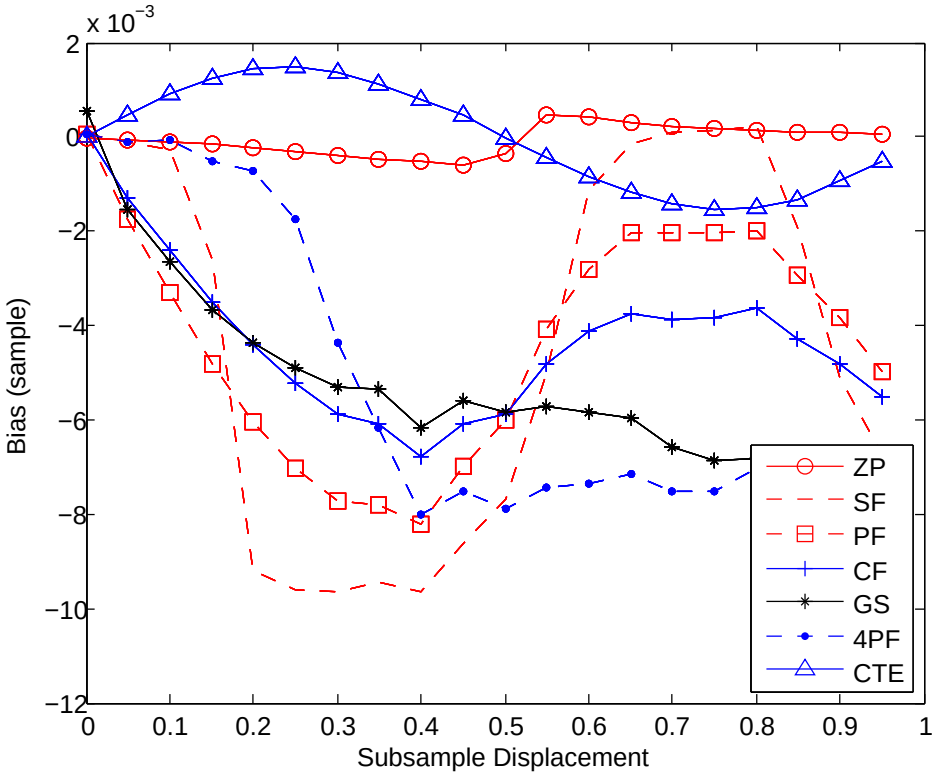

Figure 2.5: Bias of different delay estimators. The simulation setting is: $f_s = 40$MHz, $f_0 = 5$MHz, $B = 50\%$, $W = 49$ samples and SNR $= 30$ dB.

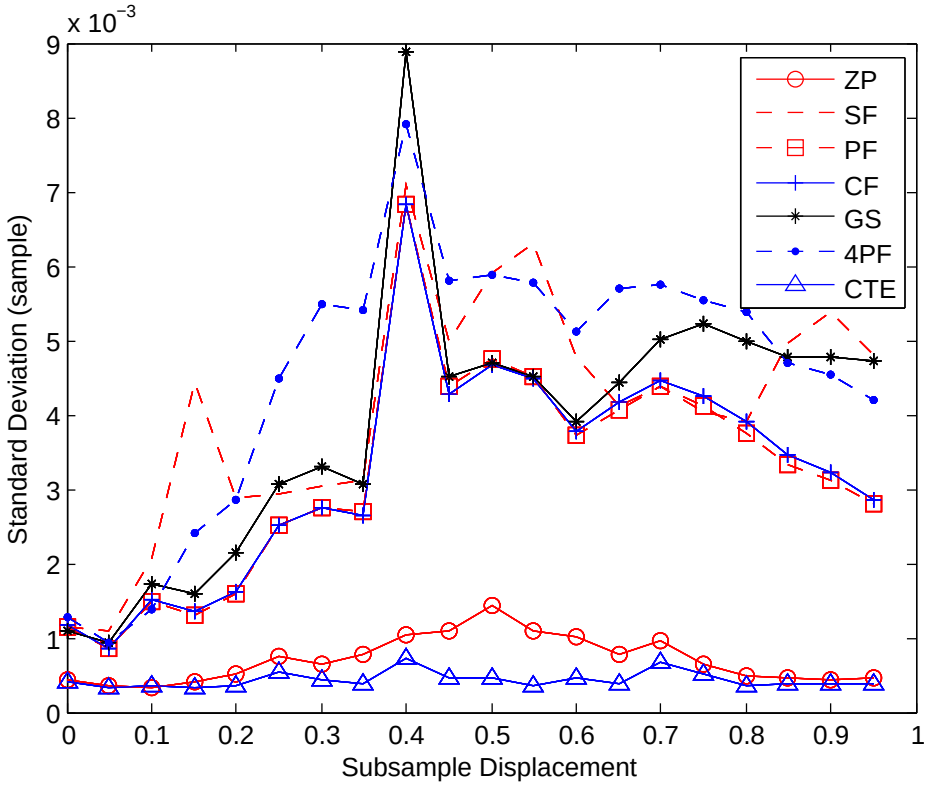

Figure 2.6: Standard deviation of different delay estimators. The simulation setting is: $f_s = 40$MHz, $f_0 = 5$MHz, $B = 50\%$, $W = 49$ samples and SNR $= 30$ dB.

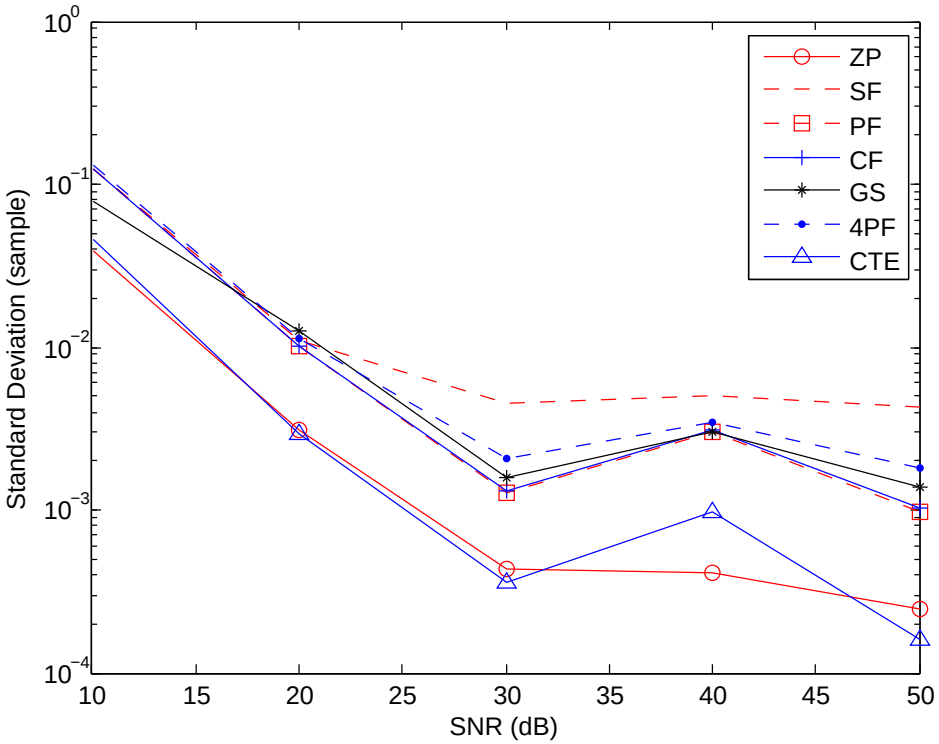

Figure 2.7: Standard deviation of different delay estimators as a function of SNR. The settings are: $f_s = 40$MHz, $f_0 = 5$MHz, $B = 50\%$, $W = 49$ samples and the default displacement is 0.15 sample.

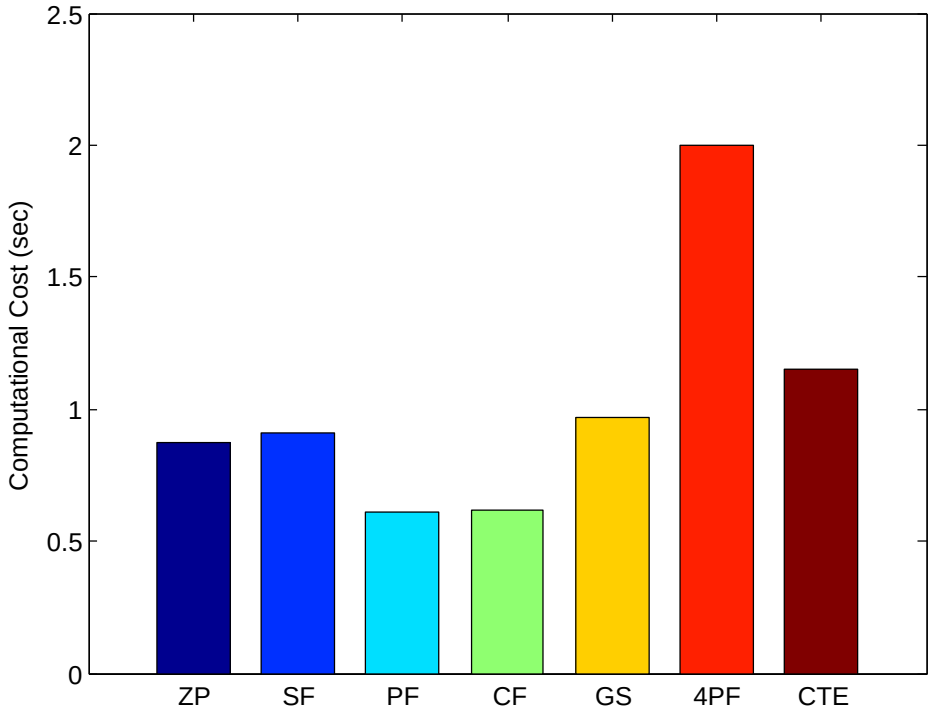

Figure 2.8: Computational cost of different delay estimators.

relatively large error around 0.25 and 0.75 subsample displacements. Another important observation is that interpolation of cross correlation function is prone to a worse estimation, since shape of cross correlation function depends on the specific band-pass RF signals and is not necessarily a perfect parabolic function nor cosine function. In a word, in term of bias, the zero phase crossing algorithm has the best performance.

Figure 2.6 presents the standard deviation of all subsample estimators as a function of the subsample displacement. Viola's continuous time-delay estimator performs superior to other estimators due to the fact that a piecewise cubic polynomial whose derivative and second order derivative are continuous at the interpolation nodes [48] can significantly remove the effect of noise. However, it is obtained at the expense of computation cost as discussed later. All 3-point curve fitting algorithms of magnitude of cross correlation perform similarly to each other. The zero phase crossing algorithm still preserves a relatively high performance. Phase unwrapping and minimum mean square error (MMSE) techniques can be utilized in order to incorporate multiple ($N \geq 3$) points. An interesting trend is that all estimators have a higher standard deviation around 0.5 sample displacement, which resembles previously published results. It could result from that cross correlation function is well-behaved with a smaller displacement.

Figure 2.7 shows the standard deviation of various subsample estimators as a function of SNR. In the range of low SNR (up to around 30 dB), the standard deviation decreases exponentially. As SNR goes to infinity, the standard deviation approximates an asymptotic line as predicted in Equation 1.2. Figure 2.7 also clearly shows that the zero phase crossing algorithm and the continuous time-delay estimator are the best choices among all subsample estimators across the whole range of SNR. This figure also validates the Figure 2.6 which shows the standard deviation with the default SNR of 30 dB. As mentioned before, the good performance of standard deviation of the continuous time-delay estimator (CTE) is achieved by more computational cost. These results are all consistent with previously reported results.

In order to compare the computational cost of each estimator, a common platform is used with a 2011a MATLAB for software simulator, Intel Core(TM) 2 Duo CPU @2.53 GHz and a 4 GB of RAM for hardware. The default settings mentioned in Section 2.3 are chosen for this simulation. Figure 2.8 depicts the total computation time of 1000 realizations of each algorithm. As shown in Figure 2.8, the computational cost of grid

slope is roughly twice that of window-based estimator, e.g., parabolic fitting and cosine fitting due to the fact that grid slope requires calculation of cross correlation and auto correlation function. The continuous time-delay estimator (CTE) consumes 35% more computation time than zero phase crossing algorithm.

In order to fully study performance of subsample estimators, the delay signal is deformed by a deformation factor, which is swept from -5% to 5% to generate different level deformed PSF. Figure 2.9 and Figure 2.10 show the bias and standard deviation of ZP and CTE subsample estimators with the default subsample equal to 0.5 sample. As seen from Figure 2.9, the ZP subsample estimator performs much better over the entire range of deformation factor in terms of bias. The bias of CTE subsample estimator is linear with the deformation factor while it is almost flat for zero phase crossing method. On the other hand, from the perspective of standard deviation, ZP and CTE subsample estimators behave almost the same except that ZP has a smaller standard deviation with a high deformation factor. As a matter of fact, since no prior information is known with respect of dynamics of the tissue, the ZP subsample estimator achieves notably superior performance to the CTE subsample estimator.

Figure 2.11 shows the displacement results in FieldII using the ZP and CTE subsample estimators. Figure 2.12 presents the actual motion of scatter and displacement results of ZP and CTE subsample estimators along the middle A-line. The performance of the two subsample estimators is fairly the same.

Figure 2.13 depicts the bias of ZP and CTE subsample estimators in MATLAB and FieldII. Above the subsample displacement, bias of CTE method increases dramatically while the ZP method still preserves its excellent property. It underlines the fact that CTE method is only estimating subsample displacement. Once the displacement is above one sample, either reference signal or delay signal has to be shifted by an integer shift to make sure that displacement between reference and delay signals is below one sample. The CTE method needs prior knowledge of integer shift, which have to be found using cross-correlation, sum square difference, etc. However, the magnitude of complex normalized cross correlation can be used to find the integer shift and the subsample shift can be found from the phase. Therefore, the ZP subsample estimator does not need any prior knowledge of displacement which means that it is a more robust method.

In a word, from simulation results and discussions in MATLAB and FieldII, the zero

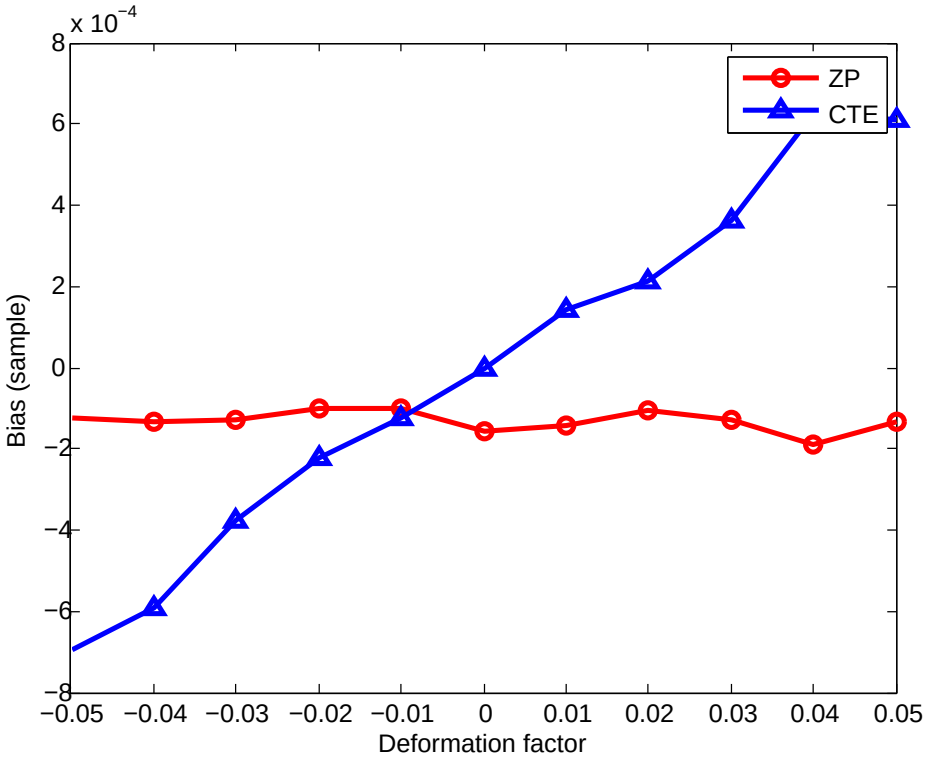

Figure 2.9: Bias of different delay estimators as a function of deformation factor. The simulation setting is: $f_s = 40$MHz, $f_0 = 5$MHz, $B = 50\%$, $W = 49$ samples and SNR $= 30$ dB and the known subsample displacement is 0.5.

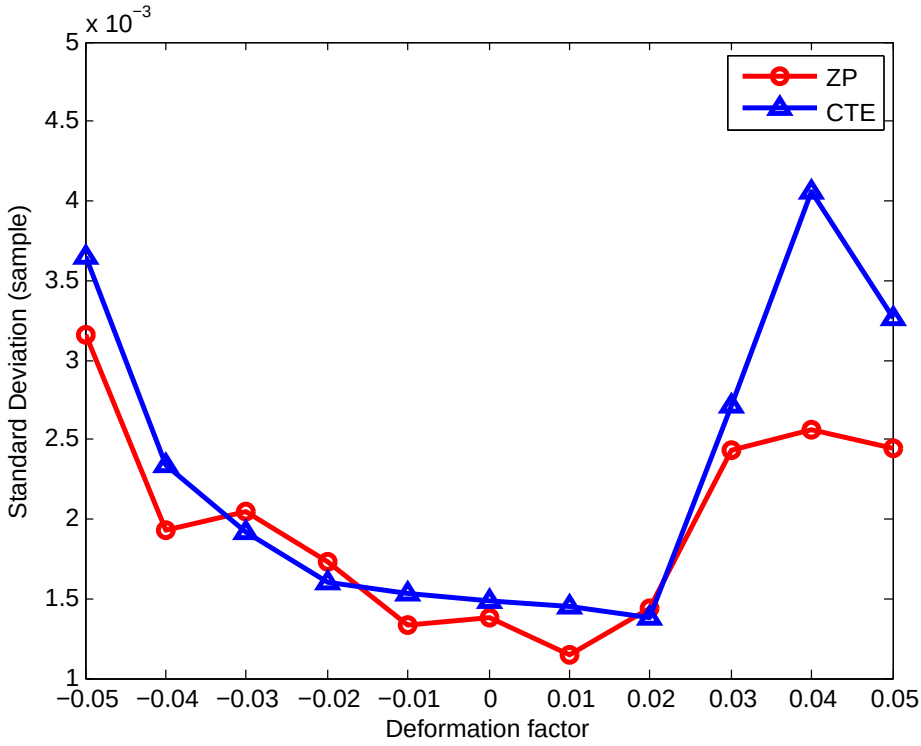

Figure 2.10: Standard deviation of different delay estimators as a function of deformation factor. The simulation setting is: $f_s = 40$MHz, $f_0 = 5$MHz, $B = 50\%$, $W = 49$ samples and SNR $= 30$ dB and the known subsample displacement is 0.5.

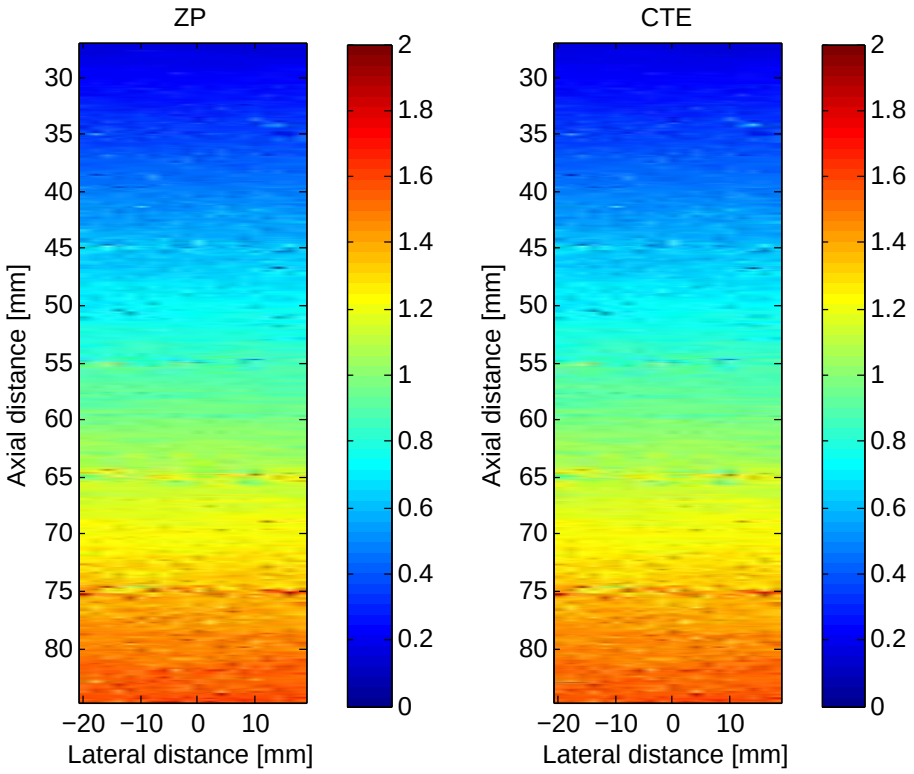

Figure 2.11: Axial displacement of ZP and CTE subsample estimators in FieldII. Scatters are moving at a linear increasing speed along the axial direction with 0 sample at $z = 20$ mm and 2 samples at $z = 100$ mm.

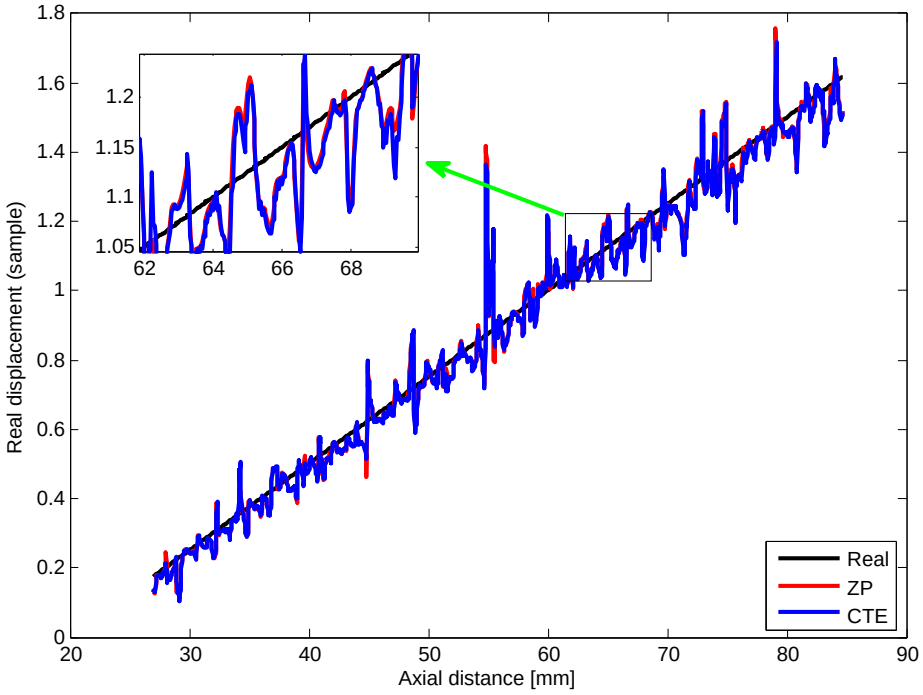

Figure 2.12: Displacement results of ZP and CTE subsample estimators along an A-line with actual motion of scatters.

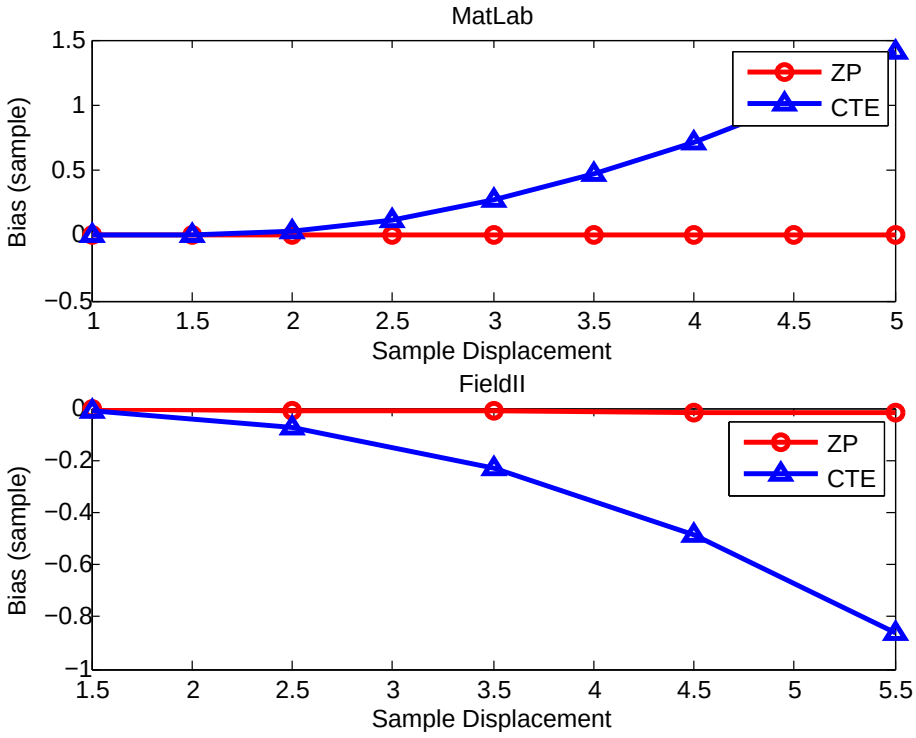

Figure 2.13: Bias of ZP and CTE subsample estimators. Note that the displacement is above subsample.

phase crossing algorithm is the best candidate for subsample estimator in terms of bias, standard deviation and computational cost.

2.5 Experimental Evaluation

To study the application of the subsample estimators with real data, a commercial ultrasound scanner (Sonix RP, Ultrasonix, BC, Canada) loaded with custom designed program and a linear array probe (LA14-5/38) was used to collect RF frames of the carotid artery in a healthy volunteer. The center frequency of the transmit pulse of the probe is 7.5 MHz. The RF frames (50 A-lines) were collected at 325 Hz (a total of 642 frames) and then streamlined to a controller PC through Gigabit Ethernet and wall motion was calculated offline in MATLAB using the ZP and CTE subsample estimators with a window size of 25 samples.

Figure 2.14 illustrates the B-mode image of the carotid artery. It clearly shows demarcation of the anterior and posterior walls. Figure 2.15 and Figure 2.16 depict the dynamic pulsation of anterior wall and posterior wall, respectively, at the middle A-line shown in Figure 2.14. Both the ZP and CTE subsample estimators capture the subsample motion of wall and results of the two methods match each other in a good manner. The fine resolution (sub-sample) of movement of wall results from the capability of the continuous estimators. Figure 2.15 and Figure 2.16 clearly show the periodic contracting and expanding of the carotid artery. Note in Figure 2.13, simulations in both Matlab and FieldII show that the CTE method tends to have a over-estimate with a large displacement. We can observe similar phenomena since as time goes ZP method is more stable with respect to a certain displacement level. Therefore, the ZP method is a more robust way of subsample estimation.

Figure 2.17 and Figure 2.18 shows the Bmode images overlayed by the estimated displacement fields at 0.15 sec and 0.6 sec respectively from CTE and ZP algorithms. Extreme similarity is shown in the two representative displacement fields. As we expect from Figure 2.15 and Figure 2.16, displacement at 0.15 sec is the opposite direction of displacement at 0.6 sec. We can also see the clear expanding or contracting of the vessel wall since the anterior wall and posterior wall are moving in the opposite direction.

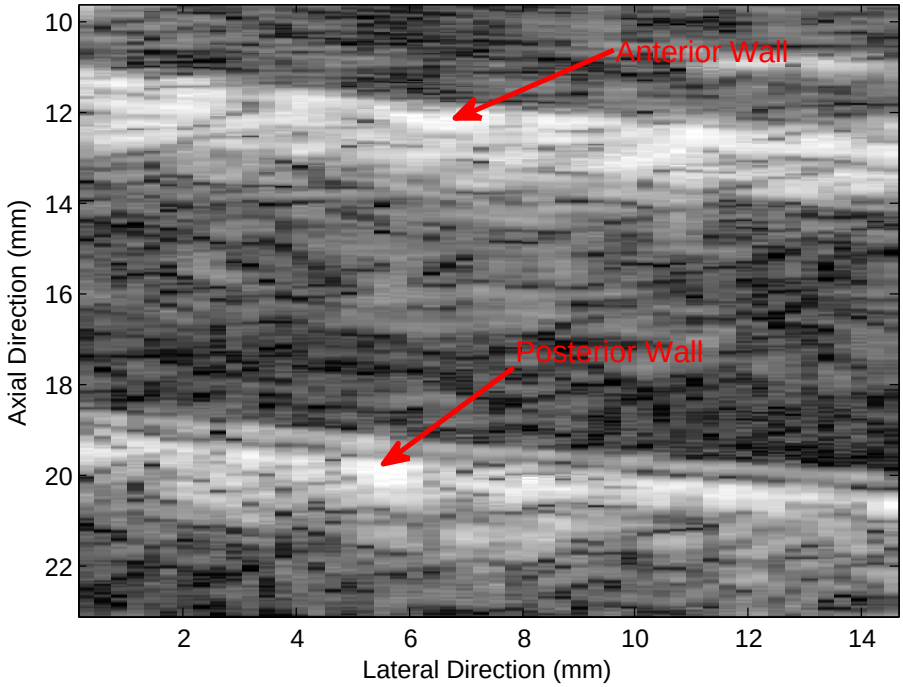

Figure 2.14: B-mode image of a carotid artery.

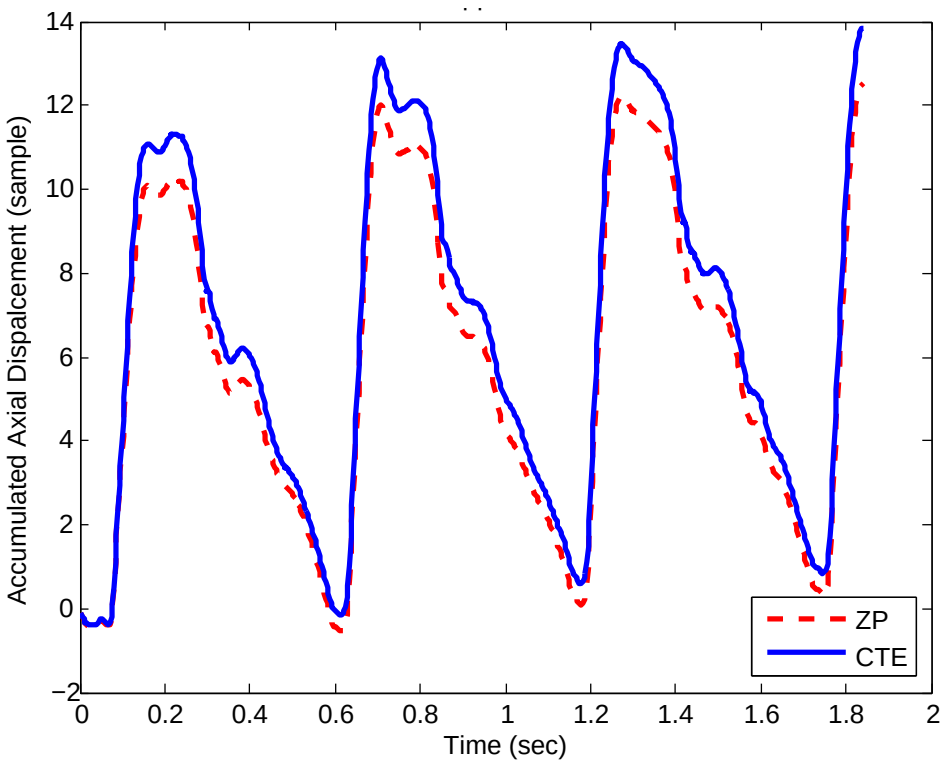

Figure 2.15: Accumulated anterior wall motion of the carotid artery by the ZP and CTE subsample estimators.

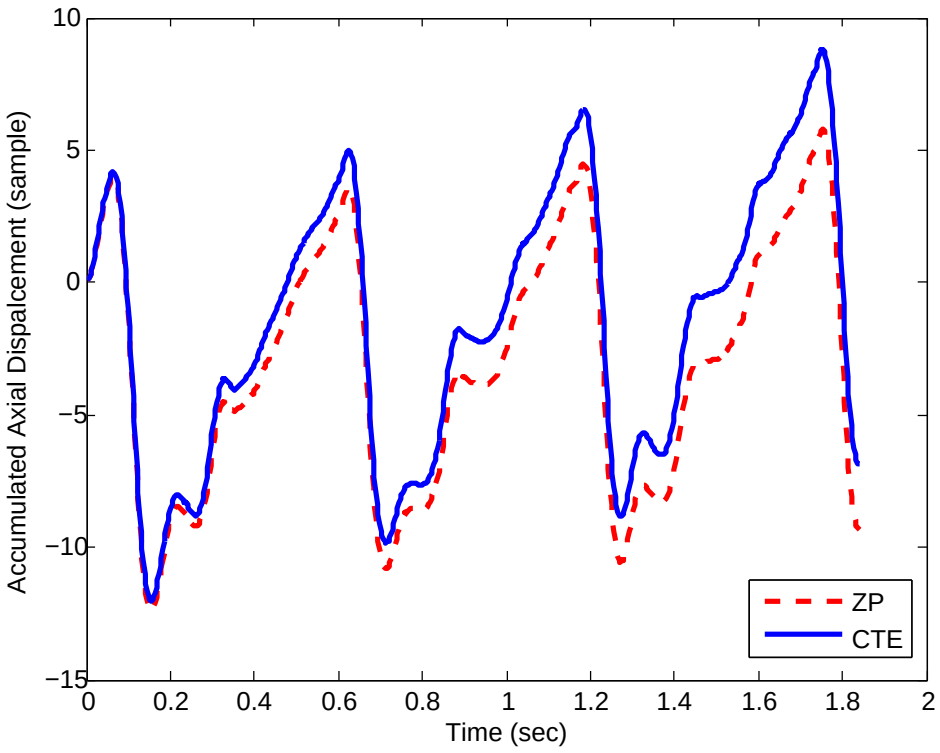

Figure 2.16: Accumulated posterior wall motion of the carotid artery by the ZP and CTE subsample estimators.

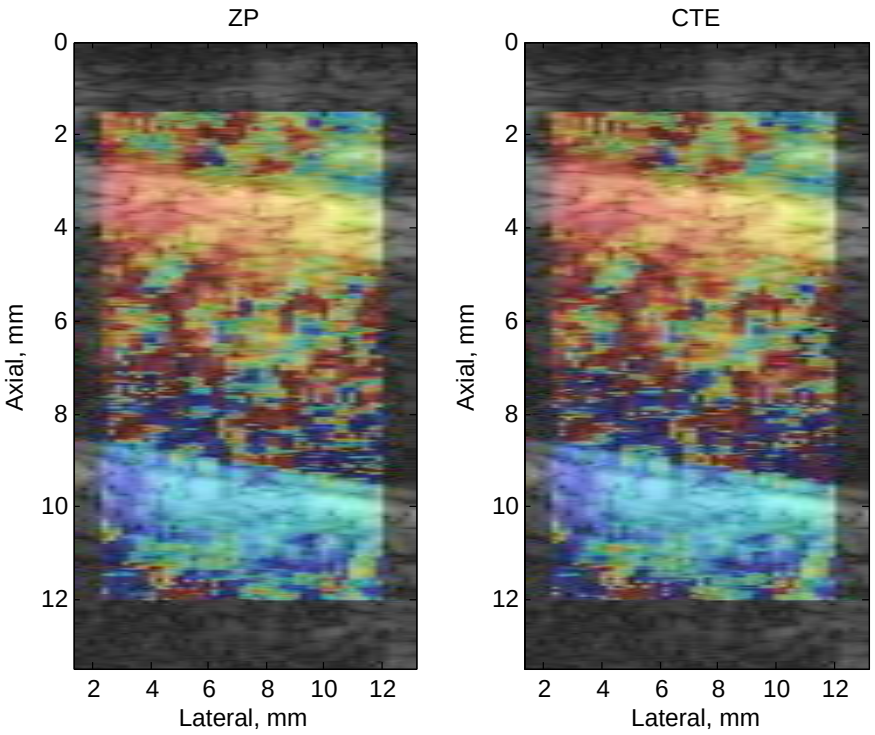

Figure 2.17: Axial displacement field of the carotid artery at 0.15 sec from ZP (left) and CTE (right)

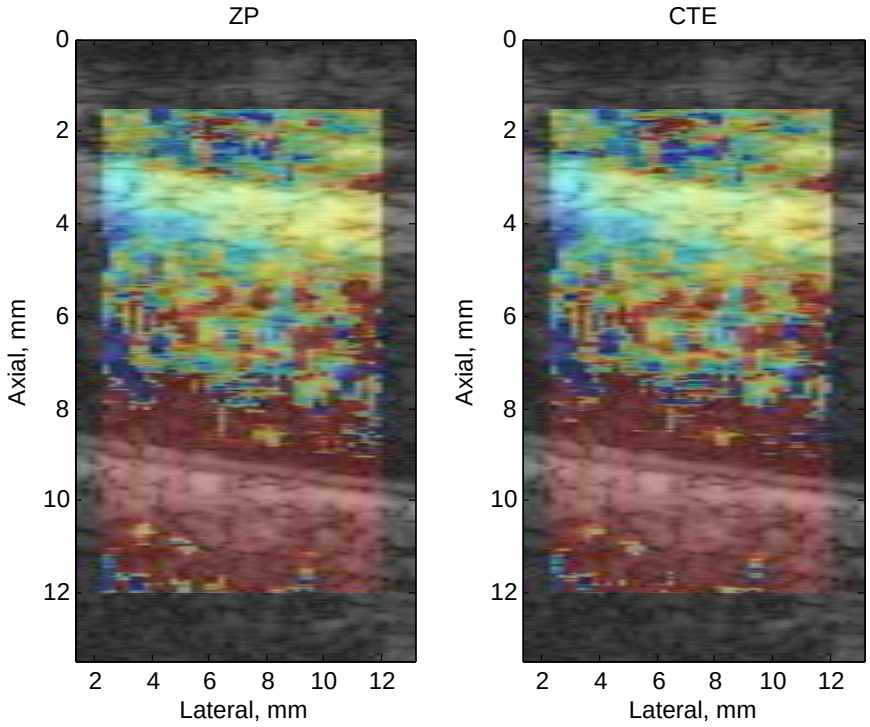

Figure 2.18: Axial displacement field of the carotid artery at 0.6 sec from ZP (left) and CTE (right)

2.6 Conclusions

A subsample estimator based on complex normalized cross correlation has been presented in this chapter. Mathematical proof of this method is shown and a series simulation is performed to compare the performance of this method with other common window-based techniques and recently proposed method in [27]. The simulation results show that under various settings, it is the most reliable algorithm in terms of bias, standard deviation and computational cost. If only the subsample shift is to be estimated, a substantial reduction of computation cost of window-based technique, including zero phase crossing algorithm, can be made. In addition to three points phase linearization, phase unwrapping will be a good choice to extend this proposed method. However, the CTE subsample estimator tends to introduce severe bias and standard deviation if the displacement is above subsample while the ZP subsample estimator maintains its excellent performance.

Further simulation in FieldII shows that the proposed method performs fairly the same to the CTE subsample estimator. This method is also successfully applied in estimating the subsample motion of a carotid artery. In addition, it has been successfully extended to the 2D speckle tracking scheme [58]. Using a moderate small interpolation factor, the phase-coupled 2D speckle tracking still generates a very smooth displacement field.

Chapter 3

One Dimensional Speckle Tracking Methods in The Lateral Direction

3.1 Introduction

Displacement estimation in ultrasound lies in heart of several problems with significant practical applications, e.g., blood flow estimation [73], tissue elastography, noninvasive temperature estimation, target tracking during image-guided procedures [98], and wall motion [89], radiation force imaging [82]. For instance, ultrasound strain imaging has become a powerful tool for a wide range of biomedical applications, which requires an accurate motion tracking method because strain maps (i.e., spatial derivatives of displacements) are greatly impacted by displacement estimates [49].

In addition, with advance of the ultrasound scanner, higher and higher frame rate has been achieved [89]. Thus a more accurate subsample estimator of frame-to-frame is required. The typical way is to find the subsample which maximizes the correlation function. Due to the discrete feature of signals, large interpolation factor is generally required [48]. The interpolation techniques include parabolic fitting, spline fitting, cosine fitting, grid slope [37] and many others [33]. The grid slope technique utilizes both cross

correlation and auto correlation. Since the shape of cross correlation function is determined by the point spread function (PSF) of the imaging system and is not necessarily a parabolic, spline nor higher order polynomial function [49], error is introduced. [44] gives a direct strain estimator based on spectral shift estimate. At the expense of higher computational cost, another algorithm with both continuous representation of reference and delay signals was used to calculate a continuous pattern matching function in [48]

Besides finding the maximum of correlation function, there exists other techniques proposed in [27] [48] [31]. These techniques are fitting the discrete signal by a spline function at the sacrifice of computational cost. An efficient way was shown in [110]. These methods were shown to exhibit better performance than window-based techniques in terms of bias and standard deviation. [27] gives details of common strategies of time-delay estimation, including curve fitting of RF echo and cross correlation function.

However, accuracy of displacement estimation in the lateral direction is primarily limited by the sparse pitch in ultrasound. As shown in Figure 3.1, the lateral resolution is close to the physical length of all elements divided by number of elements. Even though advanced beamforming may improve the lateral resolution in a small region of interest, limited improvement can be observed due to the fact that there is no carrier frequency in lateral direction. In order to achieve a subsample estimation, interpolation in the lateral direction is highly necessary. For instance, tissue/blood motion estimation requires an accurate subsample estimator especially with higher and higher frame rate.

A zero phase crossing method in the lateral direction is presented based on complex normalized cross correlation (NCC). Due to the fact that there is no analytic signal in the lateral direction, the phase of complex cross correlation is not necessarily linear. However, the subsample of maximum magnitude of complex correlation still lies on the zero phase line instead of interpolating the magnitude. Therefore, subsample displacement can be estimated by finding the zero phase crossing, though the phase of cross correlation function is dependent of scattering distribution and therefore not necessarily linear, which consequently could result in inaccurate estimation.

This chapter is organized as follows: Section 3.2 presents theory of zero phase crossing algorithm. Simulation and results & discussion are included in Section 3.3 and Section 3.4 respectively. Finally, conclusions are given in Section 3.5.

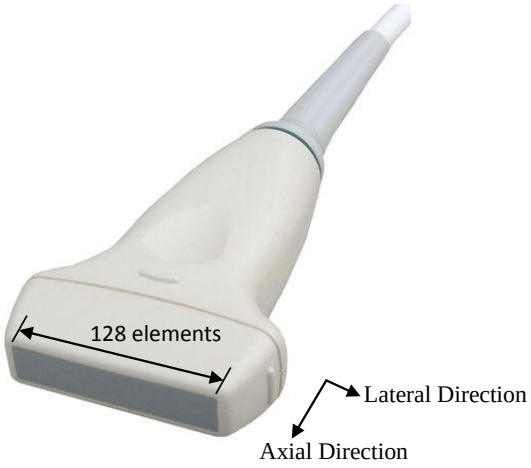

Figure 3.1: A typical linear array transducer. Note that the resolution in the lateral direction is defined by the physical length of the transducer divided by the number of elements and the resolution in the lateral direction is much coarser than that in the axial direction.

3.2 Theory

Similar to what is presented in the axial direction, we start with a simplified mathematical model. Let $s_r(t)$ be the received signal in the lateral direction [111]. The Hilbert transformation of $b_r(t)$ is $s_i(t)$,

$$H(s_r(t)) = s_i(t). \tag{3.1}$$

So the analytic expression of $s_r(t)$ is:

$$s_a(t) = s_r(t) + j \cdot s_i(t) = e(t) \cdot e^{j\phi(t)}, \tag{3.2}$$

where $e(t)$ is the envelop and $\phi(t)$ is the phase. After delay of t_d, the analytic displaced received signal, is $r_a(t) = s_a(t - t_d)$, i.e.,

$$r_a(t) = e(t - t_d) \cdot e^{j\phi(t-t_d)}. \tag{3.3}$$

Our objective is to estimate t_d based on the complex NCC function. The complex NCC between $s_a(t)$ and $r_a(t)$ is:

$$R(\tau) = \frac{\int_{-\infty}^{\infty} s_a^*(t) \cdot r_a(t+\tau)dt}{\sqrt{\int_{-\infty}^{\infty} |s_a(t)|^2 \, dt \cdot \int_{-\infty}^{\infty} |r_a(t)|^2 \, dt}}. \tag{3.4}$$

By plugging Equation 3.2 and Equation 3.3 into Equation 3.4, the complex NCC will be:

$$\begin{aligned} R(\tau) &= \frac{\int_{-\infty}^{\infty} e(t)e^{-j\phi(t)}e(t+\tau-t_0)e^{j\phi(t+\tau-t_0)}dt}{\sqrt{\int_{-\infty}^{\infty} |e(t)|^2 \, dt \cdot \int_{-\infty}^{\infty} |e(t+\tau-t_0)|^2 \, dt}} \\ &= \frac{\int_{-\infty}^{\infty} e(t)e(t+\tau-t_0)e^{j(\phi(t+\tau-t_0)-\phi(t))}dt}{\sqrt{\int_{-\infty}^{\infty} |e(t)|^2 \, dt \cdot \int_{-\infty}^{\infty} |e(t)|^2 \, dt}} \\ &= \frac{\int_{-\infty}^{\infty} e(t)e(t+\tau-t_0)e^{j(\phi(t+\tau-t_0)-\phi(t))}dt}{\int_{-\infty}^{\infty} |e(t)|^2 \, dt}. \end{aligned} \tag{3.5}$$

The magnitude of complex NCC function in Equation 3.5 is:

$$\begin{aligned} M(\tau) &= \frac{\left|\int_{-\infty}^{\infty} e(t)e(t+\tau-t_0)e^{j(\phi(t+\tau-t_0)-\phi(t))}dt\right|}{\int_{-\infty}^{\infty}|e(t)|^2\,dt} \\ &\leq \frac{\int_{-\infty}^{\infty}\left|e(t)e(t+\tau-t_0)e^{j(\phi(t+\tau-t_0)-\phi(t))}\right|dt}{\int_{-\infty}^{\infty}|e(t)|^2\,dt} \\ &= \frac{\int_{-\infty}^{\infty}|e(t)e(t+\tau-t_0)|\,dt}{\int_{-\infty}^{\infty}|e(t)|^2\,dt} \\ &\leq 1. \end{aligned} \tag{3.6}$$

The "=" holds if and only if $\tau = t_0$. Therefore, the magnitude of complex normalized cross-correlation is maximized when $\tau = t_0$, i.e.,

$$\arg\max_{\tau} M(\tau) = t_0. \tag{3.7}$$

Normally, interpolation scheme and curve fitting method are based on Equation 3.7, which shows that the displacement estimation can be found by means of locating the subsample which corresponds to the maximum magnitude. In addition, by plugging $\tau = t_0$ back into Equation 3.5, $R(t_0) = 1$ and therefore

$$\angle R(t_0) = 0. \tag{3.8}$$

The phase of $R(\tau)$ is not necessarily linear as shown in Equation 3.5 since there is no analytic signal in the lateral direction. Therefore, linearity of the phase line characterizes performance of the zero phase crossing method which uses the linear curve fitting technique.

For example, Figure 3.2 shows the magnitude and phase of a complex NCC. Note that the subsample which corresponds to the maximum magnitude (top) lies in the linear phase line (bottom) and the phase corresponding to this subsample is 0. In this specific case, phase has a good linearity.

Given the phase of discrete correlation function, $P(n)$, and n_0 corresponds to the discrete sample, of which the magnitude of complex correlation function is maximum, the zero phase crossing can be found using the following equation:

$$n_{zp} = \frac{-2P(n_0)}{P(n_0+1) - P(n_0-1)} + n_0, \tag{3.9}$$

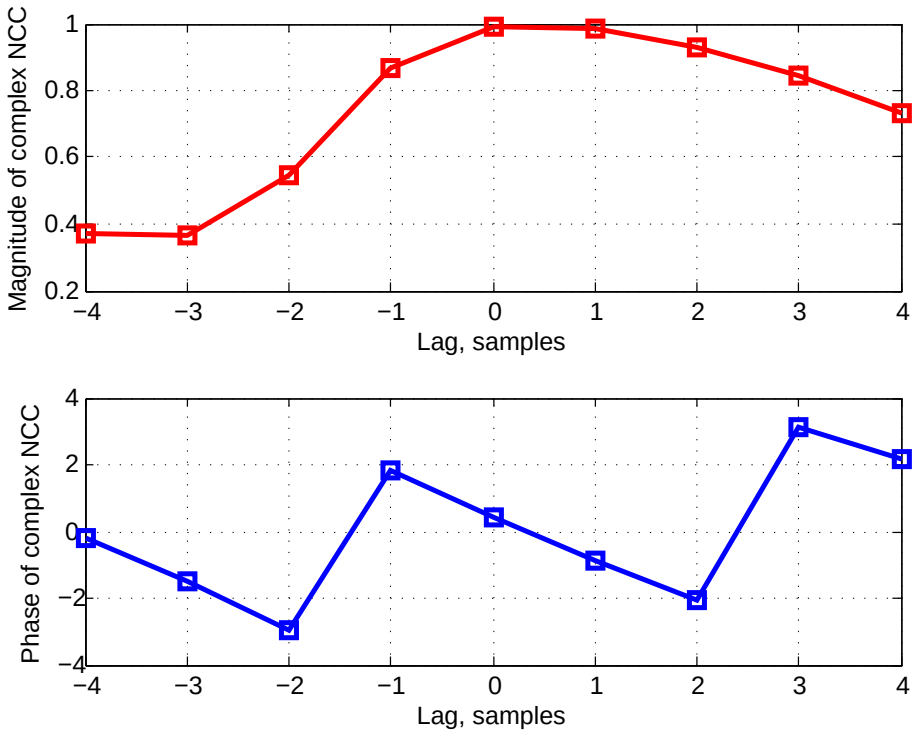

Figure 3.2: Magnitude and phase of a complex normalized cross correlation (NCC).

which shows that three phases ($P(N_0)$, $P(N_0 - 1)$, $P(n_0 + 1)$) are used for the estimation of zero phase crossing. In addition, before implementing Equation 3.9, phase unwrapping should be done.

3.3 Simulation

3.3.1 Subsample Estimators

In order to simplify the comparison of performance and similarity to the previous chapter, the zero phase (ZP) crossing algorithm mentioned in Section 3.2 was only compared to the two commonly used subsample estimators:

- Parabolic fitting (PF) to NCC
- Cosine fitting (CF) to NCC

Detailed expressions of these estimators can be found in [27].

3.3.2 Simulation Method

MATLAB (MathWorks Inc., Natick, MA) was used for all the simulations. The bias and standard deviation of the delay estimators are the most common merits of performance and were calculated using Equation 3.11 and Equation 3.12. The default simulation parameter settings were listed in Table 3.1. Besides the settings above, subsample delays were varied from -0.5 to 0.5 samples in a step of 0.05 samples, so that a total of 21 different delays were evaluated for each subsample estimator.

Table 3.1: Default values used to generate $psf(x)$

Parameter	Value
Azimuthal aperture width (D)	20 mm
Depth in tissue (x_r)	50 mm
Scaling factor (A)	1
Wavelength at the system center frequency (λ)	0.308 mm
System center frequency (f_0)	5.0 MHz

A sinc-squared point spread function was chosen and given by [1]:

$$psf(x) = A(\frac{\sin\left(\frac{\pi Dx}{\lambda x_r}\right)}{\left(\frac{\pi Dx}{\lambda x_r}\right)})^2 \tag{3.10}$$

The flow of simulation was listed below.

1. The point spread function $psf(x)$ in Equation 3.10 was sampled by a spatial grid x_G ranging from -2mm to 2mm at a step of $\frac{\lambda x_r}{lD}$, where the resolution length is $\frac{\lambda x_r}{D}$ and l is the number of samples per resolution length and l is set 4 by default. The sampled $psf(x)$ is $psf_{pre}(n)$.

2. $psf_{pre}(n)$ was convolved with a 1000-point Gaussian random vector with mean of 0 and standard deviation of 1 to generate the pre-compressed signal.

3. The point spread function $psf(x)$ in Equation 3.10 was sampled by a shifted spatial grid $x_G + x_d$, where x_d is the known subsample displacement. The newly sampled $psf(x)$ is $psf_{post}(n)$.

4. $psf_{post}(n)$ was convolved with the same 1000-point Gaussian random vector as $psf_{pre}(n)$ was to generate the post-compressed signal.

5. The pre- and post-compressed signals were added with a Gaussian white noise to generate echo signals with different signal-to-noise-ratios. Then various subsample estimators were implemented to calculate the displacement between pre- and post-compressed signals.

6. 1000 realizations were run for each algorithm. Bias and standard deviation were computed by Equation 3.11 and Equation 3.12.

$$b(\hat{\Delta}) = \frac{1}{1000}\sum_{k=1}^{1000}(\hat{\Delta}[k] - \Delta[k]), \tag{3.11}$$

$$\sigma(\hat{\Delta}) = \sqrt{\frac{1}{1000}\sum_{k=1}^{1000}(\hat{\Delta}[k] - \frac{1}{1000}\sum_{k=1}^{1000}\hat{\Delta}[k])^2} \tag{3.12}$$

where $\hat{\Delta}[k]$ is the estimated time delays, and $\Delta[k]$ is the true time delays.

3.3.3 Simulation in FieldII

To simulate ultrasonic echo data, the FieldII acoustical simulation program was used to generate a point spread function (PSF). Parameters of the simulation are as follows: a 196-element linear array transducer with 64 channels both in transmitter and receiver; the center frequency is 5 MHz and the sampling frequency is 40 MHz; the transmit pulse has a Gaussian envelop with a 60% bandwidth; The transmit beam was focused at a distance of 40 mm; and the speed of sound in tissue is assumed to be equal to 1540 m/s; height of element is 5 mm and width is λ (0.3mm).

To simulate ultrasonic scatterers in tissue, 94626 scatterers (approximately 10 scatterers per resolution cell) with amplitude of a Gaussian random variable were uniformly distributed in a cuboid with the dimension of 80mm $\times$ 10mm $\times$ 40 mm. Scatterers were moving at a linearly increasing speed from -0.5 sample/fr at the lateral location of -2mm to 0.5 sample/fr at the lateral location of 2mm along the lateral direction. Once we simulate the RF frame, Gaussian white noise can be added in order to create different SNRs. Figure 3.3 shows the simulated point spread function in FieldII. Once frames of RF images are collected, different subsample estimators are applied to calculate the lateral displacement. Figure 3.4 depicts a representative Bmode image simulated in FieldII with 50 dB dynamic range.

3.4 Results and Discussion

Figure 3.5 shows the bias of the proposed algorithm and other subsample estimators as a function of the subsample displacement. The method of generating a known subsample displacement was presented in Section 3.3. The proposed algorithm outperforms other estimators across the entire range of subsample displacement. Cosine fitting and parabolic fitting methods exhibit comparable performance more or less. Interestingly, the bias of the curve fitting methods still preserves the sine-shaped property, as is seen in the axial case [27]. However, the proposed method tends to generate a linear bias with a small magnitude.

Figure 3.6 presents the standard deviation of all subsample estimators as a function of the subsample displacement. Similarly, parabolic fitting and cosine fitting methods perform relatively the same. Nevertheless, the proposed method exhibits superior

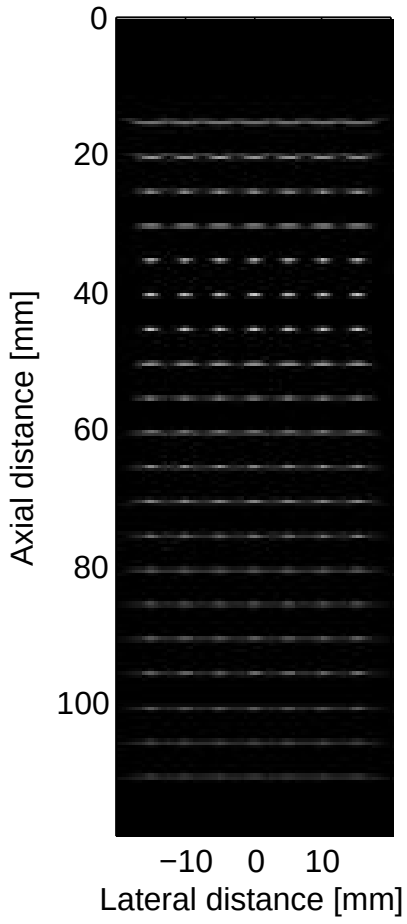

Figure 3.3: Point spread function used for simulation in FieldII. The focus is set at the depth of 40 mm.

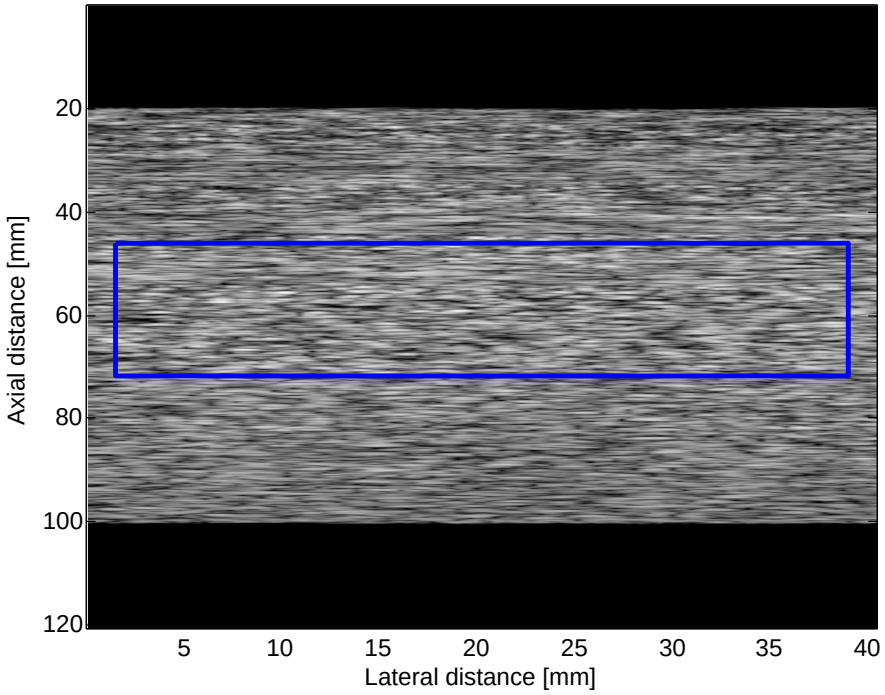

Figure 3.4: Bmode image of a uniform phantom simulated in FieldII with dynamic range of 50 dB. The blue rectangle is the region of interest for displacement estimation.

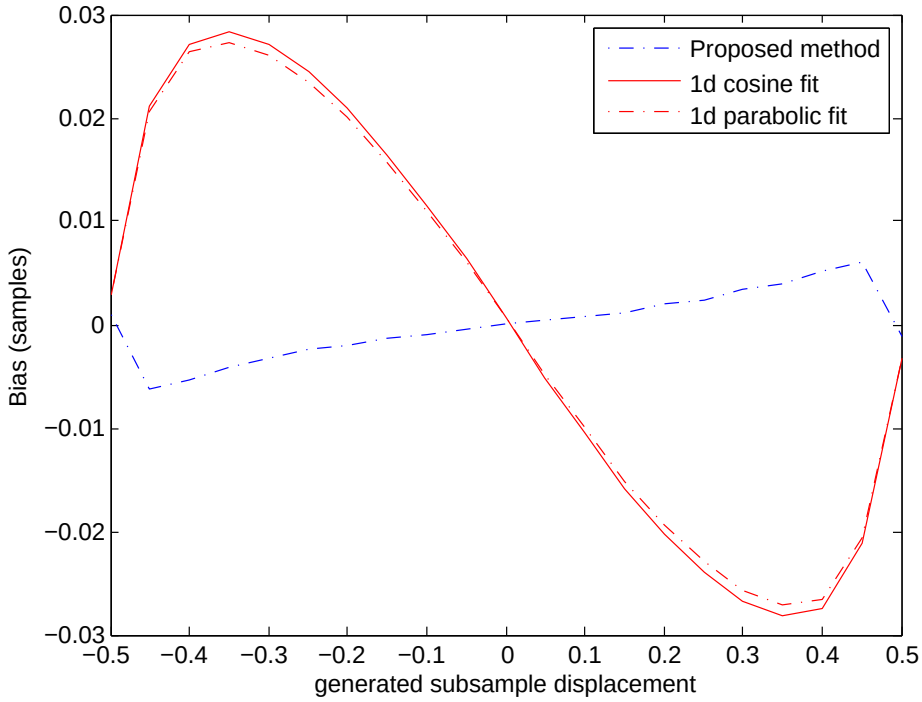

Figure 3.5: Bias of different delay estimators. The simulation setting is listed in Table 3.1.

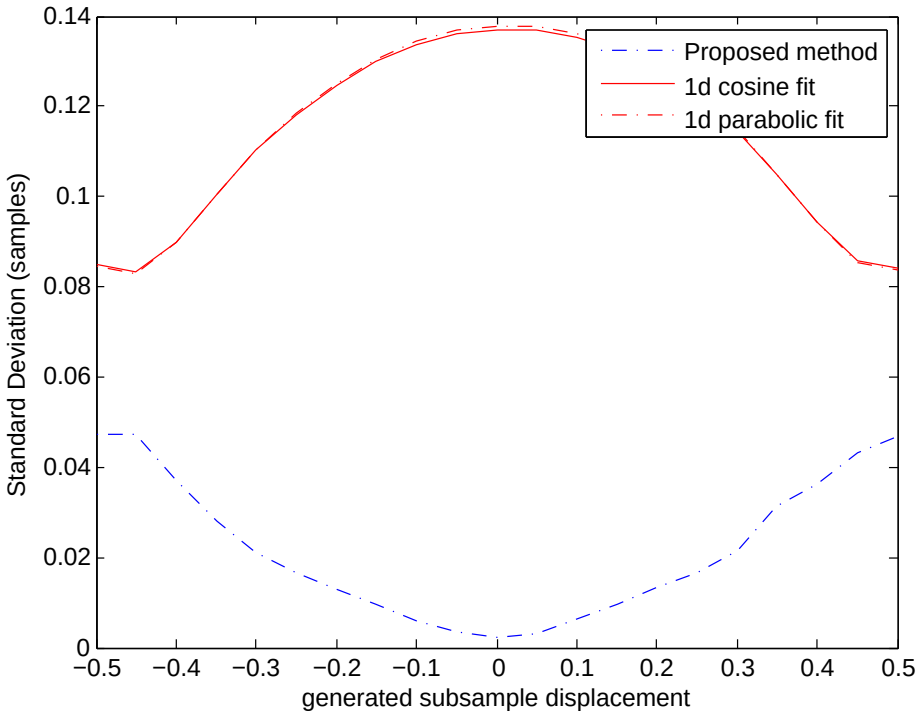

Figure 3.6: Standard deviation of different delay estimators. The simulation setting is listed in Table 3.1.

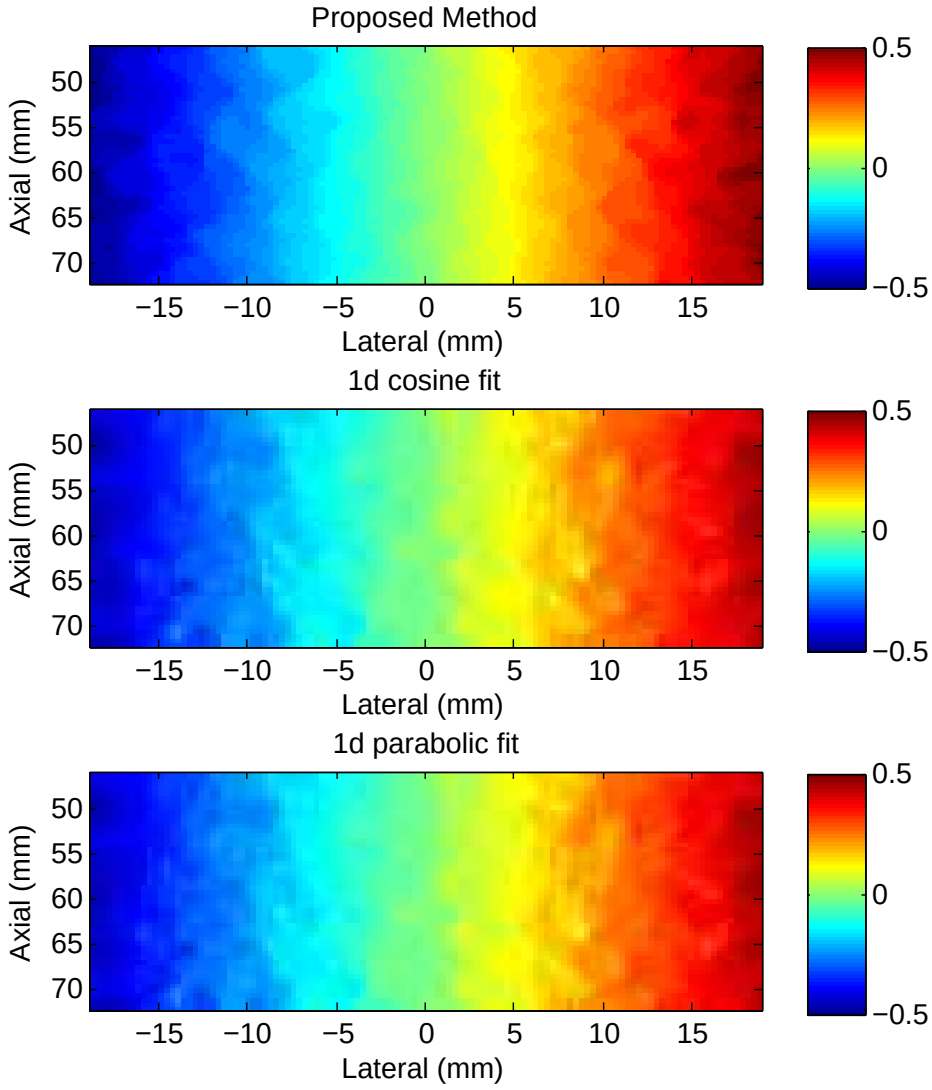

Figure 3.7: Lateral displacement estimation in FieldII. The true displacement field has a linearly increasing displacement from -0.5 sample at -20 mm to 0.5 sample at 20 mm.

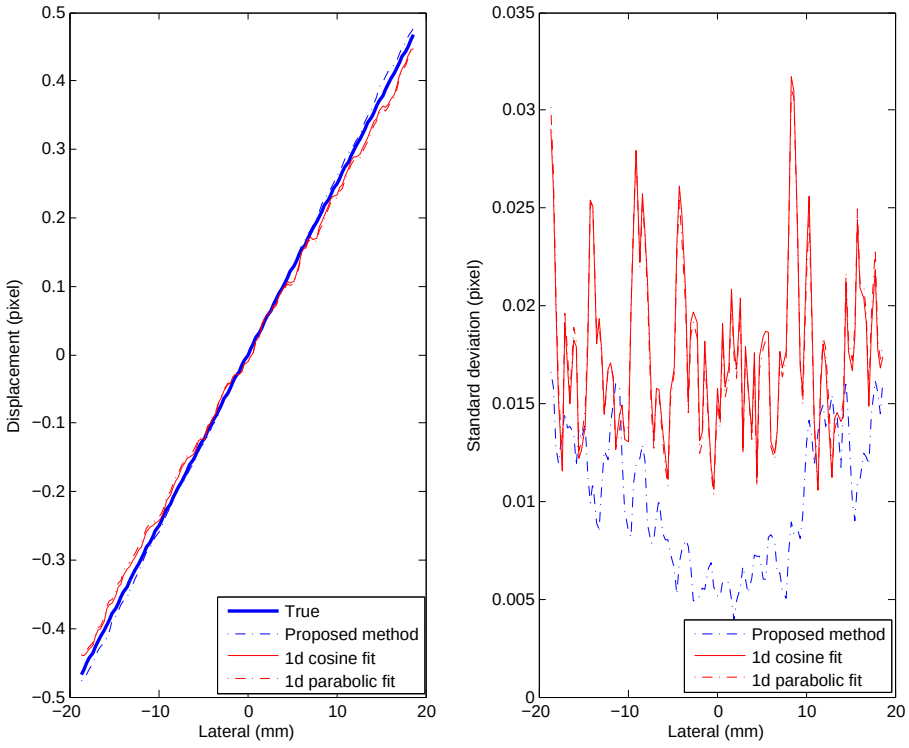

Figure 3.8: Average lateral estimation versus true displacement in FieldII (left) and standard deviation of three subsample estimators (right).

performance over the entire range, especially in smaller displacements. In addition, the standard deviation is monotonically decreasing of curve fitting methods but monotonically increasing of the proposed method as a function of absolute true subsample displacement. It might be due to facts that the proposed method is more dependent of similarity of the pre- and post-compression signals and that smaller displacement results in less distortion. Therefore, the zero phase crossing method is a much more promising method of detecting small displacements, especially considering the frame rate has been increasing to an extend that the displacement between consecutive frames is far below one sample.

In Figure 3.7, where lateral displacement estimation within the rectangular region in Figure 3.4 is shown, it is clear that lateral estimation field from the proposed method is more smooth than other two methods. Statistics are shown in Figure 3.8, which is showing the estimated lateral displacement versus the true displacement in FieldII (left) and the standard deviation of three subsample estimators (right). The same trend can be observed from Figure 3.5 and Figure 3.8 (left) that the proposed method overestimates the positive displacement and underestimates the negative displacement while the curve fitting methods do the opposite. Figure 3.8 (right) is also consistent with the simulation result in Figure 3.6.

3.5 Conclusions

A lateral subsample estimator based on complex normalized cross correlation in ultrasound has been presented in this chapter. Mathematical proof of this method is shown and simulation is performed to compare the performance of this method with two common curve fitting techniques. The simulation results show that it is the most reliable algorithm in terms of bias and standard deviation. More sophisticated simulation in Field II also validates the proposed method.

Generalization of 1D problem to a higher dimensionality, e.g. 2D, is straightforward. In the 2D case, for example, the displacement estimation should be on the zero phase line of two complex cross correlation functions, one from Hilbert transformation in the axial direction and one from Hilbert transformation in the lateral direction. It will be covered by the next chapter.

Chapter 4

Two Dimensional Speckle Tracking Methods

4.1 Introduction

Displacement estimation in sequences of ultrasound echo signals is essential for a wide range of practical applications, e.g., flow estimation [73, 96], tissue velocity estimation [89, 99], tissue elastography [5, 44], radiation force imaging [82], target tracking during image-guided procedures [98] and many other applications. The performance of these applications intimately ties to the performance of the displacement estimation. For example, a temperature map using ultrasound is the foundation of guided tissue heating with and without control. The temperature map comes from the temporal accumulation of a sequence of spatially derivative of displacement fields. An estimator with a high standard deviation produces a high noisy displacement field, thus rendering a noisy temperature map. An estimator with a high bias results in a shifted temperature level. Therefore, an accurate displacement estimator has a significant implications in many applications.

As introduced in chapter 2 and chapter 3, where subsample estimation was investigated in the axial direction and in the lateral direction, respectively, zero phase crossing is the most robust techniques. However, one directional motion tracking has limitations for many applications. For example, in the blood flow or tissue motion estimation,

motion tracking along beam direction, i.e., the axial direction results in unknown motion in the lateral direction [50]. However, the motion in the lateral direction could be significant. In the elastography application, tracking only in the axial direction results in loss of strain estimation in the lateral estimation. Two-dimensional temperature estimation relies on performance of delay estimation in both the axial and lateral directions [51–53]. Moreover, there are very limited research conducted in the lateral displacement estimation compared to the axial direction.

A number of techniques have been explored for the 2D displacement estimation. Interpolation in 1D estimation can be extended into a 2D estimation in a straightforward manner. 2D displacement can be solved by two independently 1D estimation, i.e., the axial shift being estimated by locating the second kernel only on the axial direction and the lateral shift only on the lateral direction. A number of 1D pattern matching interpolation methods such as parabolic fitting [39], spline fitting [42], grid slope [37], cosine fitting [20], zero padding, and reconstructive methods have been introduced and thoroughly investigated in the literature. Despite of its inherent estimation error if the correlation function is distorted, it is widely used due to easy implementation and low computational cost. [13] estimated the displacement by locating the maximum of the 2D cross correlation function defined in Equation 1.3. The discretized 2D cross correlation necessitates a subsample estimator with higher and higher frame rates. An iterative technique of finding maximum location was proposed in the literature. The 3 by 3 centered at the integer maximum location was interpolated and iteratively use the maximum location in the lateral direction to track the maximum location in the axial direction or vice-versa. A demandingly high interpolation in the lateral direction has to be used in order to have a moderately smooth displacement field because of coarse resolution in the lateral direction. Researchers also proposed extended spline-based algorithm, which was shown to excel in a number of 2D subsample estimators in terms of bias and standard deviation. The analytic property and high sampling frequency in the axial direction of the echo data has lead to efficient and robust methods [70], which was shown to have a better performance. 2D phase-coupled estimator, based on the gradient of the magnitude and the zero-phase crossing of the 2D complex correlation of the analytic signals, was first introduced in [58]. This approach with a minimal lateral interpolation achieved subsample smooth and accurate lateral displacement estimates

highly free of quantization effects due to interpolation. Application of the new technique to simultaneous estimation of tissue motion and flow velocity was demonstrated in [99] and an extension of this method was shown in [113].

In this chapter, we extend our previous work in the 1D zero phase crossing algorithm into a 2D scenario. In this method, instead of interpolating the magnitude of cross correlation, the subsample estimation is accomplished by finding the crossing of zero phase of complex cross correlation function. The zeros phase crossing in the axial direction can be easily found due to the fact that the phase of complex cross correlation function is linear. However particular attention has to be paid to the case in the lateral direction. Even though the same idea can be applied in the lateral direction, phase of the zero phase line is not necessarily linear. Therefore, performance in the lateral direction is expected not as good as the case in the axial direction. The mathematical derivation of this method is described in Section 4.2. Since the zero phase crossing can be found analytically, this estimator is not subject to sampling quantization and therefore can be categorized as a continuous time-delay estimator. The detailed performance of this method compared with other estimators is presented in Section 4.4.

Experiments using Ultrasonix SonixRP ultrasound machine are used to investigate the performance of these estimators. A linear array moving at a constant speed controlled by a programmed motor is used to collect RF frames from a fabricated phantom.

This chapter is organized as follows: Section 4.2 presents theory of the zero phase crossing algorithm. Simulation and results & discussion are included in Section 4.3 and Section 4.4 respectively. Experimental results are shown in Section 4.5. Finally, conclusions are given in Section 4.6.

4.2 Theory

4.2.1 Two Dimensional Sub-Sample Estimator

In this section, the zero phase crossing algorithm is developed using a 2D model of the received signal, $s(x, z)$, from a 2-D region with spatial coordinates x and z representing the lateral and axial directions, respectively. Assuming the 2D region has undergone a

translation d_x and d_z between two imaging frames, the displaced signal will be:

$$r(x,z) = s(x-d_x, z-d_z). \tag{4.1}$$

For simplicity, we use a separable model for $s(x,z)$ [1, 50]

$$s(x,z) = b(x)u(z)\sin(\omega_0 z), \tag{4.2}$$

where $b(x)$ and $u(z)$ are baseband signals in the lateral and axial directions, respecively. Note that there is a carrier frequency (ω_0) in the axial direction and no carrier frequency in the lateral direction.

Taking Hilbert transformation in the axial direction, the analytic signals will be:

$$s_a(x,z) = b(x)u(z)e^{\omega_0 z}, \tag{4.3}$$

and

$$r_a(x,z) = b(x-d_x)u(z-d_z)e^{\omega_0(z-d_z)}. \tag{4.4}$$

The 2d complex normalized cross-correlation between $s_a(x,z)$ and $r_a(x,z)$ is:

$$R_a(\tau,\zeta) = \frac{\int_{-\infty}^{\infty}\int_{-\infty}^{\infty} s_a^*(x,z)r_a(x+\tau,z+\zeta)dzdx}{\sqrt{\int_{-\infty}^{\infty}\int_{-\infty}^{\infty}|s_a(x,z)|^2\,dzdx\int_{-\infty}^{\infty}\int_{-\infty}^{\infty}|r_a(x,z)|^2\,dzdx}}, \tag{4.5}$$

where

$$\begin{aligned}\int_{-\infty}^{\infty}\int_{-\infty}^{\infty}|s_a(x,z)|^2\,dzdx &= \int_{-\infty}^{\infty}\int_{-\infty}^{\infty}\left|b(x)u(z)e^{j\omega_0 z}\right|^2 dzdx \\ &= \int_{-\infty}^{\infty}\int_{-\infty}^{\infty}|b(x)u(z)|^2\,dzdx \\ &= \int_{-\infty}^{\infty}|b(x)|^2\,dx\int_{-\infty}^{\infty}|u(z)|^2\,dz,\end{aligned} \tag{4.6}$$

and

$$\int_{-\infty}^{\infty}\int_{-\infty}^{\infty}|r_a(x,z)|^2\,dzdx = \int_{-\infty}^{\infty}|b(x)|^2\,dx\int_{-\infty}^{\infty}|u(z)|^2\,dz. \tag{4.7}$$

In addition,

$$\begin{aligned}&\int_{-\infty}^{\infty}\int_{-\infty}^{\infty}s_a^*(x,z)r_a(x+\tau,z+\zeta)dzdx \\ &= \int_{-\infty}^{\infty}\int_{-\infty}^{\infty}b(x)b(x+\tau-d_x)\cdot u(z)u(z+\zeta-d_z)e^{j\omega_0(\zeta-d_z)}dzdx \\ &= \int_{-\infty}^{\infty}b(x)b(x+\tau-d_x)dx\cdot\int_{-\infty}^{\infty}u(z)u(z+\zeta-d_z)e^{j\omega_0(\zeta-d_z)}dz.\end{aligned} \tag{4.8}$$

Then $R_a(\tau, \zeta)$ can be rewritten as,

$$R_a(\tau, \zeta) = c_{a,x}(\tau) * c_{a,z}(\zeta), \tag{4.9}$$

where

$$c_{a,x}(\tau) = \frac{\int_{-\infty}^{\infty} b(x)b(x+\tau-d_x)dx}{\int_{-\infty}^{\infty} |b(x)|^2 dx}, \tag{4.10}$$

$$c_{a,z}(\zeta) = \frac{\int_{-\infty}^{\infty} u(z)u(z+\zeta-d_z)dz}{\int_{-\infty}^{\infty} |u(z)|^2 dx} \cdot e^{j\omega_0(\zeta-d_z)}. \tag{4.11}$$

Note that $c_{a,x}(\tau)$ is a real function and $c_{a,z}(\zeta)$ is a complex function. By Cauchy-Schwarz inequality, $c_{a,x}(\tau)$ is maximized when $\tau = dx$ and $|c_{a,z}(\zeta)|$ when $\zeta = dz$. Therefore, $|R_a(\tau, \zeta)|$ is maximized when $\tau = d_x$ and $\zeta = d_z$, and phase of $R_a(d_x, d_z)$ is zero. Then,

$$\begin{cases} \arg\max\limits_{(\tau,\zeta)} R_a(\tau, \zeta) = (d_x, d_z) \\ \angle R_a(d_x, d_z) = 0 \end{cases}, \tag{4.12}$$

i.e., the true displacement (d_x, d_z) is on the zero phase line of $R_a(\tau, \zeta)$. This conclusion is also derived in [58]

On the other hand, if taking Hilbert transformation in the lateral direction, the analytic signals will be:

$$s_l(x, z) = e(x)e^{j\Phi(x)}u(z)\sin(\omega_0 z), \tag{4.13}$$

and

$$r_l(x, z) = e(x - d_x)e^{j\Phi(x-d_x)}u(z - d_z)\sin(\omega_0(z - d_z)). \tag{4.14}$$

The normalized 2d complex cross-correlation between $s_l(x, z)$ and $r_l(x, z)$ is:

$$\begin{aligned} &R_l(\tau, \zeta) \\ &= \frac{\int_{-\infty}^{\infty}\int_{-\infty}^{\infty} s_l^*(x, z)r_l(x+\tau, z+\zeta)dzdx}{\sqrt{\int_{-\infty}^{\infty}\int_{-\infty}^{\infty} |s_l(x, z)|^2 dzdx \int_{-\infty}^{\infty}\int_{-\infty}^{\infty} |r_l(x, z)|^2 dzdx}}, \end{aligned} \tag{4.15}$$

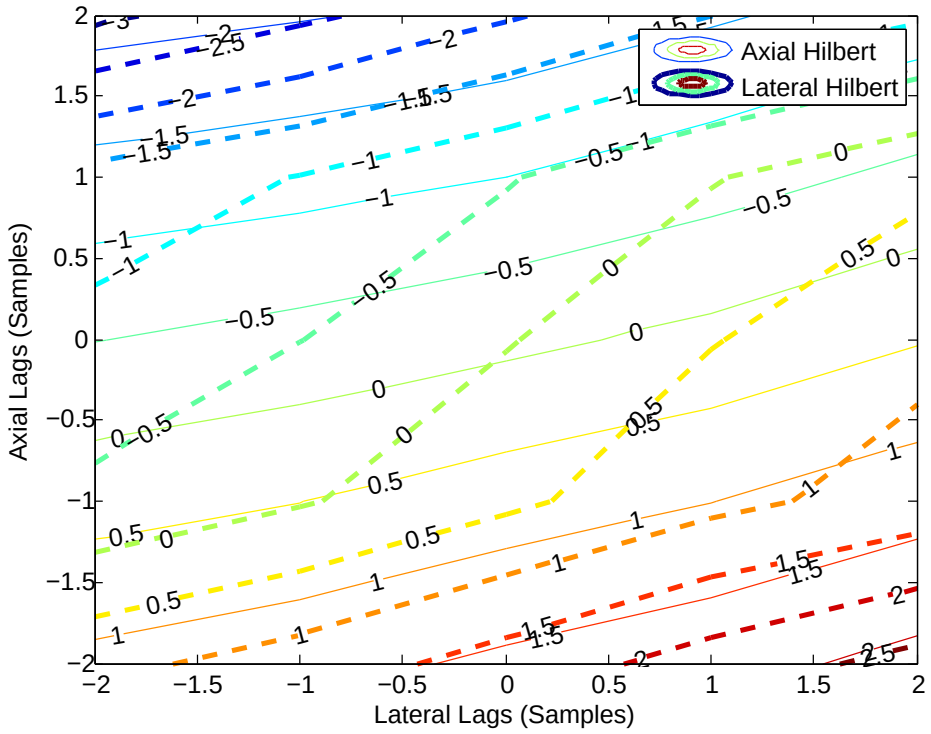

Figure 4.1: Phase Contours of the 2-D complex NCCs. The thin continuous line indicates the NCC from the axial Hilbert transformation and the bold dashed line indicates the NCC from the lateral Hilbert transformation.

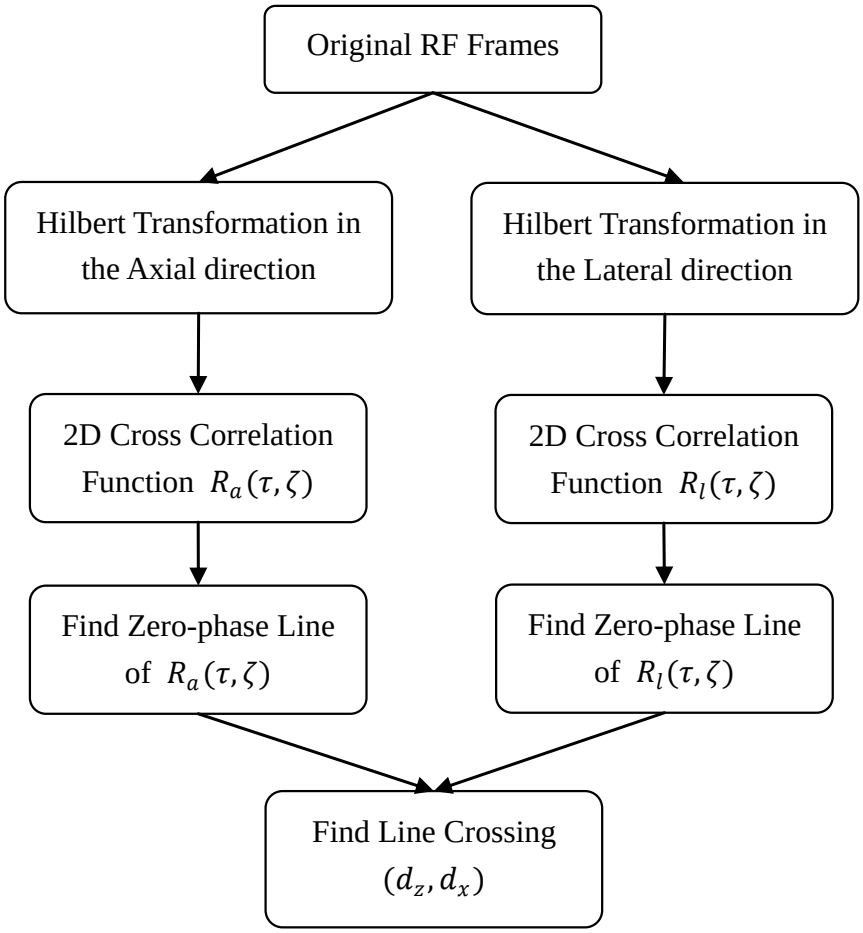

Figure 4.2: The 2D zero-phase crossing algorithm flow-chart. It consists of calculating two parallel cross correlation functions and then locating intersection point of two zero phase lines.

where

$$\begin{aligned}
&\int_{-\infty}^{\infty}\int_{-\infty}^{\infty}|s_l(x,z)|^2\,dzdx \\
&=\int_{-\infty}^{\infty}\int_{-\infty}^{\infty}\left|e(x)e^{j\Phi(x)}u(z)\sin(\omega_0 z)\right|^2 dzdx \\
&=\int_{-\infty}^{\infty}\int_{-\infty}^{\infty}|e(x)|^2\,|u(z)\sin(\omega_0 z)|^2\,dzdx \\
&=\int_{-\infty}^{\infty}|e(x)|^2\,dx\int_{-\infty}^{\infty}|u(z)\sin(\omega_0 z)|^2\,dz,
\end{aligned} \tag{4.16}$$

and

$$\int_{-\infty}^{\infty}\int_{-\infty}^{\infty}|r_l(x,z)|^2\,dzdx=\int_{-\infty}^{\infty}|e(x)|^2\,dx\int_{-\infty}^{\infty}|u(z)\sin(\omega_0 z)|^2\,dz. \tag{4.17}$$

$$\begin{aligned}
&\int_{-\infty}^{\infty}\int_{-\infty}^{\infty}s_l^*(x,z)r_l(x+\tau,z+\zeta)dzdx \\
&=\int_{-\infty}^{\infty}\int_{-\infty}^{\infty}e(x)e^{-j\Phi(x)}u(z)\sin(\omega_0 z)e(x+\tau-d_x)\cdot \\
&e^{j\Phi(x+\tau-d_x)}u(z+\zeta-d_z)\sin(\omega_0(z+\zeta-d_z))dzdx \\
&=\int_{-\infty}^{\infty}e(x)e(x+\tau-d_x)e^{-j\Phi(x)}e^{j\Phi(x+\tau-d_x)}dx\cdot \\
&\int_{-\infty}^{\infty}u(z)u(z+\zeta-d_z)\sin(\omega_0 z)\sin(\omega_0(z+\zeta-d_z))dz.
\end{aligned} \tag{4.18}$$

Then $R_l(\tau,\zeta)$ can be rewritten as

$$R_l(\tau,\zeta)=c_{l,x}(\tau)*c_{l,z}(\zeta), \tag{4.19}$$

where

$$c_{l,x}(\tau)=\frac{\int_{-\infty}^{\infty}e(x)e(x+\tau-d_x)e^{j(\Phi(x+\tau-d_x)-\Phi(x))}}{\int_{-\infty}^{\infty}|e(x)|^2\,dx}, \tag{4.20}$$

and

$$c_{l,z}(\zeta)=\frac{\int_{-\infty}^{\infty}u(z)u(z+\zeta-d_z)\sin(\omega_0 z)\sin(\omega_0(z+\zeta-d_z))}{\int_{-\infty}^{\infty}|u(z)\sin(\omega_0 z)|^2\,dx}. \tag{4.21}$$

Note that $c_{l,x}(\tau)$ is a complex function while $c_{l,z}(\zeta)$ is a real function. $c_{l,z}(\zeta)$ is maximized when $\zeta = d_z$. By Cauchy-Schwarz inequality,

$$\begin{aligned} |c_{l,x}(\tau)| &= \frac{\left|\int_{-\infty}^{\infty} e(x)e(x+\tau-d_x)e^{j(\Phi(x+\tau-d_x)-\Phi(x))}dx\right|}{\int_{-\infty}^{\infty}|e(x)|^2\,dx} \\ &\leq \frac{\int_{-\infty}^{\infty}\left|e(x)e(x+\tau-d_x)e^{j(\Phi(x+\tau-d_x)-\Phi(x))}\right|dx}{\int_{-\infty}^{\infty}|e(x)|^2\,dx} \\ &= \frac{\int_{-\infty}^{\infty}|e(x)e(x+\tau-d_x)|\,dx}{\int_{-\infty}^{\infty}|e(x)|^2\,dx} \\ &\leq 1. \end{aligned} \tag{4.22}$$

So $|c_{l,x}(\tau)|$ is maximized when $\tau = d_x$. Therefore, $R_l(\tau,\zeta)$ is maximized when $\tau = d_x$ and $\zeta = d_z$, i.e.

$$\arg\max_{(\tau,\zeta)} R_l(\tau,\zeta) = (d_x, d_z). \tag{4.23}$$

so $|c_{l,x}(\tau)|$ is maximized when $\tau = d_x$. Therefore, $R_l(\tau,\zeta)$ is maximized when $\tau = d_x$ and $\zeta = d_z$, and phase of $R_l(d_x,d_z)$ is zero. Then,

$$\begin{cases} \arg\max_{(\tau,\zeta)} R_l(\tau,\zeta) = (d_x,d_z) \\ \angle R_l(d_x,d_z) = 0 \end{cases}, \tag{4.24}$$

i.e., the true displacement (d_x, d_z) is on the zero phase line of $R_l(\tau,\zeta)$.

Figure 4.2 depicts the flowchart of the proposed 2D zero-crossing method. An interesting property is that the algorithm consists of calculations of two zero phase lines, which can be simultaneously computed. So real-time implementation of this algorithm is feasible.

Since (d_x, d_z) is on the zero phase lines of $R_a(\tau,\zeta)$ and $R_l(\tau,\zeta)$, we can estimate (d_x, d_z) by using the intersection point of these two zero phase lines. For example, Fig. **??** shows phase contours of two complex NCCs, one from the axial Hilbert transformation and the other from the lateral Hilbert transformation. The intersection point of two zero phase lines is the displacement estimate. Figure **??** depicts the flowchart of the proposed 2D zero-crossing method. An interesting property is that the algorithm consists of parallel calculations of two zero phase lines, which may be an advantage when high performance parallel computing is used for real-time implementation.

4.3 Simulation

4.3.1 Subsample Estimators

Let $R(\tau, \zeta)$ be the discrete 2D pattern matching function between the windowed reference and the displaced echo signal over a predefined search region. Note we do not take any Hilbert transformation in neither axial nor later direction. Given $R(\tau, \zeta)$ the coarse axial d_z and lateral d_x estimates of the motion in the axial (z) and the lateral (x) directions are achieved by locating the maximum of the 2D discrete pattern matching function $R(\tau, \zeta)$. The estimates d_x and d_z are given by

$$(d_x, d_z) = \arg\max_{(\tau,\zeta)} R(\tau, \zeta), \tag{4.25}$$

which has a similar form to Equation 4.23. The difference is that $R(\tau, \zeta)$ is calculated from the original RF signals while $R_a(\tau, \zeta)$ and $R_l(\tau, \zeta)$ comes from the Hilbert transformed signals. Although there are a lot of subsample estimators in literature discussed in Section 4.1, the zero phase based algorithm derived in Section 4.2 was compared to the following subsample estimators:

- Phase coupled Method [58]
- Polynomial fitting (f9) to NCC in [32]
- Parabolic fitting (PF) to NCC

4.3.2 Independent 1D Subsample Estimators

These methods are the most commonly used techniques to estimate the subsample motion in 2D problems. For the purpose of comparison in this chapter, (i) the three point 1D parabolic fitting where the axial and lateral sub-sample shifts are estimated independently with a certain fitting function. The subsample estimators can be found by using

$$\begin{aligned} d_z &= \arg\max_{\tau} f_a(\tau) \\ d_x &= \arg\max_{\zeta} f_l(\zeta) \end{aligned} \tag{4.26}$$

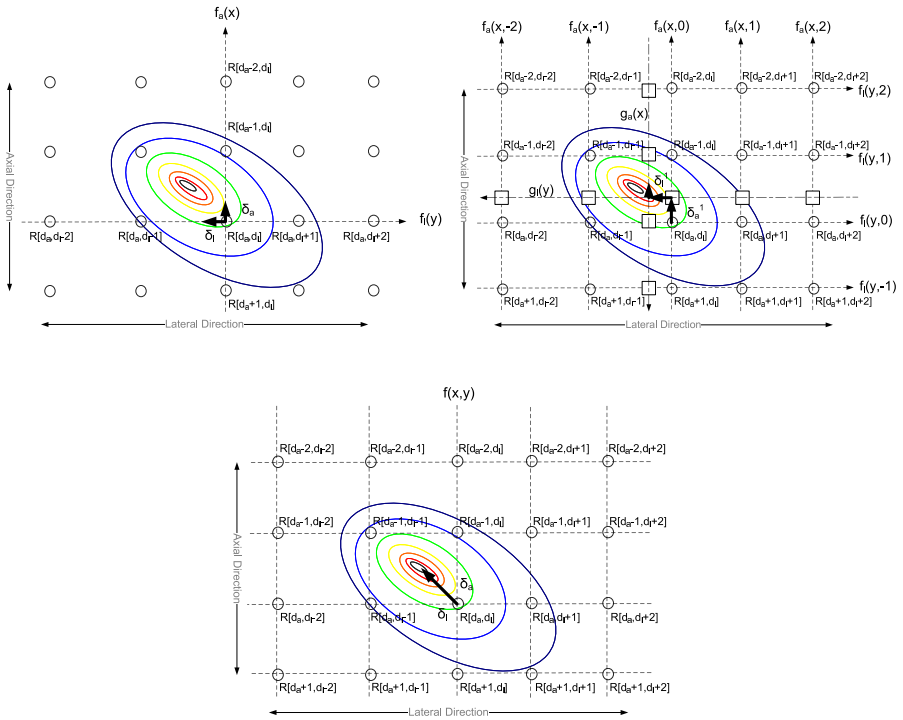

Figure 4.3: Curve fitting methods. The top left one is 1D independent fitting method. The top right is the iterative 1D fitting method. The bottom is the 2D polynomial surface fitting method.

where $f_a(\tau)$ and $f_l(\zeta)$ are the correlation function along axial direction and lateral direction respectively. f can be a form of parabolic function or cosine function. Detailed expressions and derivations can be found in 2.2.

4.3.3 2D Surface Fitting Methods

In a more general approach, a 2D function can be fitted to be a discrete matching function in both the axial and the lateral directions. Joint estimation with subsample accuracy can be then achieved in both directions by finding the peak of the fitted function analytically.

Let $f(x, z)$ be a 2D interpolation function passing through the 2D pattern matching function at (d_x, d_z) and its neighbors (i.e. $R(\tau+i, \zeta+j)$ where $i \in \{0, \pm1, \pm2, ..., \pm M_a\}$, $j \in \{0, \pm1, \pm2, ..., \pm M_l\}$). The subsample motion estimates (d_z, d_x) are computed jointly from the corresponding 2D interpolation function as shown in Equation 4.25.

Several 2D pattern matching function are proposed in [32] as follows.

$$\begin{aligned} f_9(x,z) = {} & a_1 + a_2x + a_3z + a_4xz + a_5x^2 + a_6z^2 + a_7xz^2 \\ & + a_8x^2z + a_9x^2z^2 \end{aligned} \tag{4.27}$$

$$\begin{aligned} f_{16}(x,z) = {} & a_1 + a_2x + a_3z + a_4xz + a_5x^2 + a_6z^2 + a_7xz^2 \\ & + a_8x^2z + a_9x^2z^2 + a_10x^3 + a_{11}x^3z + a_{12}x^3z^2 \\ & + a_{13}z^3 + a_{14}xz^3 + a_{15}x^2z^3 + a_{16}x^3z^3 \end{aligned} \tag{4.28}$$

$$\begin{aligned} f_{25}(x,z) = {} & a_1 + a_2x + a_3z + a_4xz + a_5x^2 + a_6z^2 + a_7xz^2 \\ & + a_8x^2z + a_9x^2z^2 + a_10x^3 + a_{11}x^3z + a_{12}x^3z^2 \\ & + a_{13}z^3 + a_{14}xz^3 + a_{15}x^2z^3 + a_{16}x^3z^3 \\ & + a_{17}x^4 + a_{18}x^4z + a_{19}x^4z^2 + a_{20}x^4z^3 \\ & + a_{21}z^4 + a_{22}xz^4 + a_{23}x^2z^4 + a_{24}x^3z^4 + a_{25}x^4z^4 \end{aligned} \tag{4.29}$$

$f_9(x, z)$, $f_{16}(x, z)$ and $f_{25}(x, z)$ exploit the same idea that fitting a discrete 2D grid with a continuous function and then finding the peak of the fitted function. Specifically,

coefficients a_i of $f_9(x,z)$ can be solved by fitting to 3 by 3 grid around the maximum of the discrete pattern matching function and a_i of $f_{16}(x,z)$ and $f_{25}(x,z)$ has to use the 5 by 5 grid around the maximum of the discrete pattern matching function. For example, 25 equation can be derived from the 5 by 5 grid to calculate $a_i, i \in \{0,1,...,15\}$ of $f_{16}(x,z)$. Least-squares fitting of the data points is achieved by pseudo-inverse technique. One we have the coefficients of $f_i(x,z)$, the location of the maximum of the fitted 2D polynomial is found by setting $\nabla f_i(x,z) = 0$. Newton's iterative method is used to solve $\nabla f_i(x,z) = 0$.

$$\begin{bmatrix} x \\ z \end{bmatrix}_{k+1} = \begin{bmatrix} x \\ z \end{bmatrix}_{k} - \begin{bmatrix} \frac{\partial f}{\partial x \partial x} & \frac{\partial f}{\partial x \partial z} \\ \frac{\partial f}{\partial z \partial x} & \frac{\partial f}{\partial z \partial z} \end{bmatrix}^{-1} \begin{bmatrix} \frac{\partial f}{\partial x} \\ \frac{\partial f}{\partial z} \end{bmatrix} \Bigg|_{\begin{bmatrix} x_k \\ y_k \end{bmatrix}} \tag{4.30}$$

4.3.4 Simulation Method

A series of simulations were performed in MATLAB (MathWorks Inc., Natick, MA). The bias and standard deviation of the delay estimators are the most common merits of performance and were calculated using Equation 4.32 and Equation 4.33. The default simulation parameter settings are listed in Table 4.1.

Besides the settings above, subsample delays were varied from -0.5 to 0.5 samples in a step of 0.1 samples, so that a total of 11 different delays were evaluated for each subsample estimator in each direction. Therefore 11 by 11 estimation grid can be generated.

Table 4.1: Default values used to generate $psf(x,z)$

Parameter	Value
Azimuthal aperture width (D)	20 mm
Depth in tissue (x_r)	50 mm
Scaling factor (A)	1
Wavelength at the system center frequency (λ)	0.308 mm
System center frequency (f_0)	5.0 MHz
Sampling frequency (f_s)	40.0 MHz
Speed of sound (c)	1540 m/s
Pulse length (σ_z)	200 ns

Signal noise ratio	40 dB

A sinc squared-shaped point spread function was chosen and given by [1]:

$$psf(x,z) = A(\frac{\sin(\frac{\pi Dx}{\lambda x_r})}{(\frac{\pi Dx}{\lambda x_r})})^2 e^{-\frac{z^2}{2\sigma_z^2}} \sin(\omega_0 z), \tag{4.31}$$

where x and z are representing the lateral and axial direction respectively.

The flow of simulation is listed below.

1. The point spread function $psf(x,z)$ in Equation 4.31 was sampled by a 2D spatial grid $[x_G, z_G]$ with x_G ranging from -2mm to 2mm at a step of $\frac{\lambda x_r}{lD}$ and z_G ranging from $-5\sigma_z$ to $5\sigma_z$ at a frequency of 40MHz, where the resolution length is $\frac{\lambda x_r}{D}$, l is the number of samples per resolution length and l is set 4 by default. The sampled $psf(x,z)$ is $psf(N_x, N_z)$.

2. $psf(N_x, N_z)$ was convolved with a 1000 by 200 point Gaussian random matrix with mean of 0 and standard deviation of 1 to generate the pre-compressed signal.

3. The point spread function $psf(x,z)$ in Equation 4.31 is sampled by a shifted spatial grid $[x_G + x_d, z_G + z_d]$, where (x_d, z_d) is the subsample displacement which is to be estimated. The newly sampled $psf(x,z)$ is $psf'(N_x, N_z)$.

4. $psf'(N_x, N_z)$ was convolved with the same 1000 by 200 Gaussian random matrix to generate the post-compressed signal.

5. The pre- and post-compressed signals were added with a Gaussian white noise to generate echo signals with different signal-to-noise-ratios (SNRs). Then various subsample estimators were implemented to calculate the displacement between pre- and post-compressed signals.

6. Bias and standard deviation were computed by Equation 4.32 and Equation 4.33,

$$b(\hat{\Delta}) = \frac{1}{N}\sum_{k=1}^{N}(\hat{\Delta}[k] - \Delta[k]) \tag{4.32}$$

$$\sigma(\hat{\Delta}) = \sqrt{\frac{1}{N}\sum_{k=1}^{N}(\hat{\Delta}[k] - \frac{1}{N}\sum_{k=1}^{N}\hat{\Delta}[k])^2} \tag{4.33}$$

where N is the total number of estimates, $\hat{\Delta}[k]$ is the estimated time delays and $\Delta[k]$ is the true time delays.

4.4 Simulation Results and Discussion

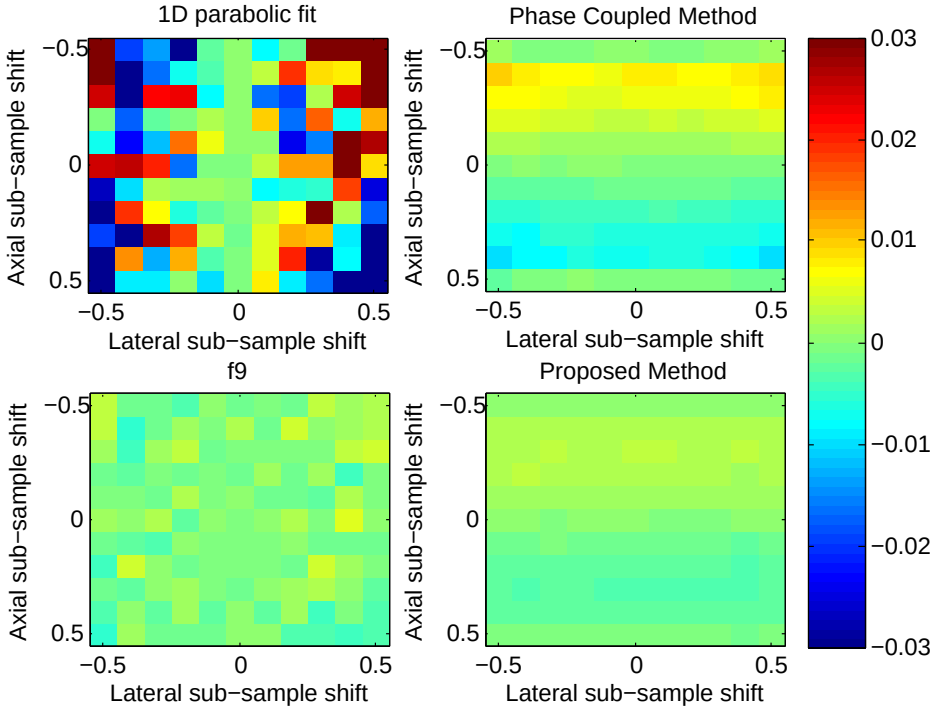

Figure 4.4: Bias in the axial direction of different delay estimators as a function of sub-sample shift on the 2D grid. A 39 by 164 estimation matrix was generated to calculate mean and standard deviation of each estimator. The resolution in the axial and lateral direction is 19.2μm and 192.5μm respectively.

Figure 4.4 shows the bias in the axial direction of the proposed algorithm and other sub-sample estimators as a function of the sub-sample displacement. The method of generating a known sub-sample displacement was presented in Section 4.3. The proposed algorithm outperforms other estimators across the entire range of sub-sample

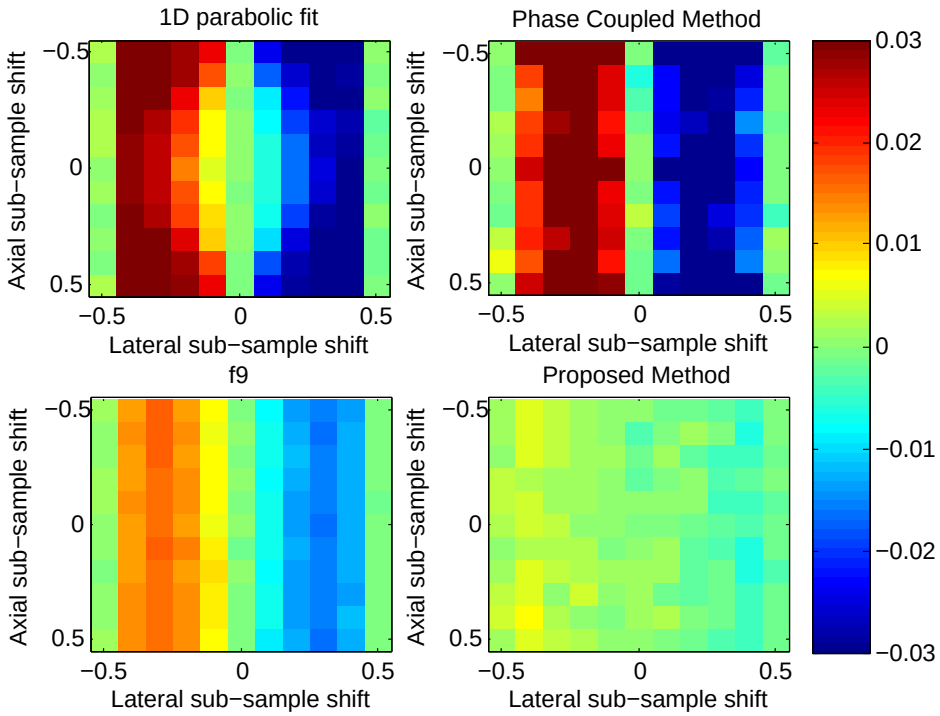

Figure 4.5: Bias in the lateral direction of different delay estimators as a function of sub-sample shift on the 2D grid. A 39 by 164 estimation matrix was generated to calculate mean and standard deviation of each estimator. The resolution in the axial and lateral direction is 19.2μm and 192.5μm respectively.

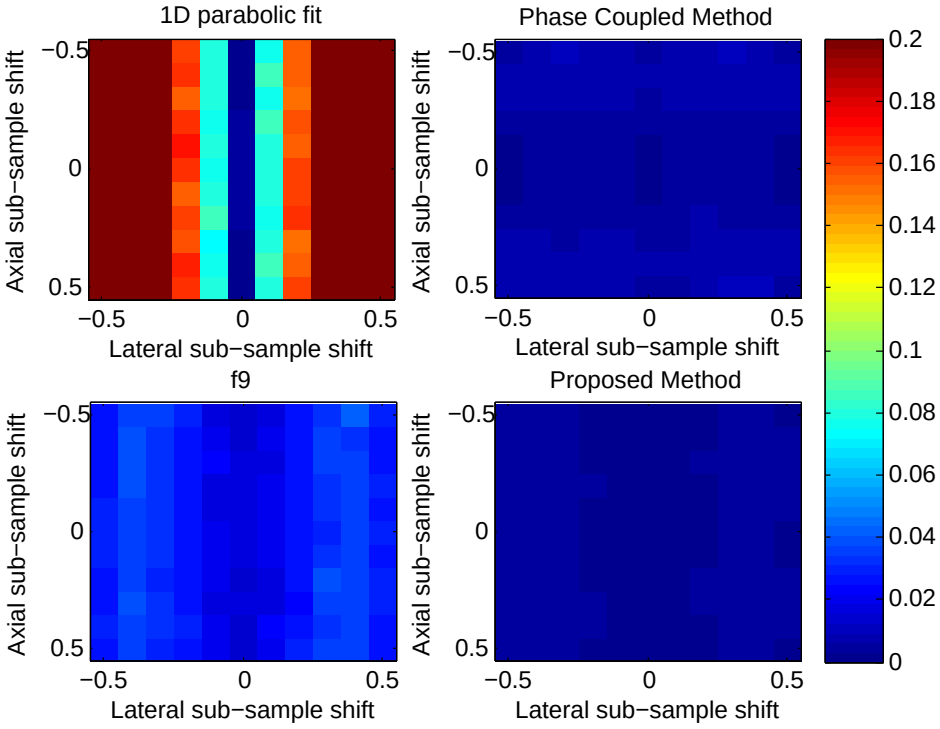

Figure 4.6: Standard deviation in the axial direction of different delay estimators as a function of sub-sample shift on the 2D grid. A 39 by 164 estimation matrix was generated to calculate mean and standard deviation of each estimator. The resolution in the axial and lateral direction is 19.2μm and 192.5μm respectively.

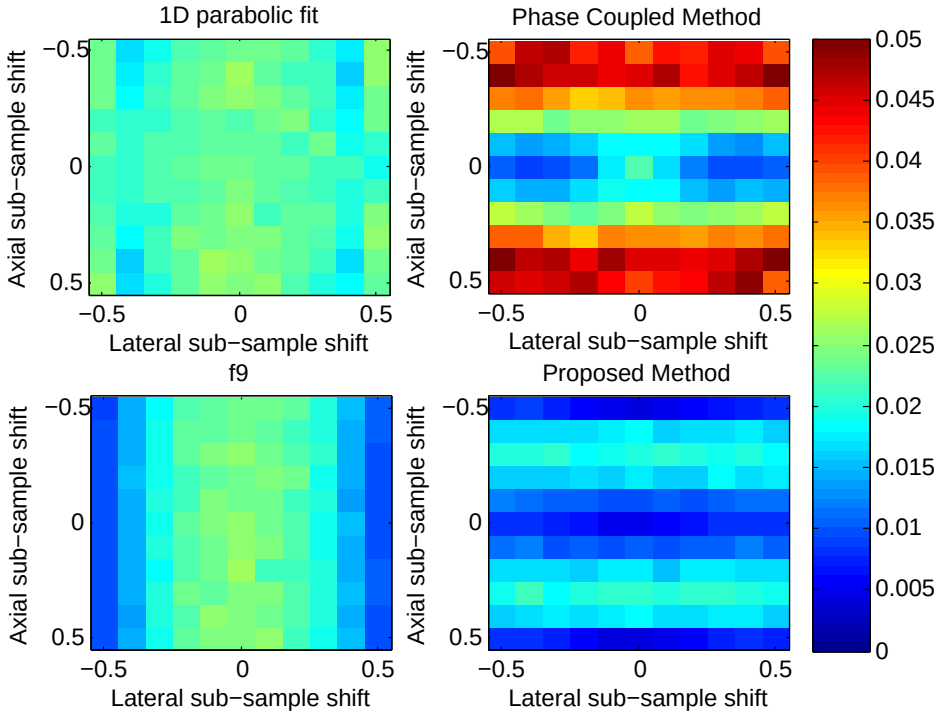

Figure 4.7: Standard deviation in the lateral direction of different delay estimators as a function of sub-sample shift on the 2D grid. A 39 by 164 estimation matrix was generated to calculate mean and standard deviation of each estimator. The resolution in the axial and lateral direction is 19.2μm and 192.5μm respectively.

displacement. The phase coupled method exhibits a similar performance with the proposed method in that both methods utilize the zero phase line in the axial direction. The comparison between the parabolic fitting method and f9 method is consistent with results in [32] that f9 method exhibits a much smaller bias magnitude than parabolic fit method. As also shown in [32], bias in the axial direction of curving fitting methods have a large magnitude within the region of large displacements. Therefore, in terms of smoothness of bias field, the proposed method and the phase coupled method are the best ones.

Figure 4.5 presents the bias in the lateral direction of all sub-sample estimators as a function of the sub-sample displacement. Parabolic fitting and the phase coupled methods perform relatively similiar. Nevertheless, the proposed method exhibits superior performance over the entire range. Interestingly, small lateral bias can be observed from curving fitting methods and f9 when the magnitude of lateral motion is 0.5 samples. Lateral motion has a more impact on estimation. For instance, when magnitude of lateral motion is about 0.3 samples, lateral bias is more or less independent of the axial motion.

In Figure 4.6 and Figure 4.7, where standard deviation in the axial direction and in the lateral direction are shown respectively, it is clear that lateral estimation field from the proposed method is more smooth than any other methods. Due to the analytic property in the axial direction, estimation in the axial direction is ubiquitously stable and accurate shown in Figure 4.4 and Figure 4.6. As expected, not as much superior performance is observed in the lateral direction, which results from non-analytic nature of the signal and linearization of the zero phase line. Another phenomenon is that the lateral standard deviation from the proposed method and the phase-coupled method is more dependent of axial motion whereas the lateral standard deviation from any other method is more dependent of lateral motion.

4.5 Experimental Materials and Methods

To study the application of the subsample estimators with real data, a uniform tissue-mimicking phantom (Tissue D) was fabricated using the method in [81]. The phantom was firmly secured in a large water container. A linear array probe (LA14-5/38) was

moved by a programmed motor at a constant speed. A commercial ultrasound scanner (Sonix RP, Ultrasonix, BC, Canada) loaded with custom designed program was used to collect RF frames. The center frequency of the transmit pulse of the probe is 7.5 MHz. The RF frames (56 A-lines) were collected at a frame rate of 82 and then streamlined to a controller PC through Gigabit Ethernet. Four different sets were collected, one with motor moved right by 10mm in 10sec (denoted by right10), one with motor moved left by 10mm in 10sec (denoted by left10), one with motor moved right by 10mm in 20sec (denoted by right20), and one with motor moved left by 10mm in 20sec (denoted by left20).

Figure 4.8 illustrates the experimental setup of frame collection (left) and the B-mode image (50 dB dynamic range) of the fabricated phantom (right). Note that there is a copper wire (coordinates of 4mm in the lateral direction and 32 mm in the axial direction) put in the phantom for motion reference. The linear array is not perfectly aligned in parallel with the phantom in order to induce motion in both the axial and lateral directions. Figure 4.9 shows the location of the wire at the beginning and end of frames. The wire has a motion of 9.97mm, which is very close to the ground truth 10mm.

Table 4.2: Statistics of accumulated displacement fields

Experiment	1d parabolic fit		PC method		f9		Proposed method	
	b	σ	b	σ	b	σ	b	σ
right10	-1.847	2.667	-4.228	2.007	-1.710	2.716	0.147	1.836
left10	-2.124	2.713	-4.588	1.854	-1.973	2.724	0.357	1.944
right20	-1.778	3.180	-4.316	2.199	-1.653	3.239	0.212	1.733
left20	-2.178	3.075	-4.703	1.929	-2.04	3.092	0.291	1.768

Figure 4.10 and Figure 4.11 show the histograms of the displacement field between frame 400 and frame 401 in the axial and lateral directions respectively from data set of right10. Only portion (depth between 11.6mm and 34.7mm) of the RF frames including the copper wire is used to calculate the displacement field. There is a flag set in the

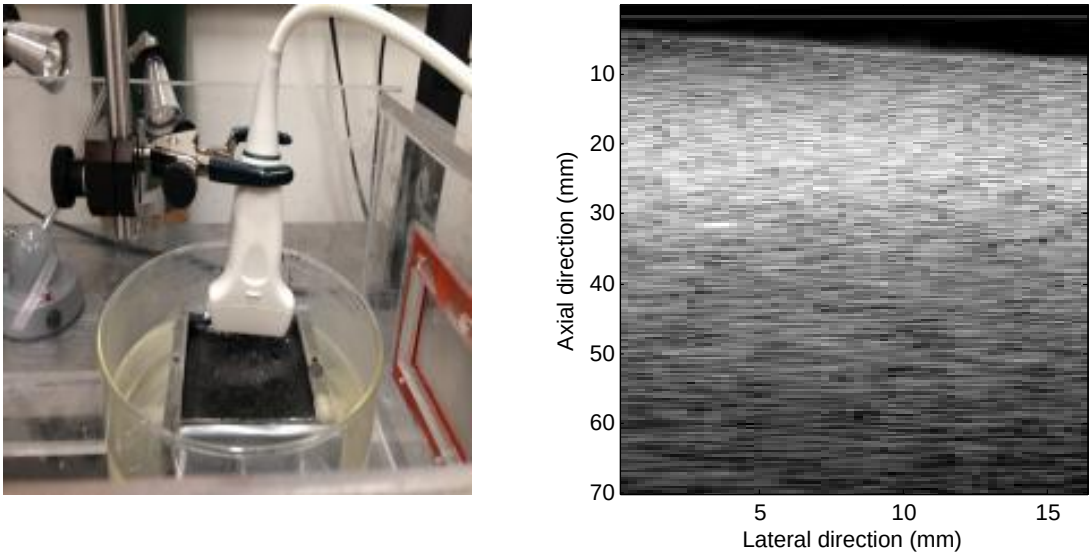

Figure 4.8: Experiment setup (left) and one sample B-mode image with 50 dB dynamic range (right).

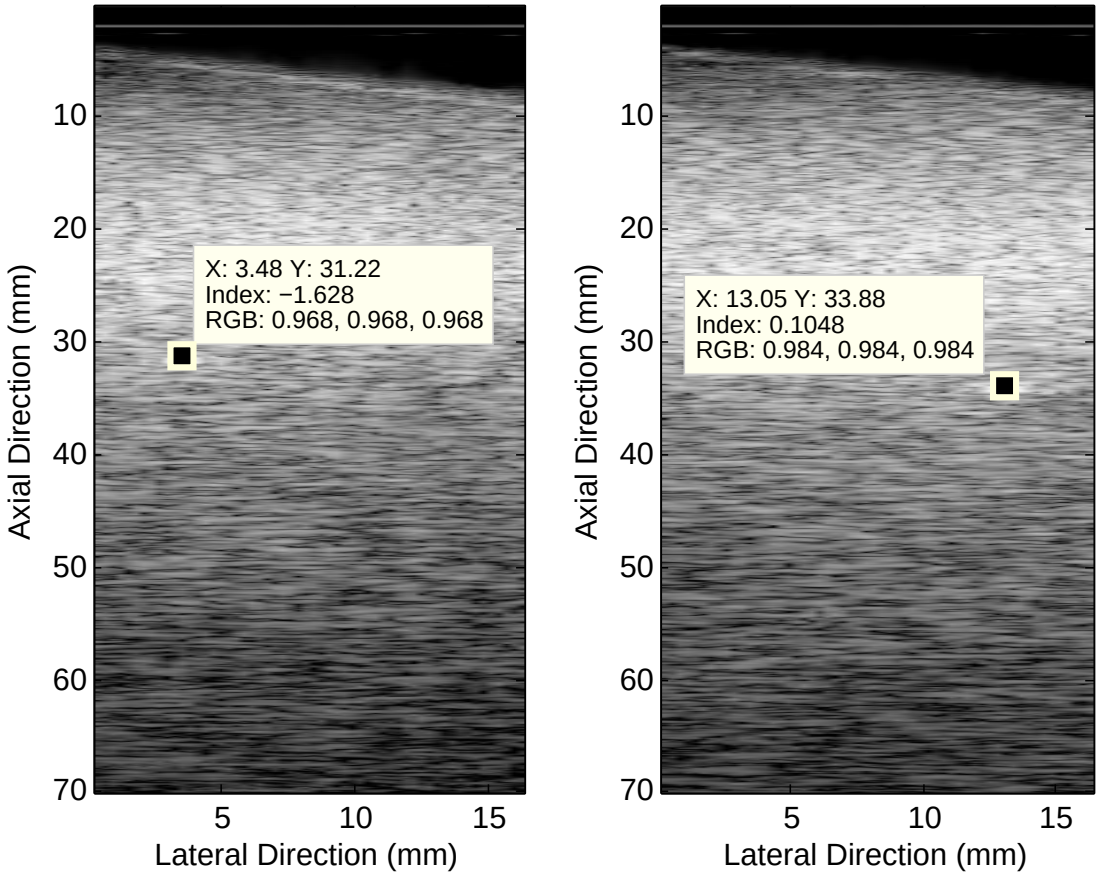

Figure 4.9: Reference motion inside the phantom.

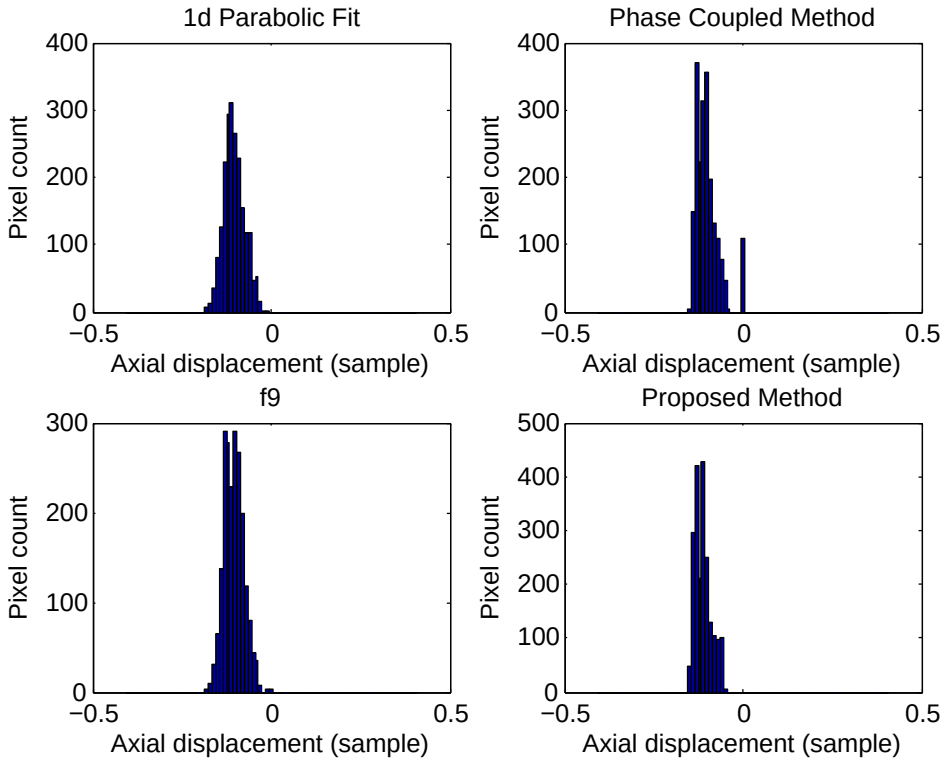

Figure 4.10: Histograms of the axial displacement fields between frame 400 and frame 401.

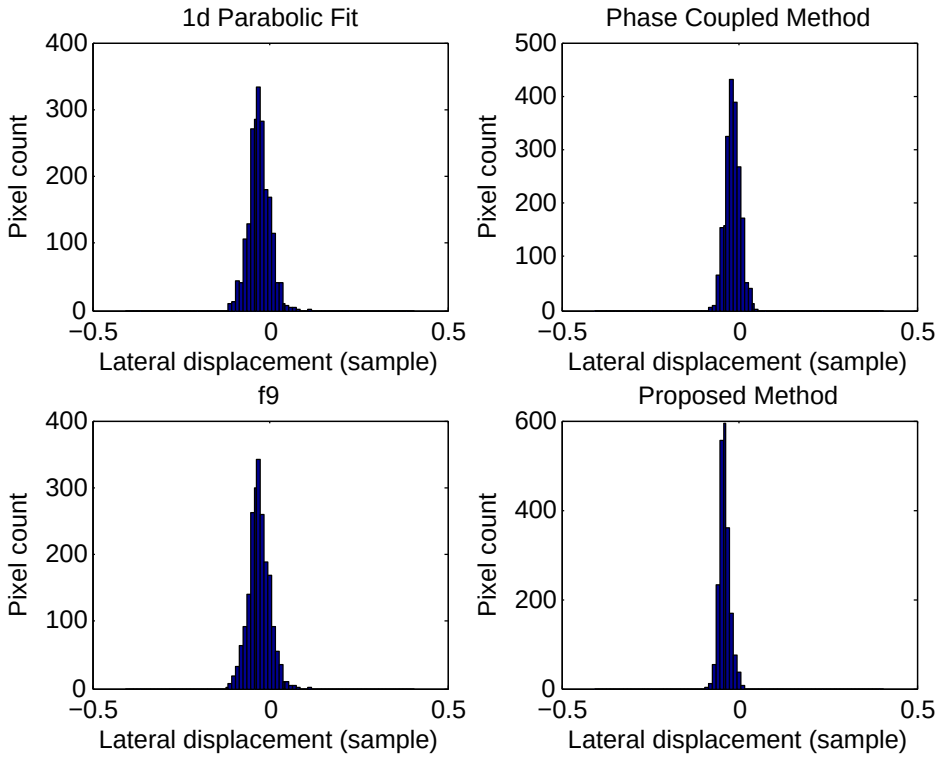

Figure 4.11: Histograms of the lateral displacement fields between frame 400 and frame 401.

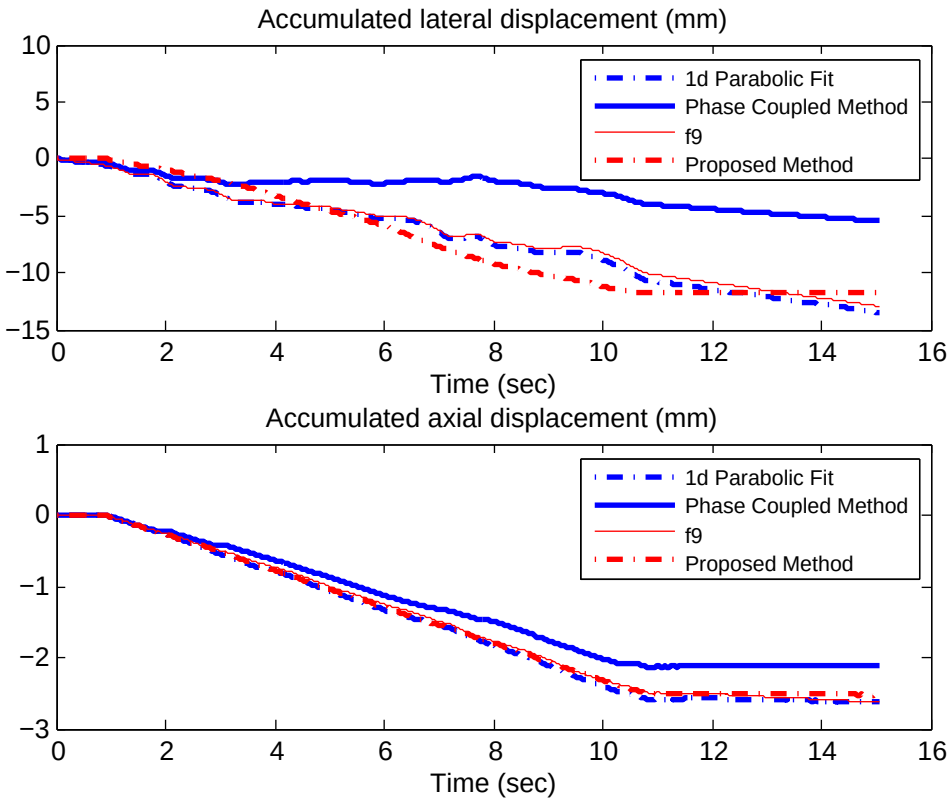

Figure 4.12: Estimated accumulated displacement from right10. Note that the true motion is 10mm.

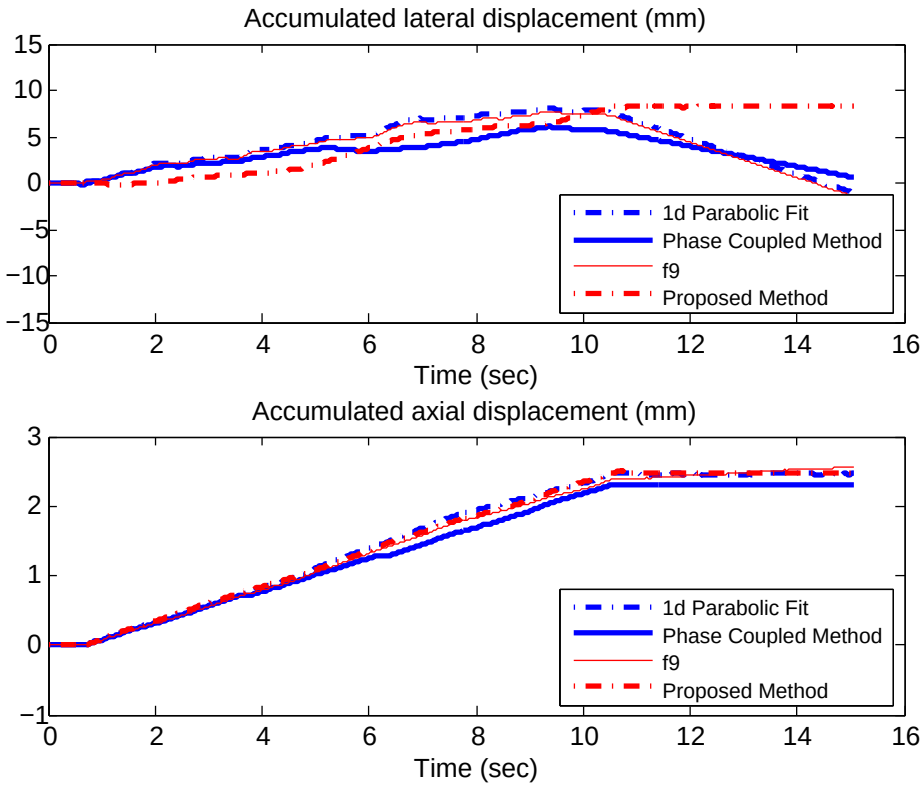

Figure 4.13: Estimated accumulated displacement from left10. Note that the true motion is 10mm.

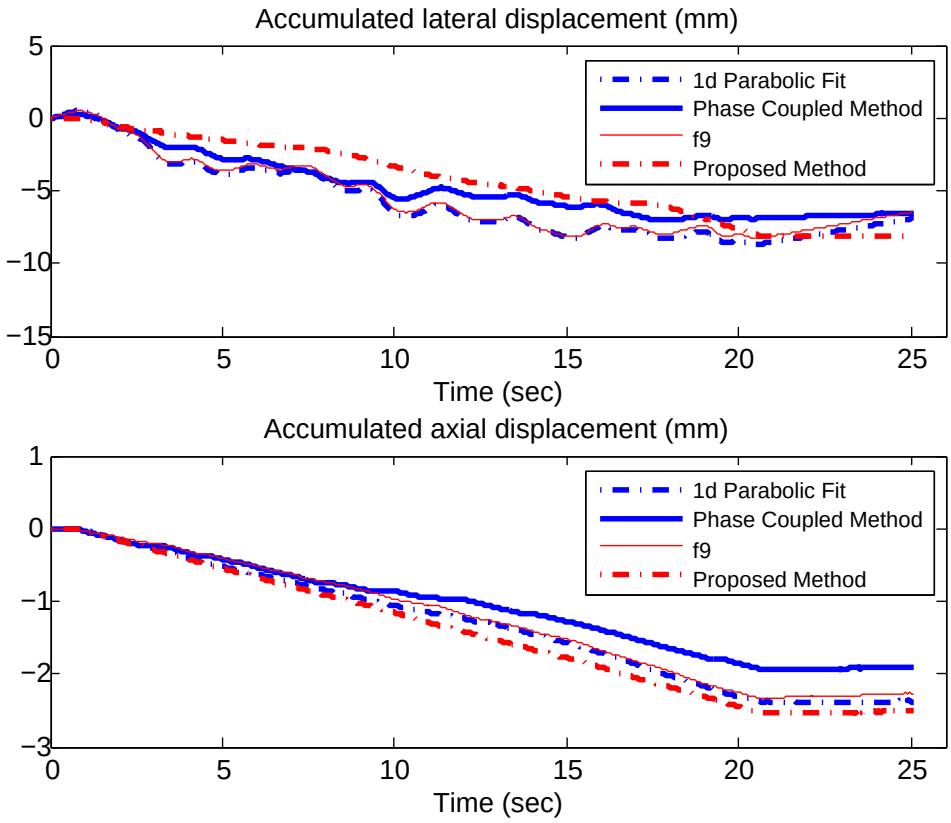

Figure 4.14: Estimated accumulated displacement from right20. Note that the true motion is 10mm.

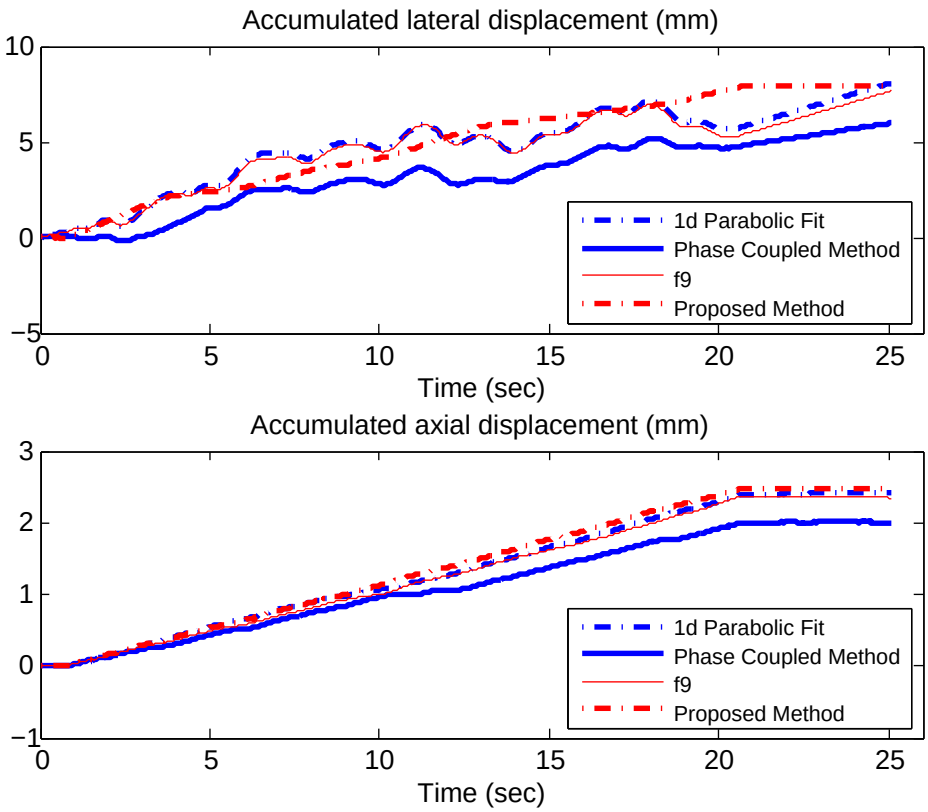

Figure 4.15: Estimated accumulated displacement from left20. Note that the true motion is 10mm.

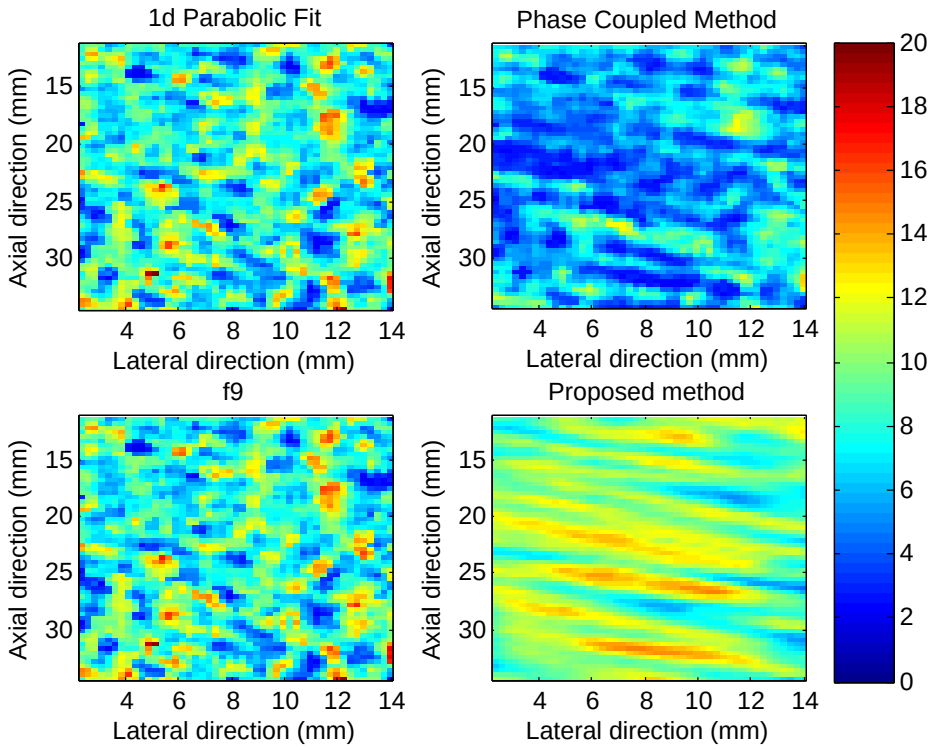

Figure 4.16: Estimated accumulated displacement fields of dataset right10 from different estimators. Note that the true motion is 10mm.

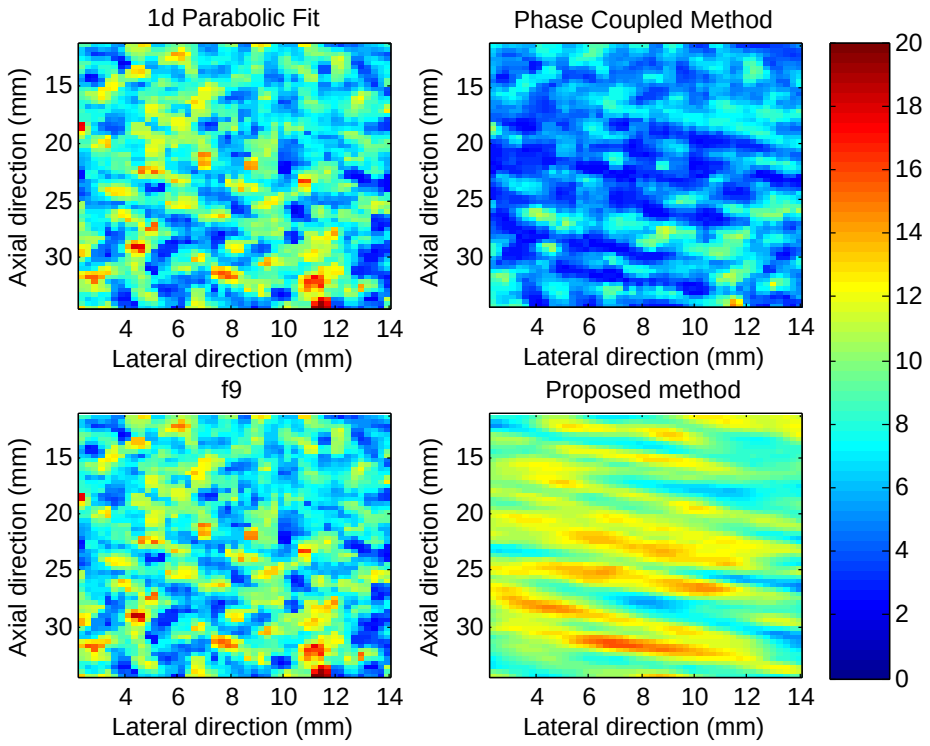

Figure 4.17: Estimated accumulated displacement fields of dataset left10 from different estimators. Note that the true motion is 10mm.

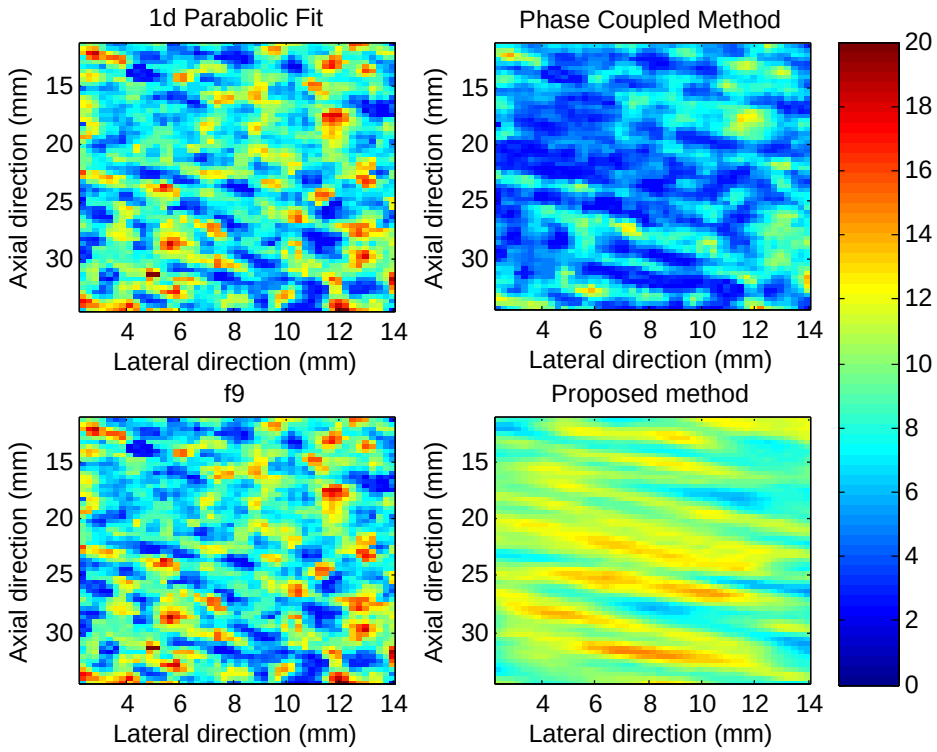

Figure 4.18: Estimated accumulated displacement fields of dataset right20 from different estimators. Note that the true motion is 10mm.

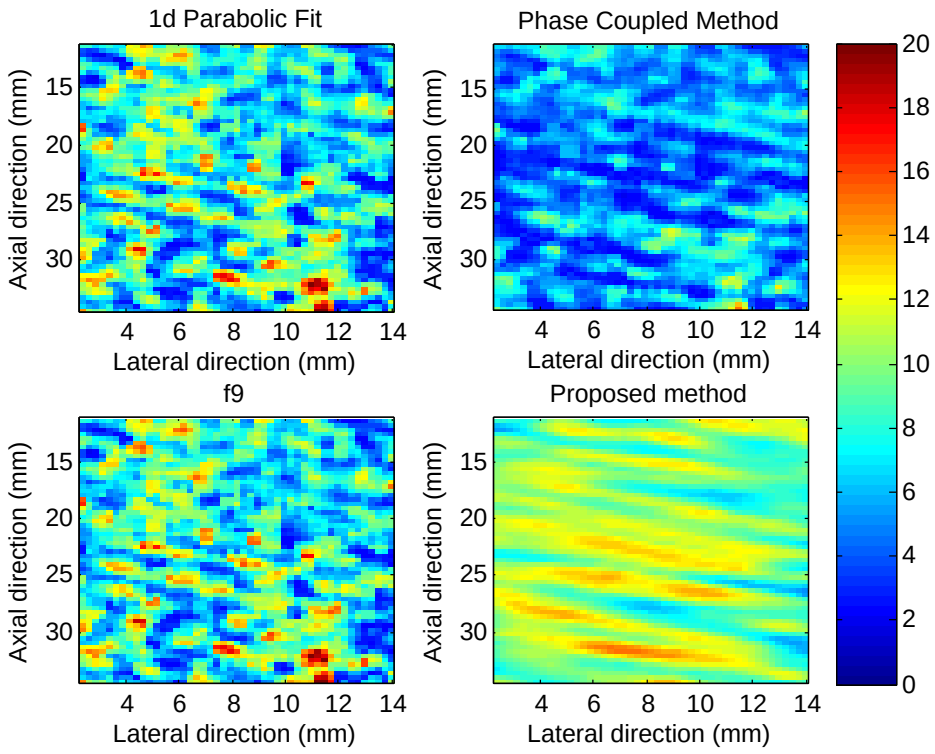

Figure 4.19: Estimated accumulated displacement fields of dataset left20 from different estimators. Note that the true motion is 10mm.

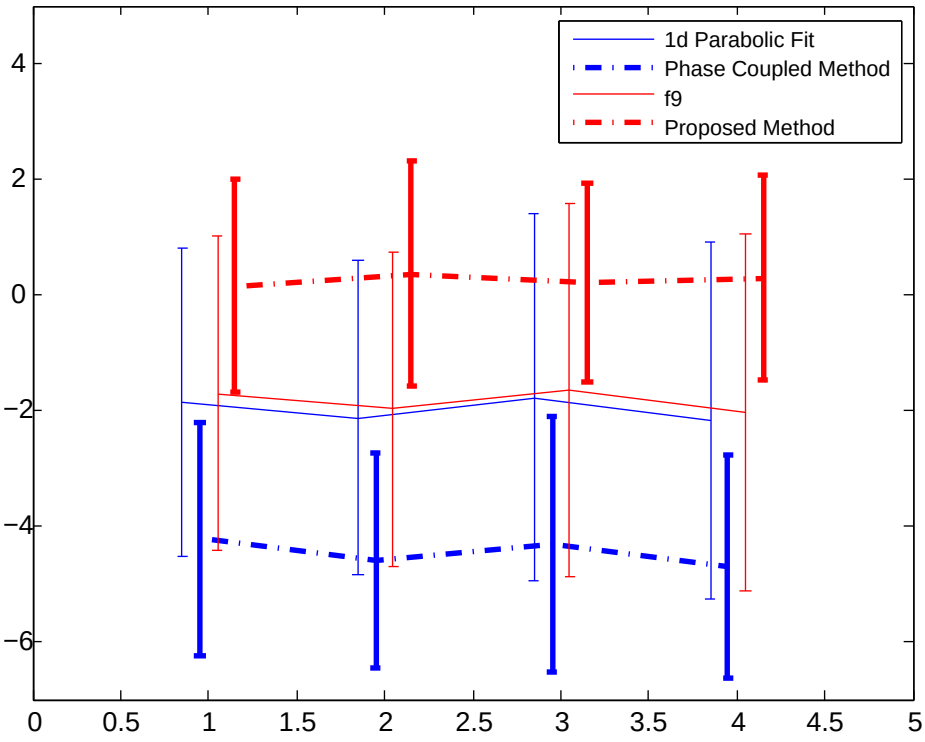

Figure 4.20: Mean and standard deviation from the accumulated displacement field. From left to right, results of right10, left10, right20 and left20 are shown.

phase coupled method which is used to indicate deformation of correlation function. Once the deformation is below certain threshold, a zero is returned. Then there is a certain amount of zero displacements since phase coupled method is more sensitive to shape of correlation function. It is clear that the estimated displacement is more concentrated from the proposed method than other three methods in both the axial (Figure 4.10) and lateral (Figure 4.11) directions.

Figure 4.12 shows one example of accumulated displacements in the axial direction (top) and the lateral direction (bottom) from one sample in right10. Stable motion can be observed in the axial direction from every method and difference between each method is small. However, constant speed motion can be barely seen except from the proposed method. Even though the array is kept static after 11 sec, other three methods are still showing relative motion between array and phantom. Figure 4.13 shows one representative accumulated displacements of left10. In Figure 4.5, all subsample estimators except the zero phase crossing method has an opposite bias when estimating positive and negative displacements. We can clear see the same trend from accumulated lateral displacements in Figure 4.12 and Figure 4.13. For the case of accumulated axial displacements, the difference is relatively much small, which can be due to fine resolution in the axial direction. Figure 4.14 and Figure 4.15 show another pair of accumulated displacement from right20 and left20.

In Figure 4.17 and Figure 4.19, estimated accumulated displacements from left10 and left20 are shown respectively. The total displacement is calculated by square root of sum squared accumulated axial displacement and accumulated lateral displacement. The ground truth of accumulated displacement field is a 10 mm map controlled by a pre-programmed motor. Similar trend can be seen from both displacement fields that estimated motion by the proposed method is more uniform and other three methods produce high noisy estimation. Scattering environment also plays an important role as the accumulated displacement fields from parabolic fit, phase coupled method and f9 have a similar map and results by zero phase crossing method from left10 and left20 are also similar. Figure 4.16 and Figure 4.18 show cases of right10 and right20.

Figure 4.20 shows mean and standard deviation of the accumulated displacement fields. Results of four data sets right10, left10, right20 and left20 are shown from left to right. Curving fitting methods and f9 produces consistent negative bias with four data

sets. Statistics are shown in Table 4.2. The proposed method exhibits smaller standard deviation with right20 and left20 than right10 and left10 while other three estimators do the opposite. It can be explained by the fact that bias and standard deviation from the proposed method is less than that from other three methods when estimating smaller motion. This results validates what can be seen in Figure 4.7, which shows that when estimating small displacement (less than 0.1 sample), the zero phase crossing method has the smallest standard deviation and other three methods have a similar magnitude.

4.6 Conclusions

A two-dimensional subsample estimator based on zero phase crossing in ultrasound has been presented in this chapter. Mathematical proof of this method is shown and simulation is performed to compare the performance of this method with two common curve fitting techniques and one polynomial surface fitting technique. The simulation results show that it is the most reliable algorithm in terms of bias, standard deviation.

The feasibility of using this method in 2D displacement estimation with sub-sample accuracy is also validated using experimental data. Uniform motion with a known sub-sample move provides a tool to characterize performance of different estimators. Future work would be application of this method to strain estimation in the non-uniform motion.

Chapter 5

Characterization of Vessel Wall Dynamic Using Ultrasound

5.1 Introduction

We have demonstrated the use of a 2D speckle tracking algorithm to estimate axial and lateral tissue displacements with subsample accuracy [58]. Furthermore, at moderately high frame rates, it was shown to be capable of simultaneously tracking tissue motion and blood flow in the carotid artery of human volunteers [99]. This capability will allow for new noninvasive hemodynamic characterization of blood vessels. In bio-fluid mechanics studies, measuring the details of the flow in arterial models or artificial organs is essential to investigate various flow-induced changes and to evaluate parameters, such as wall elasticity , steady and pulsatile flow. In addition, robust measurement of flow and tissue motion, together with appropriate forward computational fluid dynamics model, can be used for solving inverse problems to reconstruct the mechanical properties of target vessel walls, a grand challenge problem.

Characterization of performance of different 2D estimators with subsample accuracy is of great importance as displacement between frames is under sample due to higher frame rates. A series of simulations based on MATLAB were studied to explore comparison of performance of different subsample estimators in Chapter 4. Many time-domain algorithms have been suggested and used in ultrasound echo signals., including recently proposed method in [58], extended methods from 1D problem and polynomial function

fitting technique in [32]. All of these methods are based on pattern matching function. 1D subsample estimator and polynomial function fitting can be found in [32] and phase-coupled method was proposed in [58].

In this chapter, our recently proposed 2D estimators in the previous chapter is compared with other conventional estimators using simulated RF data. Two common flow profiles, i.e., parabolic flow and cosine flow, were simulated in FieldII simulation package. The 2D zero phase crossing algorithm is compared to other subsample estimators, given the true displacement field. Besides, we present experimental validation of our ability to track flow and wall motion in a tissue mimicking flow phantom (ATS Model 524).

5.2 Materials and Method

5.2.1 Simulation

To simulate ultrasonic echo data, the FieldII [60] acoustical simulation program was used to generate pre- and post-shift RF frames. Parameters of the simulation are as follows: a 196-element linear array transducer with 64 channels both in transmitter and receiver; the center frequency was 5 MHz and the sampling frequency was 40 MHz. The transmit beam was focused at the depth of 60 mm and dynamic receive focusing was used. The speed of sound in tissue was assumed to be equal to 1540 m/s. The point spread function of the linear array and the simulated B-mode image are displayed in Figure 5.1.

Two flow patterns, parabolic and raised-cosine, were simulated in Field II. The sampling frequency for parabolic flow simulation was chosen as 30 MHz. All scatters were positioned randomly and had Gaussian distributed amplitudes. The amplitudes of scatters in flow region was scaled by 20 dB below the tissue scatters. The center of the vessel was placed at a depth of 60 mm and radius of the vessel was set to 10 mm. The parabolic and raised-cosine flow profiles were symmetric with respect to the center of the vessel. Several frames were collected for each flow profile. The different 2D subsample estimators were used to calculate the displacement field. A minimal 3×3 median filter was applied to remove spurious vectors and therefore improves smoothness of estimated displacement field. Figure 5.2 depicts the displacement vector of a cosine

flow profile generated by the 2D zero phase crossing algorithm.

5.2.2 2D phase-coupled speckle tracking algorithm

The theoretical underpinning of this algorithm is that the gradient vectors of the magnitude of the 2D cross correlation approach the true peak along the orthogonal to the zero-phase contour. This was established theoretically for a 2D shift, $s(x, z, t_1) = s(x - d_x, z - d_z, t_0)$, by establishing a relationship between the phase and magnitude gradients of the 2D complex correlation from the echo data at t_0 and t_1 [58]. Using a sampled-data grid of the 2D cross correlation in the vicinity of the true peak, it is possible to project the magnitude gradient vectors on the zero-phase contour. Of course, this assumes that the grid is sampled finely enough to make a valid projection. The phase-coupled algorithm interpolates the 2D cross correlation in the lateral direction by the smallest possible factor to make a valid projection. This was shown to allow for submicron lateral displacement accuracy with relatively low lateral interpolation factors (typically <16) .

Figure 5.3 illustrates this approach using actual pulse-echo data from a diagnostic scanner. This approach achieves subsample smooth and accurate lateral displacement estimates with minimum interpolation in the lateral direction.

The steps of the phase-coupled algorithm are listed as follows (See Figure 5.3):

Step0 The 2D complex cross correlation function is calculated by two kernel windows from two frames after taking Hilbert transformation in the axial direction.

Step1 A fast search algorithm can be used to find the integer shift based on the coarse grid (computed at the original axial and lateral sampling frequencies).

Step2 A 3×3 grid centered on the coarse peak of the cross correlation is defined.

Step3 While $1 \leq j \leq j_{max}$ the grid is interpolated laterally by a factor of 2^j. For each interpolation factor, the gradient vectors of the magnitude are computed. The two gradient vectors with closest to being orthogonal to the zero-phase line are chosen and their intersection point is found. If angle between the two vectors is greater than θ_{max}, $j \leftarrow j + 1$ Repeat *Step3*. Otherwise, *Continue*

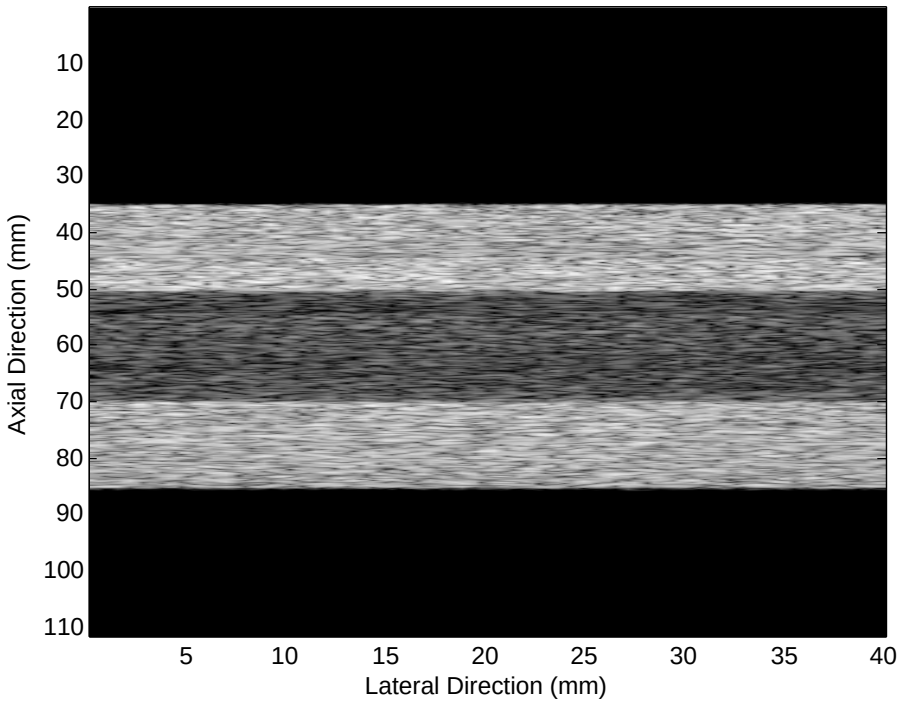

Figure 5.1: Bmode of the flow phantom simulated in FieldII.

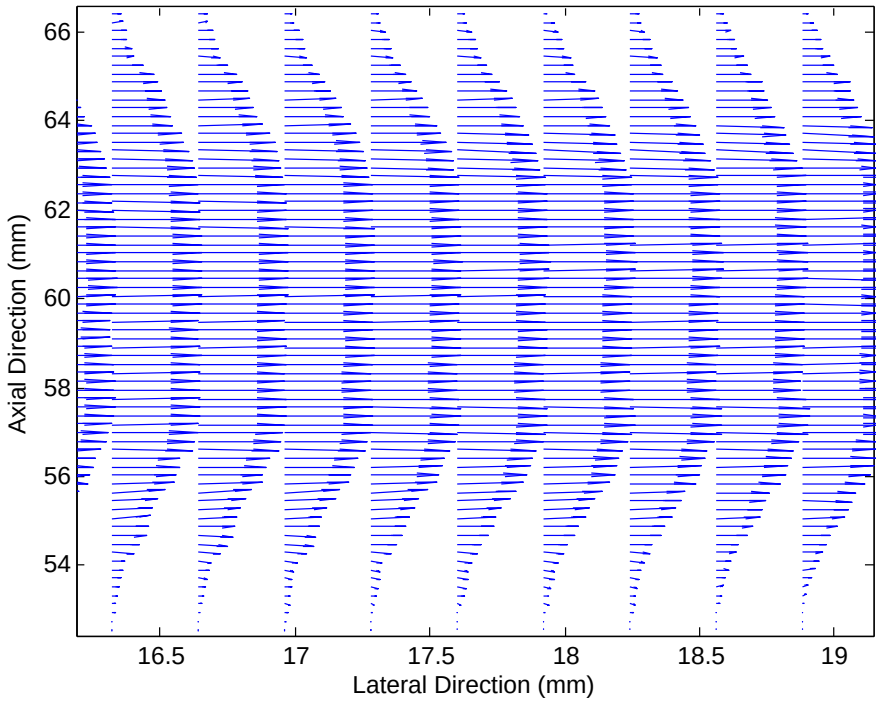

Figure 5.2: Displacement vectors in the flow region of a raised-cosine profile.

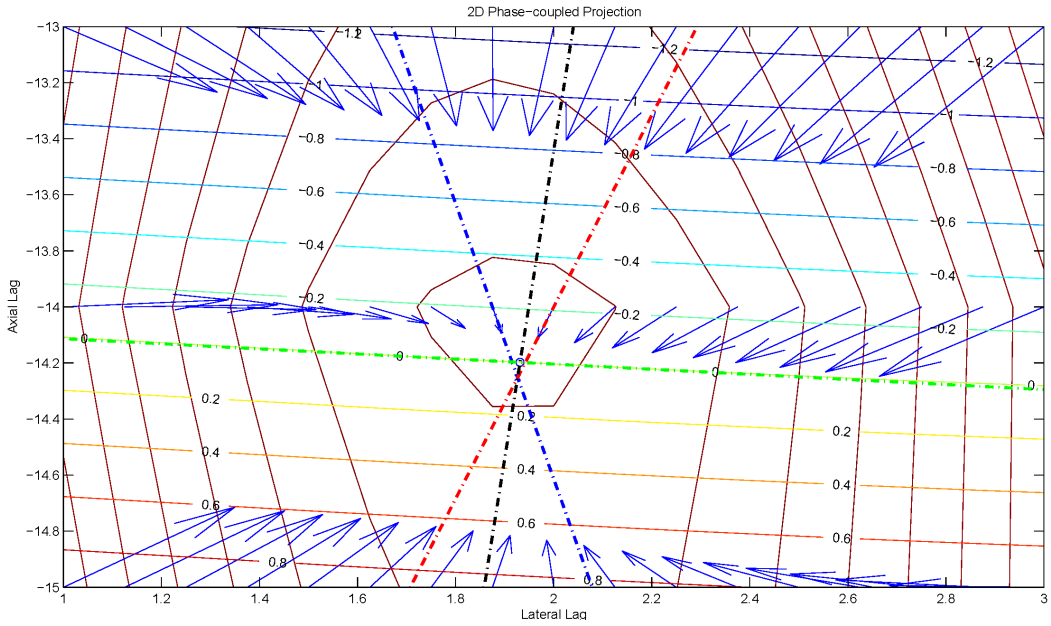

Figure 5.3: Magnitude and phase contours of the 2-D cross correlation on the laterally-interpolated 3×3 grid in the vicinity of the correlation peak (between lags 13 and 15 axially and 1 and 3 laterally). The arrows represent the magnitude gradient vectors on the interpolated grid. Lateral interpolation by a factor of 16 is used in this case (with the interpolated grid points indicated by the arrow bases). The phase contours are labeled with phase values in radians and appear to be almost straight with a small tilt. The true peak is indicated by the open circle on the zero-phase line. The dash-dotted lines are the directions of the magnitude gradient vectors closest to the peak and the tangent and the orthogonal to the zero-phase line.

Step4 An orthogonal projection from the intersection point on the zero-phase line is made.

Step5 The coordinates of the intersection point define the estimate of the shift, $(\hat{d}_x, \hat{d}_z)$. *Stop.*

Step3 provides the advantage of estimating the minimum necessary lateral interpolation to obtain an accurate subsample estimate. This is a computational advantage in addition to minimizing errors resulting from higher interpolation factors. However, the conditional nature of this step reduces the computational advantage when high performance computing is considered for implementation.

5.2.3 Experimental setup

A commercial ultrasound scanner (Sonix RP, Ultrasonix, BC, Canada) was used to collect the beamformed RF data synchronized with pressure and flow sensor measurements. A custom designed program in ultrasound scanner make it possible to collect a moderately high frame rate of 448 Hz [99]. The ATS model 524 flow phantom was connected with a Cole-Parmer MasterFlex roller pump which provided the pulsatile flow. Two pressure sensors were attached to this flow phantom at the beginning and the end while one flow sensor was placed in the middle of flow loop.

Cellulose microspheres were diluted in water to produce linear scattering from the flow during data collection. This flow phantom was imaged with a linear array probe (LA14-5/38). The arduino microcontroller board was utilized to synchronize the data collection of sensors and RF frames from the linear array. The sensor data was stored in terminal connecting arduino and MATLAB. The displacement field was then computed offline from RF data by the 2D zero phase crossing tracking algorithm and other subsample estimators. Figure 5.4 shows the experimental setup (left) and Bmode of the flow phantom (right).

5.2.4 *In Vivo* Experiment

The LA14-5/38 probe on the SonixRP was used to collect RF data from imaging the right carotid artery in a healthy 26-year old volunteer. The images were collected at a

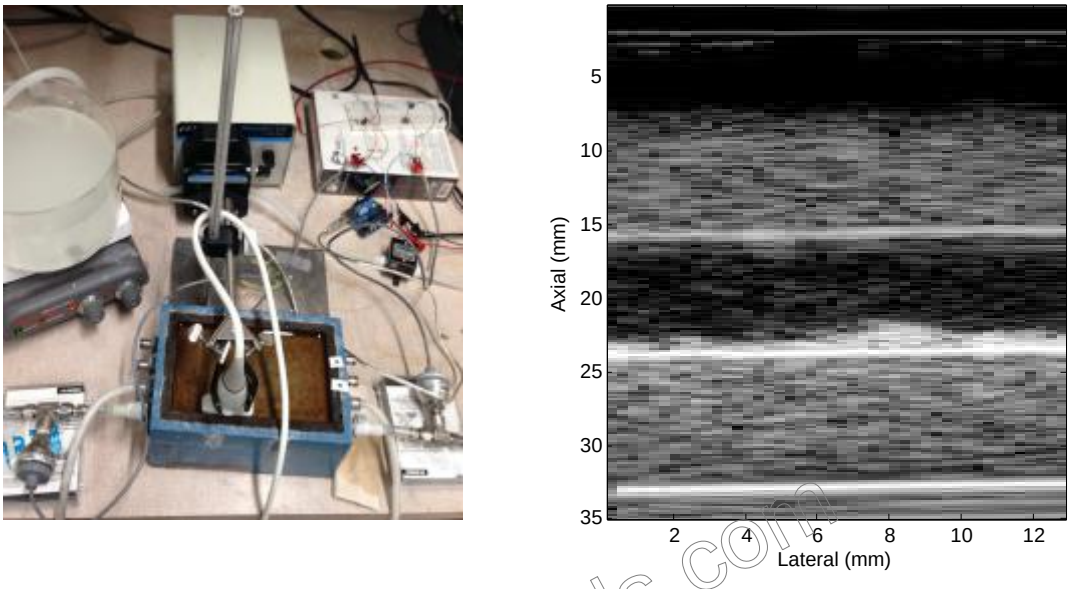

Figure 5.4: Experimental setup (left) and Bmode with dynamic of 50 dB of the flow phantom (right).

frame rate of 325 at the expense of limiting the field of view in the lateral dimension (approximately 15 mm or 51 A-lines per frame) [99].

5.3 Results and Discussion

5.3.1 Simulation results

Two representative displacement fields, i.e., the raised-cosine flow and parabolic flow, are shown in Figure 5.5. Scatters in simulation is only moving in the lateral direction at a speed as a function of depth. A kernel size of 45 samples (0.855 mm) in the axial direction by 5 samples (1.45 mm) in the lateral direction is chosen to calculate the displacement field. Displacement fields from parabolic fit, f9 and PC have a similar discontinuity pattern in the flow region, which can be due to that all of them are based on magnitude of cross correlation function. The well-behaved nature of the displacement fields is demonstrated both in the raised-cosine and parabolic flows. Once find the integer shift, the zero phase crossing method only uses the linearity of phase of cross correlation function and then is not prone to any magnitude distortion. As also demonstrated in Figure 5.5, the displacement estimation in the non-stationary region is all consistent with the ground truth in simulation. In the case of raised-cosine flow, smooth continuity of estimated displacement field by zero phase crossing method is clear shown over other three estimators. Note that intersection method shown in bottom right figure is the same algorithm used in Chapter 4.

Figure 5.6 shows the average flow from different estimators as a function of depth from simulated RF frames. The red line is the ground truth pre-defined in FieldII. The average flow is calculated by taking statistical mean along the lateral direction, i.e., taking mean of all estimation at the same depth. Average raised-cosine flow estimation matches the ground truth in good manners, except that there is certain fluctuation in the steady flow region. For the parabolic flow, high deviation is observed in the boundary between flow region and stationary region. The hypothesis can be made that the raised-cosine function is derivatively continuous at the boundary while the parabolic function is not. One can imagine that estimators low-pass filter the pre-defined flow function. The gap between estimation and ground truth becomes smaller as a smaller kernel axial size is used. For example, 5.7 uses 15 samples in the axial direction. It is

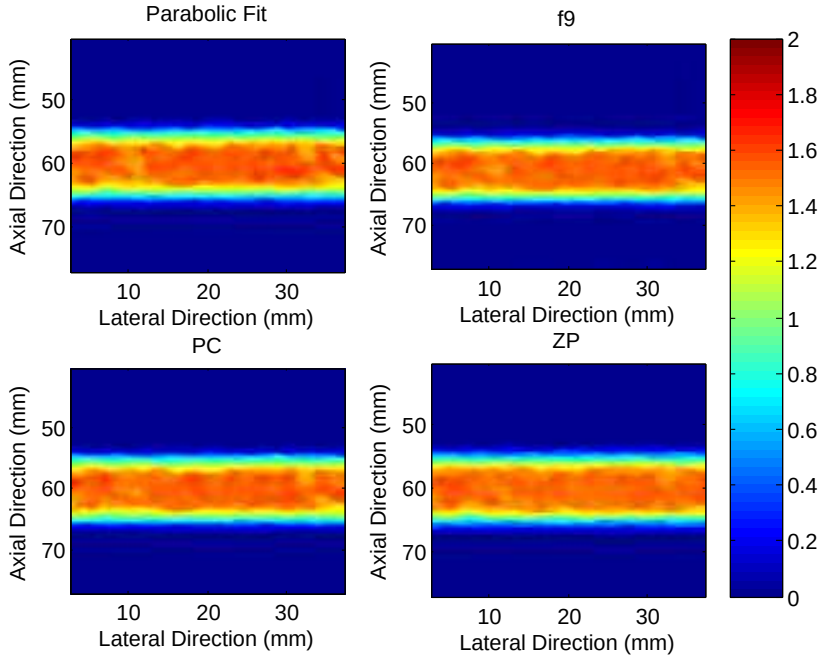

(a) The raised-cosine profile flow

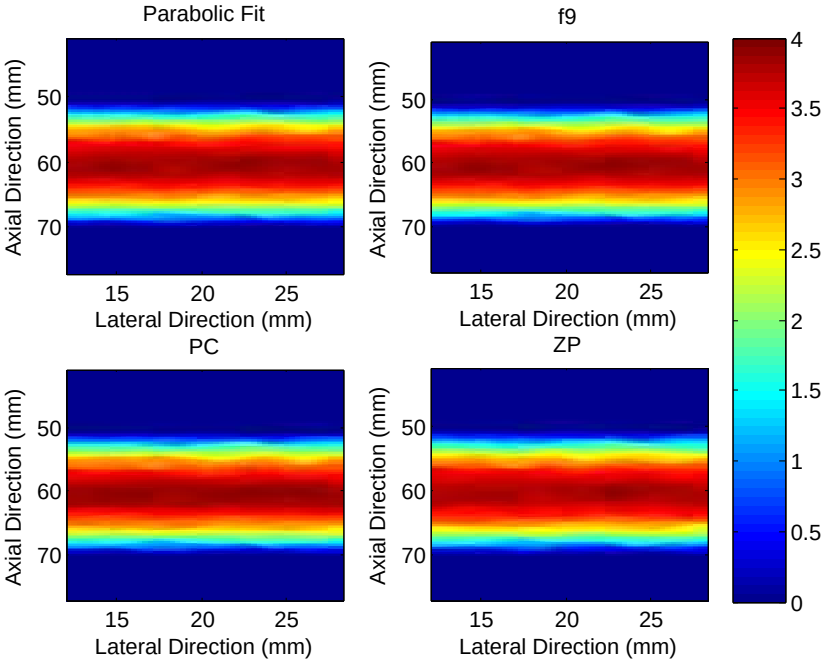

(b) The parabolic profile flow

Figure 5.5: Estimated displacement field simulated in MATLAB. The kernel size is 45 sample (0.855 mm) in the axial direction and 5 samples (1.45 mm) in the lateral direction.

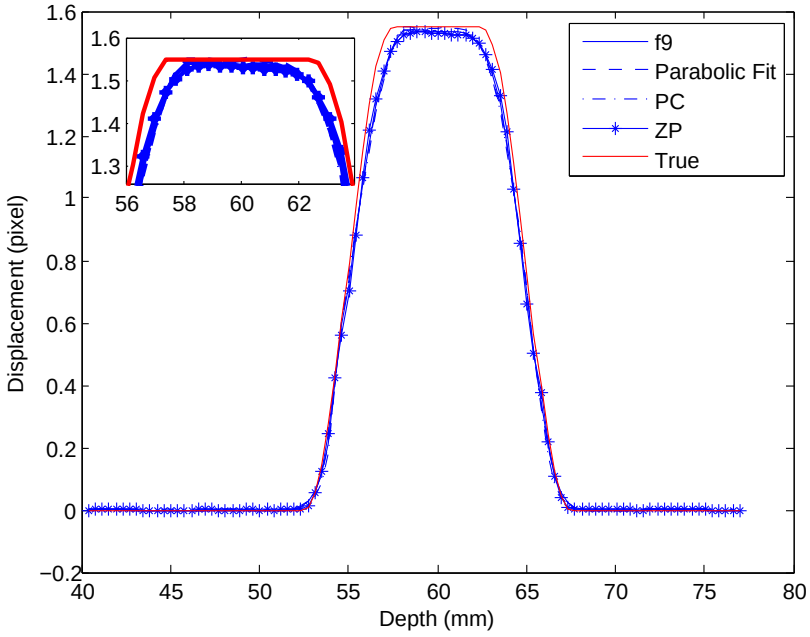

(a) The raised-cosine profile flow

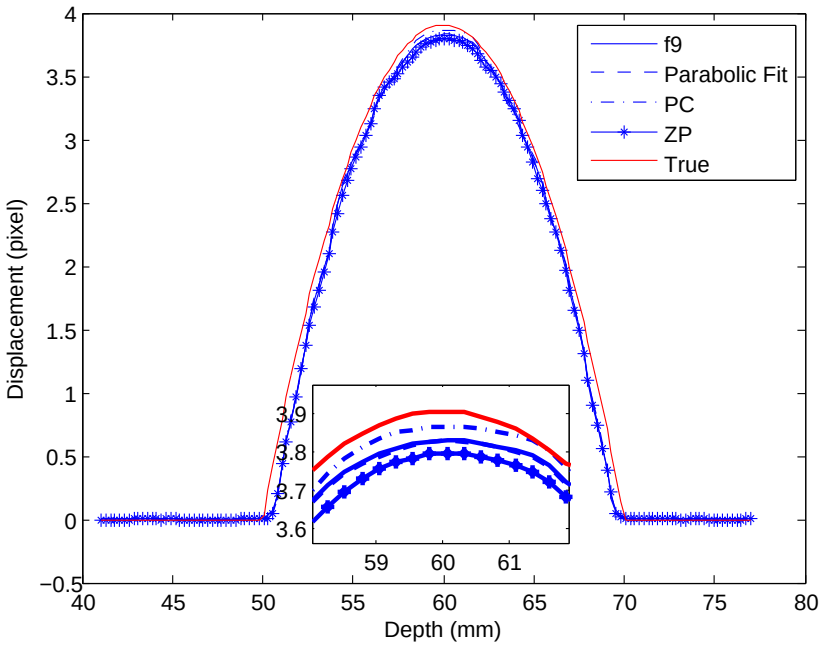

(b) The parabolic profile flow

Figure 5.6: Average flow estimation simulated in MATLAB. The red line is the ground truth and the kernel size is 45 sample (0.855 mm) in the axial direction and 5 samples (1.45 mm) in the lateral direction.

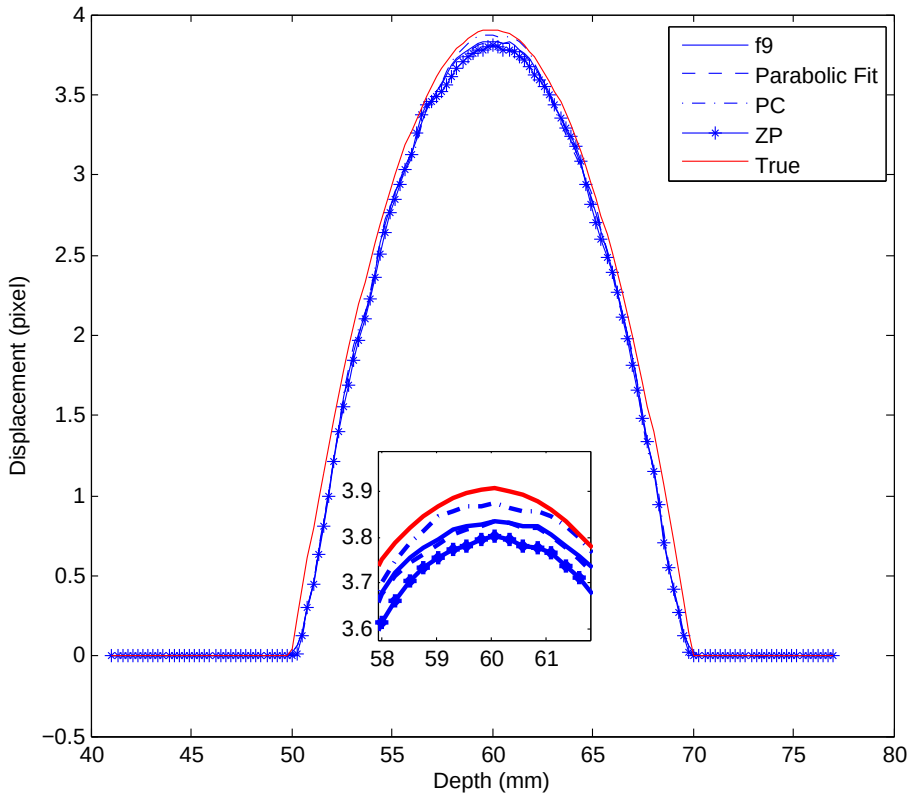

Figure 5.7: Average flow estimation of the parabolic flow simulated in MATLAB. The red line is the ground truth and the kernel size is 15 sample (0.285 mm) in the axial direction and 5 samples (1.45 mm) in the lateral direction.

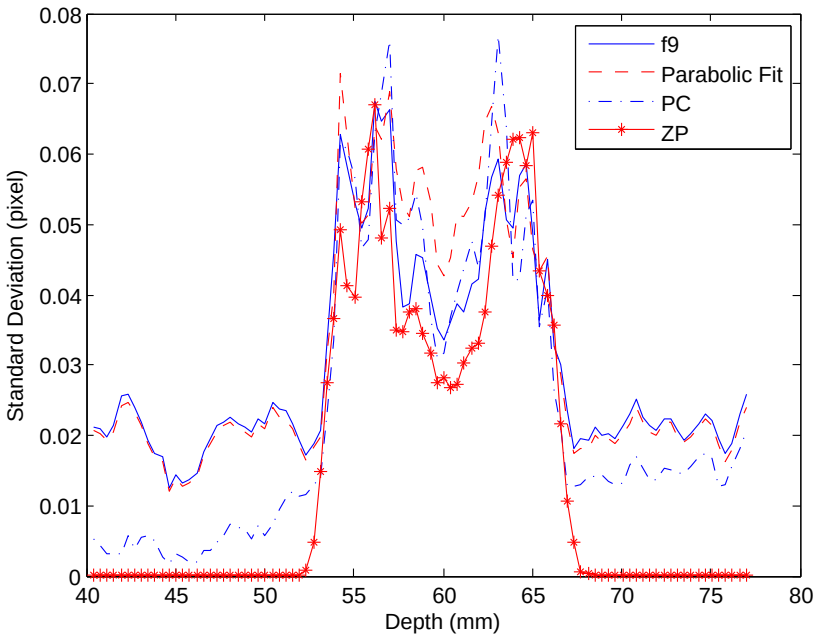

(a) The raise-cosine profile flow

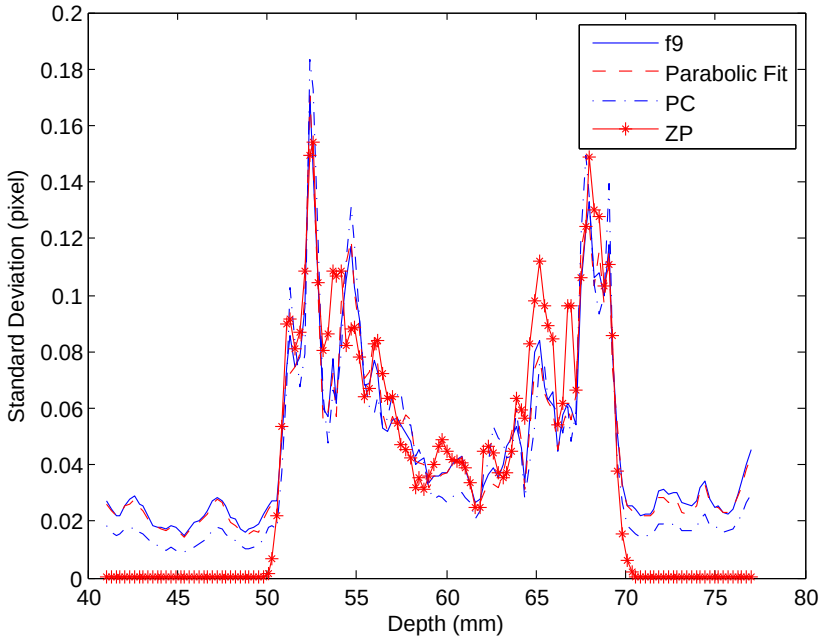

(b) The parabolic profile flow

Figure 5.8: Standard deviation of estimation of the raised-cosine flow simulated in MATLAB. The red line is the ground truth and the kernel size is 45 sample (0.855 mm) in the axial direction and 5 samples (1.45 mm) in the lateral direction.

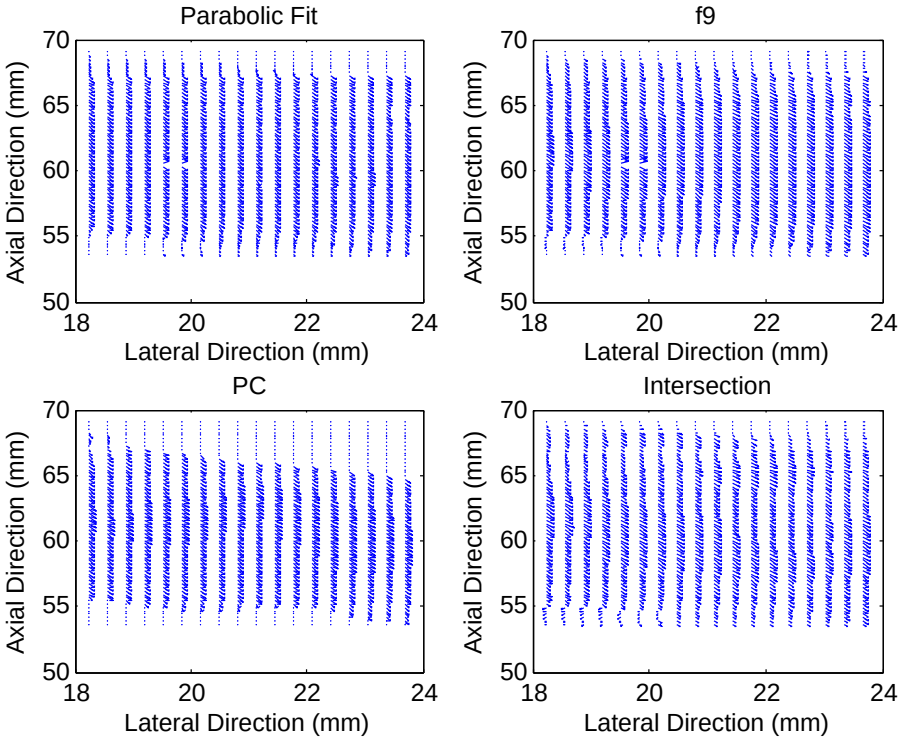

Figure 5.9: Displacement vectors in the flow region of a parabolic profile tilted by a 15 degree angle.

clear that the gap is smaller of 15 samples than that of kernel size in the axial direction of 45 samples shown in the bottom of Figure 5.6. However, it cannot be assumed that smaller kernel size gives a better estimation. Optimization of the window size is another important topic in displacement estimation needed to be taken into account for a good estimator [58]. A small window size is desirable if the cross correlation function is still well-behaved.

In Figure 5.9, where the standard deviation of flow estimation is shown with the raised-cosine flow on top and the parabolic flow on the bottom, the zero phase crossing method outperforms other estimators in the non-stationary region. In the flow region, it still has the smallest standard deviation for the raised-cosine flow estimation and is comparable to other estimators for the parabolic flow. It is expected that given a better cross correlation function, the estimation is more accurate, as clearly depicted in the difference between stationary and non-stationary regions. Among different estimators, the zero phase crossing method stands out as the top choice of a stable algorithm. An interesting finding about parabolic flow estimation is that the standard deviation is the worst around the boundary. It can be concluded that the continuous flow generally gives rise to a good cross correlation function and thus estimators have a smaller standard deviation.

Figure 5.9 shows the displacement field of a parabolic flow tilted by a 15 degree angle. In this case, both lateral and axial shifts have been estimated by all estimators. The zero phase crossing method captures the detailed displacement field. Whereas, phase-coupled method uses a certain threshold for magnitude of cross correlation function and simply sets zero displacements if the magnitude of cross correlation function is below that threshold. This is why we see a sudden change of flow between stationary and non-stationary regions.

5.3.2 Experimental results

Figure 5.10 shows the comparison of cumulative axial displacement on the wall with pressure sensor data (top) and lateral displacement inside the channel with the flow sensor data (bottom). Both flow sensor and lateral displacement data were filtered using a 5-point moving average filters. Dynamic behavior of sensor data and 2D phase-coupled speckle tracking algorithm agreed with the stimulus, i.e., roller pump. The

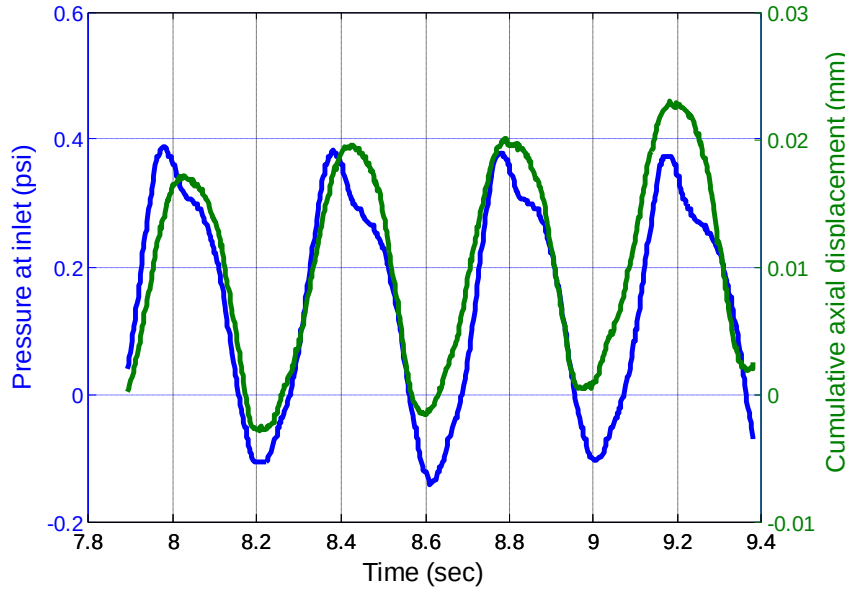

(a)

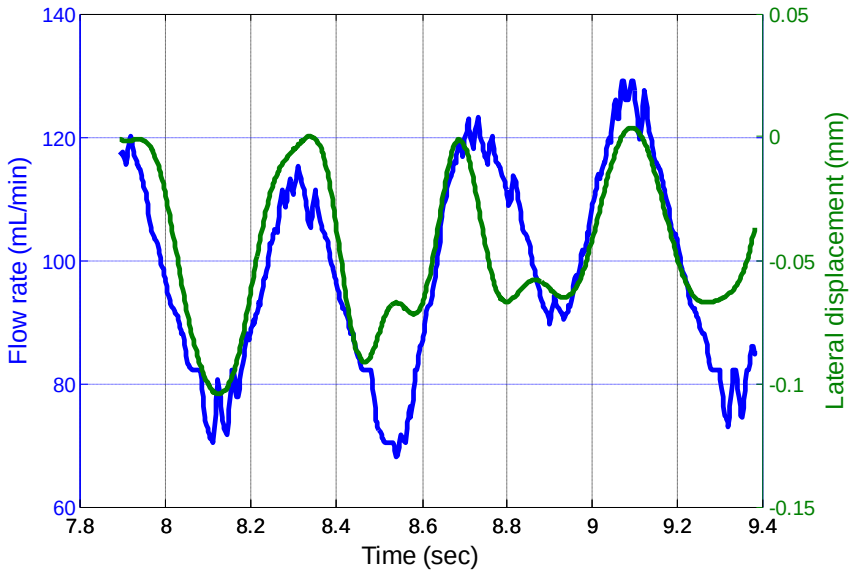

(b)

Figure 5.10: Cumulative axial displacement on the wall with pressure sensor data (a) and lateral displacement inside the channel with the flow sensor data (b).

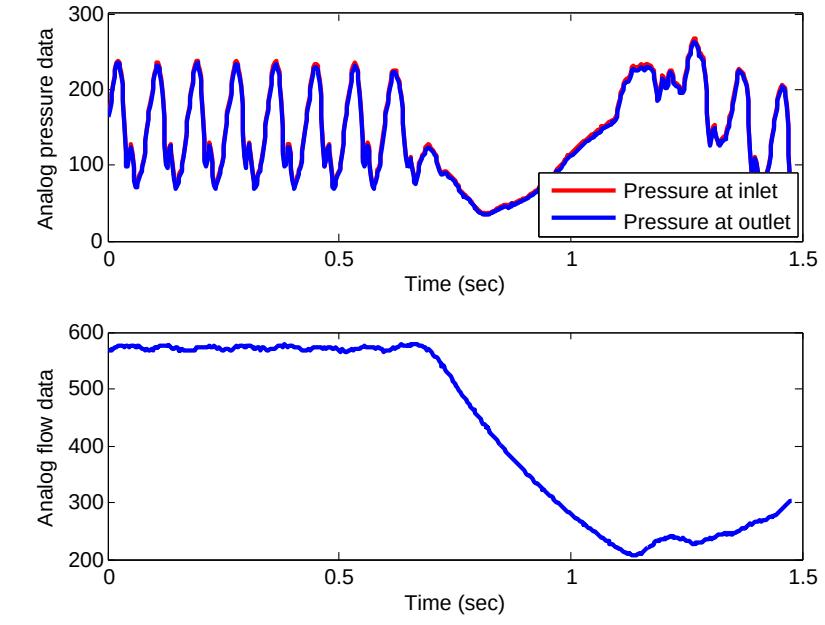

(a)

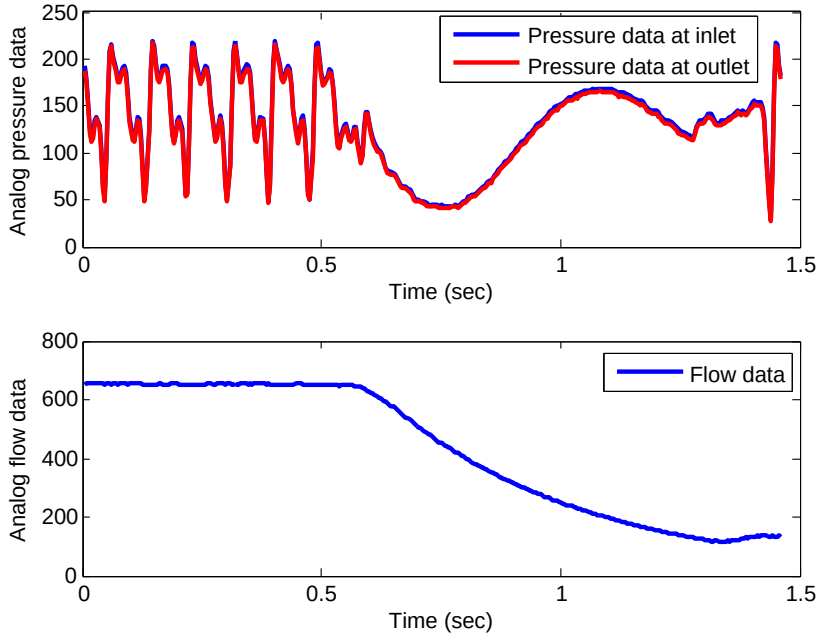

(b)

Figure 5.11: Analog pressure data and flow data collected from sensors with different frame rates. (a) is 413 frames/sec and (b) is 260 frames/sec.

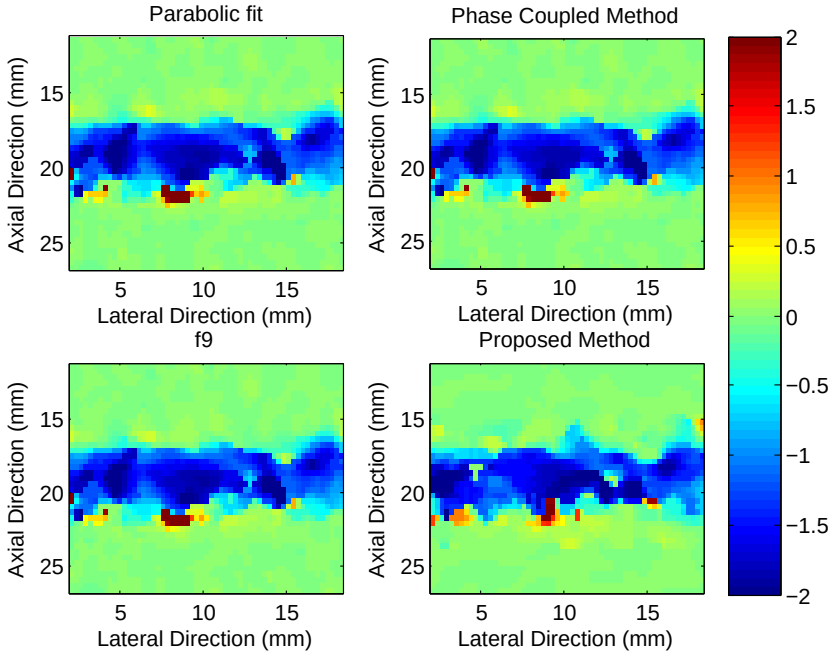

(a)

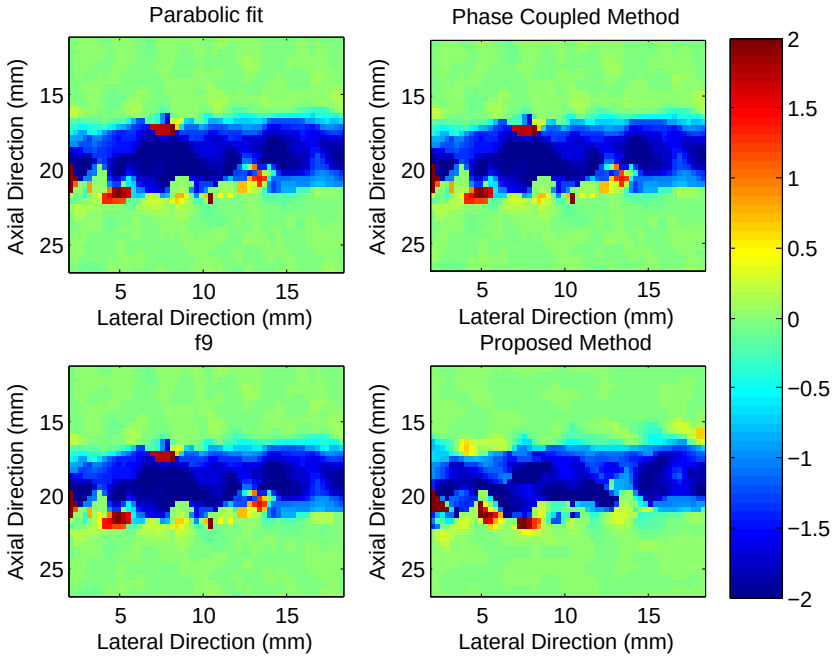

(b)

Figure 5.12: Two representative flow estimation by different estimators. (a) is the lateral displacement between frame 40 and frame 41. (b) is the lateral displacement between frame 105 and frame 106.

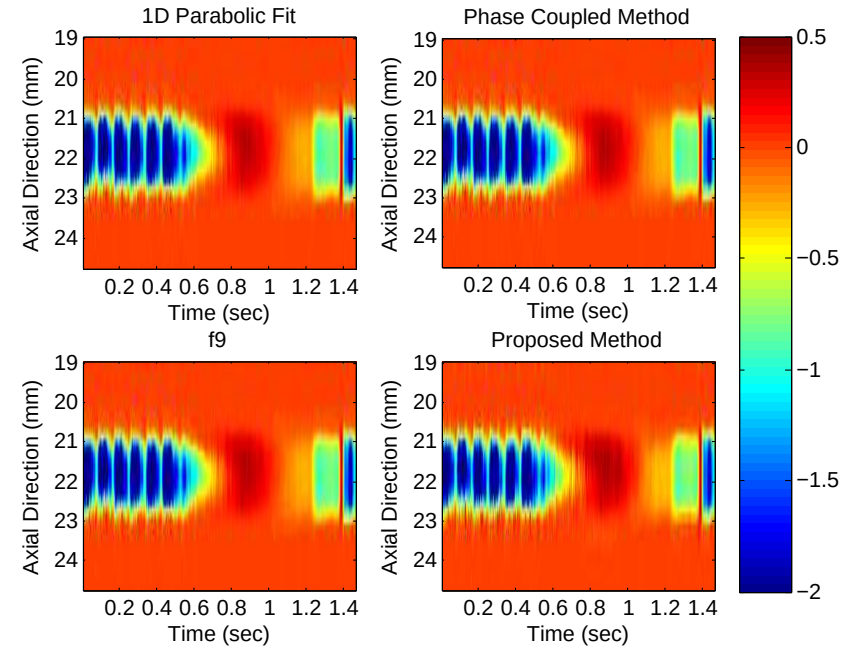

(a)

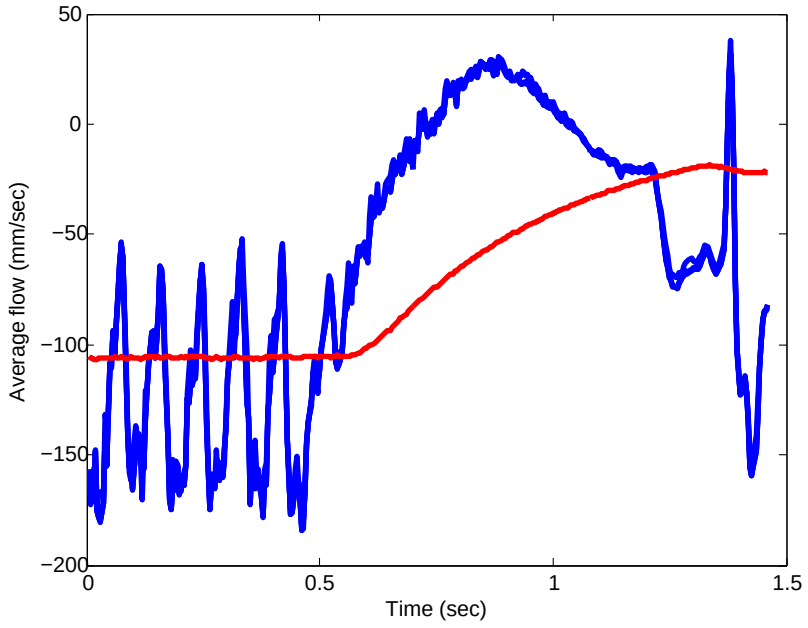

(b)

Figure 5.13: (a) is temporal averaged flow estimation for the dataset of 260 frames/sec. (b) is the volumetric flow velocity comparison between estimation (blue) and sensor (red).

results were repeatable and highly correlated in the case of pressure and wall motion data, indicating the validity of tracking the wall motion for the estimation of pressure. Lateral displacement speckle tracking data exhibited general agreement with flow sensor data, but some discrepancies exist. Despite these discrepancies, the general agreement between the two waveforms is clear. Therefore, the periodic nature of phantom movement is captured axially, and more importantly, laterally.

The sensor and RF frames were also collected when the roller pump was manually switched on and off. For example, Figure 5.11 shows the analog pressure data and flow data collected from sensors with different frame rates. Two pressure data was collected with one (red) at the inlet and the other one (blue) at the outlet. Initially, the steady state flow has been running for a certain period of time and then the switch is turned off. Instantly, the switch is turned on. As shown in Figure 5.11, the pressure recovers much faster than the flow due to the fact the flow is heavily low-pass filtered based on the documentation of the flow sensor. Figure 5.12 shows two examples of the lateral displacement by different estimators. The first one is the lateral displacement field between frame 40 and frame 41. Flow inside the phantom is clearly demonstrated, which is also shown in the second example of frame 105 and frame 106.

Figure 5.13 (a) represents the temporal average flow estimation. The periodicity of steady-state flow is clearly captured by displacement estimators. Besides, the transitionary change due to the on/off switch of roller pump is also shown in the temporal profile. This is closely consistent with the pressure data shown in Figure 5.11. Figure 5.13 (b) represents the volumetric flow velocity by estimators and sensors. Since the flow sensor is heavily low-pass filtered, the sensor data is not as responsive during on/off switch of roller pump as estimation results are.

5.3.3 *In Vivo* results

A longitudinal view of the carotid artery was also collected by the same imaging system and the linear array at a frame rate of 325 [99], Bmode of which is shown in 2.14. Figure 5.14 depicts the dynamic pulsation of anterior wall (top) and posterior wall (bottom). All estimators are able to capture the subsample motion since all methods are continuous subsample estimators. Another observation that the phase-coupled algorithms remain more stable than other estimators because of its smaller estimation bias is consistent

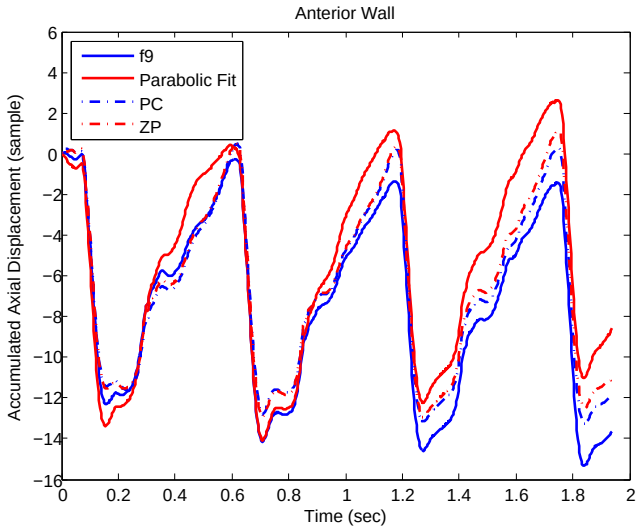

(a)

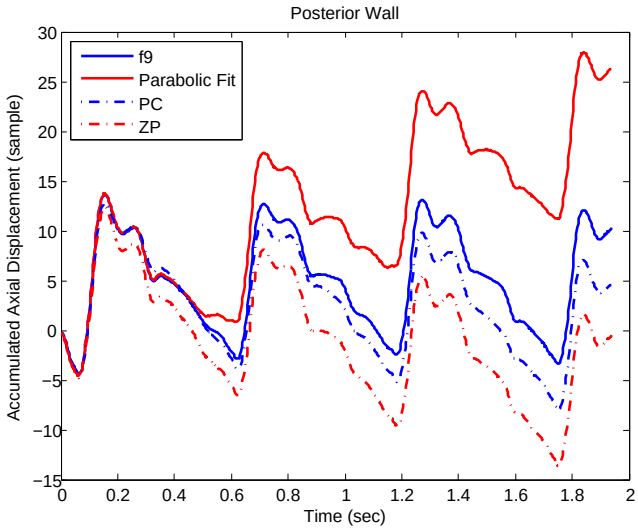

(b)

Figure 5.14: (a) is an example of accumulated axial displacement (samples) on anterior wall. (b) is an example of accumulated axial displacement (samples) on posterior wall.

with results of Fig. 5.6.

5.4 Conclusion

Characterization of performance of different 2D subsample estimators was shown. Phase-coupled and the zero phase crossing methods outperform other common techniques in terms of bias and standard deviation. Certain improvement of phase-coupled method can be made, for example, adaptive window size and hybrid methods, based on performance of estimators in different regions. This research also lay foundation for further investigation into estimation of speckle motion under various imaging conditions.

We have presented experimental measurements from a tissue-mimicking flow phantom using pressure and flow sensor data synchronized with wall motion and lateral displacement estimates based on a 2D phase-coupled speckle tracking technique. The results show that the speckle tracking method for simultaneous estimation of vessel diameter and flow produces estimates that are largely in agreement with the sensor data. The vessel wall diameter can be reliably and repeatedly measured using 2D speckle tracking. Lateral displacements are in general agreement with the measured flow profile using the flow sensor. These results provide validation for our in vivo results shown in [99]. Furthermore, they set the ground work for quantitative assessment of vascular disease based on noninvasive image-based measurements.

Chapter 6

Conclusions and Future Work

6.1 Conclusions

We proposed the use of zero phase crossing method for displacement estimation in medical ultrasound. In Chapter 2, 3 and 4, algorithms are developed for the motion estimation in the axial direction (1D), the lateral direction (1D), in both the axial and lateral directions (2D), respectively. The performance of different subsample estimators is investigated under various conditions using both simulation and experimental ultrasound data frames.

Chapter 2 derives the zero phase crossing method using a 1D mathematical model of ultrasound pulse echo signals. The proposed method is compared to other commonly used subsample estimators, including parabolic fit, cosine fit, spline-based interpolation. Performance criterion based on statistical mean and standard deviation shows that the proposed method is superior to the others. A deformation factor is also incorporated into the model and the proposed method outperforms all the other in this case as well.

In Chapter 3, the same idea from the axial direction is applied to the lateral direction in ultrasound imaging. The fact that the displacement in the lateral direction is different from that in the axial direction results from two things. One is that the lateral direction has a much coarser resolution, which is limited by the spacing between the A-lines. The other is that there is no carrier frequency in the lateral direction. A baseband RF signal model is chosen based on these facts. It is derived that whereas the complex normalized cross correlation (NCC) function may not have a linear phase, the maximum magnitude

of NCC still lies on the zero phase line. A series of simulation is implemented based on that model. Performance metric, mean and standard deviation, is demonstrated to differentiate various subsample estimators, including zero phase crossing method, parabolic fitting and cosine fitting methods. The simulation results in MATLAB show that the performance of zero phase crossing outperforms over other estimators in the whole range of subsample displacements. Simulation results in FieldII of a phantom with a non-uniform motion in the lateral direction also present consistent performance as shown in previous simulation results.

Based on the formulation of 1D cases in the axial direction and in the lateral direction, a 2D displacement estimator is derived. Essentially, a 2D RF signal model with a carrier frequency in the axial direction but no carrier frequency in the lateral direction is used to demonstrate derivations of the 2D displacement estimator. A known 2D displacement grid is generated in simulation to test different subsample estimators. The simulation results show that the proposed method outperforms other commonly used independent 1D algorithms and joint 2D surface polynomial fitting. Moreover, A sequence of ultrasound images is collected from a fabricated uniform phantom controlled by pre-programmed motor with known subsample displacement. A wire is put inside the phantom for the purpose of a reference displacement. Four different data sets are collected and subsample estimators are implemented and their results are compared to the known displacement. The experimental result shows that different estimators performs similarly in the axial direction but a distinct difference is observed in the lateral direction.

Furthermore, a flow phantom is simulated in FieldII with two flow profiles, i.e., parabolic flow and cosine flow. Different subsample estimators including the phase coupled method are then used to track flow motion. An experiment is set up with two pressure sensors and one flow sensor. Data collection from sensors is synchronized with the aid of a signal generator. The flow sensor uses a low pass filter before output so that dynamic of flow is suppressed. Surprisingly, the dynamic flow motion is captured by subsample estimators. Moreover, the periodicity of flow due to the roller pump is also captured by subsample estimators and compared to the flow sensor. The LA14-5/38 probe on the SonixRP was used to collect RF data from imaging the right carotid artery in a healthy 26-year old volunteer. The images were collected at a frame rate of 325

at the expense of limiting the field of view in the lateral dimension (approximately 15 mm or 51 A-lines per frame) [99]. Four different subsample estimators were then run to calcuate the accumulated temporal axial movement of the anterior and posterior walls. The phase-coupled speckle tracking method shows superior performance over others.

6.2 Future Work

6.2.1 Figure(s) of Merit

The accuracy of subsample estimators relies on the cross correlation function. For the 2D zero phase crossing method, linearity of zero phase lines around peak plays an important role. For the polynomial fitting method, the shape of cross correlation function matters. For the phase-coupled method, both the magnitude and phase of the cross correlation function are of significance. In addition, under different applications, scattering density and specular effect could give rise to various cross correlation function and even worse fail certain subsample estimators. A Figure of Merit, a characteristic of the cross correlation function [5], is a guide as to which subsample estimator gives a better estimation for a specific application, how gracefully a subsample estimator fails, etc. It still remained unsolved and opens numerous important research topics.

6.2.2 Three dimensional motion tracking

In the application of tissue motion, especially when there is substantial motion in the elevation direction (out of the plane of the axial and lateral directions), three dimensional displacement estimator plays an important role. The idea of zero phase crossing technique can be applied to 3D subsample estimation in a straightforward manner. Once we find three zero phase lines, two of them can determine a plane and the intersection point of the plane and another zero phase line gives the subsample estimation. The 3D zero phase crossing method can be compared to other 3D subsample estimators with access to 3D frame acquisitions.

6.2.3 Real-time implementation

As shown in Chapter 4, computation of two zero phase lines is in parallel, which makes real-time implementation of zero phase crossing method possible by using GPU. Our lab has already implemented real-time one dimensional zero phase crossing method for thermal applications. GPU's parallel computing capability could be utilized to calculate two zero phase line simultaneously. Then a standard form of first order linear equation needs to be solved, which is trivial and can be done in a closed form. Potential interpolation can be made around the maximum peak of the cross correlation function without much computational overhead.

Bibliography

[1] W. F. Walker and G. E. Trahey. A fundamental limit on the performance of correlation based phase correction and flow estimation techniques. *IEEE Trans. Ultrason., Ferroelect., Freq. Contr.*, 42:301–308, 1995.

[2] W. F. Walker and G. E. Trahey. A fundamental limit on delay estimation using partially correlated speckle signals. *IEEE Trans. Ultrason., Ferroelect., Freq. Contr.*, 42:301–308, 1995.

[3] C. de Korte, A. van der Steen, E. Cspedes, G. Pasterkamp, S. Carlier, F. Mastik, A. Schoneveld, P. Serruys, and N. Bom. Characterisation of plaque components and vulnerability with intravascular ultrasound elastography. *Physics in Medicine and Biology*, 45:1465–1475, 2000.

[4] E. Turgay, S. Salcudean, and R. Rohling. Identifying mechanical properties of tissue by ultrasound. *Ultrasound in Medicine and Biology*, 32:221–235, 2006.

[5] J. Ophir, I. Cèspedes, H. Ponnekanti, Y. Yazdi, and X. Li. Elastography: A quantitative method for imaging the elasticity of biological tissues. *Ultrason. Imag.*, 13:111–134, 1991.

[6] J. Ophir, S. Alam, B. Garra, F. Kallel, E. Konofagou, T. Krouskop, C. Merritt, R. Righetti, R. Souchon, S. Srinivasan, and T. Varghese. Elastrography: Imaging the elastic properties of soft tissues with ultrasound. *Medical Ultrasound*, 29:155–171, 2002.

[7] I. Cespedes, J. Ophir, H. Ponnekanti, and N. F. Maklad. Elastography: a quantitative method for imaging the elasticity of biological tissues. *Ultrasonic Imaging*, 13:111–134, 1993.

[8] J. Ophir, S. Alam, B. Garra, F. Kallel, E. Konofagou, T. Krouskop, and T. Varghese. Elastography: ultrasonic estimation and imaging of the elastic properties of tissues. *Ultrasonic Imaging*, 213:203–233, 1999.

[9] A. Pesavento, C. Perrey, M. Krueger, and H. Ermert. A time-efficient and accurate strain estimation concept for ultrasound elastography using iterative phase zero estimation. *IEEE Trans. Ultrason., Ferroelect., Freq. Contr.*, 46:1057–1067, 1999.

[10] T. Varghese and J. Ophir. A theoretical framework for performance chracterization of elastography: The strain filter. *IEEE Trans. Ultrason., Ferroelect., Freq. Contr.*, 44:164–172, 1997.

[11] T. Varghese, E. E. Konofagou, J. Ophir, S. K. Alam, and M. Bilgen. Direct strain estimation in elastography using spetral cross-correlation. *Ultrasound Med. Biol.*, 26:1525–1537, 2000.

[12] G. C. Carter. Coherence and time delay estimation. *Proc. IEEE*, 75:236–255, 1987.

[13] G. E. Trahey, J. W. Allison, and O. T. von Ramm. Angle independent ultrasonic detection of blood flow. *IEEE Trans. Biomed. Eng.*, 34:965–967, 1987.

[14] E. J. Chen, W. K. Jenkins, and W. D. O'Brien. The impact of various imaging parameters on ultrasonic displacement and velocity estimates. *IEEE Trans. Ultrason., Ferroelect., Freq. Contr.*, 41:293–301, 1994.

[15] I. Hein and W. D'Brien. Current time-domain methods for assessing tissue motion by analysis from reflected ultrasound echoes–a review. *IEEE Trans. Ultrason., Ferroelect., Freq. Contr.*, 40:84–102, 1993.

[16] C. M. Tempany, E. A. Stewart, N. McDannold, B. J. Quade, F. A. Jolesz, and K. Hynynen. MR imaging-guided focused ultrasound surgery of uterine leiomyomas: a feasibility study. *Radiology*, 226:897–905, 2003.

[17] B. Fallone, P. Moran, and E. Podgorsak. Noninvasive thermometry with a clinical x-ray scanner. *Med. Phys.*, 9:715–721, 1983.

[18] Y. Wan. Post-beamforming filtering for enhanced contrast resolution in medical ultrasound. *Ph.D. dissertation, The University of Minnesota*, 2010.

[19] J. A. Zagzebski. Essentials of ultrasound physics. *Mosby-Year Book, Inc*, 1996.

[20] P. de Jong, T. Arts, A. Hoeks, and R. Reneman. Determination of tissue motion velocity by correlation interpolation of pulsed ultrasonic echo signals. *Ultrasonic Imaging*, 12:84–98, 1990.

[21] G. Jacovitti and G. Scarano. Discrete time techniques for time delay estimation. *IEEE Trans. Signal Processing*, 41:525–533, 1993.

[22] T. Krouskop, F. Vinson, b. Goode, and R. Dougherty. A pulsed doppler ultrasonic system for making non-invasive measurement of the mechanical properties of soft tissue. *Journal of Rehabilitation Research and Development*, 24:1–8, 1987.

[23] R. Gill. Measurement of blood flow by ultrasound: accuracy and sources of error. *Ultrasound in Medicine and Biology*, 11:625–641, 1985.

[24] M. A. Rodriguez, R. H. Williams, and T. J. Carlow. Signal delay estimation and waveform estimation using unwrapped phase averageing. *IEEE Trans. Acoust. Speech Signal Processing*, 29:508–513, 1981.

[25] O. Kripfgans, J. Rubin, A. Hall, and J. Fowlkes. Vector doppler imaging of a spinning disc ultrasound doppler phantom. *Ultrasound in Medicine and Biology*, 32:1037–1046, 2006.

[26] P. Wells. Ultrasonic colour flow imaging. *Physics in Medicine and Biology*, 39:2113–2145, 1994.

[27] F. Viola and W. F. Walker. A spline-based algorithm for continuous time-delay estimation using sampled data. *IEEE Trans. Ultrason., Ferroelect., Freq. Contr.*, 1:80–93, 2005.

[28] R. Zahiri-Azar and S. Salcudean. Motion estimation in ultrasound images using time domain cross correlation with prior estimates. *IEEE Trans. Ultrason., Ferroelect., Freq. Contr.*, 53:1990–2000, 2006.

[29] P. G. M. de Jong, T. Arts, A. P. G. Hoeks, and R. S. Reneman. Experimental evaluation of the correlation interpolation technique to measure regional tissue velocity. *Ultrason. Imag.*, 13:84–98, 1991.

[30] I. Cespedes, Y. Huang, J. Ophir, and S. Spratt. Methods for the estimation of subsample time-delays of digitized echo signals. *Ultrasonic Imaging*, 17:142–171, 1995.

[31] R. Zahiri-Azar and S. E. Salcudean. Time-delay estimation in ultrasound echo signals using individual sample tracking. *IEEE Trans. Ultrason., Ferroelect., Freq. Contr.*, 55:2640–2650, 2008.

[32] R. Zahiri-Azar, O. Goksel, and S. E. Salcudean. Sub-sample displacement estimation from digitized ultrasound rf signals using multi-dimensional polynomial fitting of the cross-correlation function. *IEEE Trans. Ultrason., Ferroelect., Freq. Contr.*, 11:2403–2420, 2010.

[33] F. Viola and W. F. Walker. A comparison of the performance of time-delay estimators in medical ultrasound. *IEEE Trans. Ultrason., Ferroelect., Freq. Contr.*, 50:392–401, 2003.

[34] I. Cespedes, Y. Huang, J. Ophir, and S. Spratt. Methods for the estimation of subsample time-delays of digitized echo signals. *Ultrasonics Imaging*, 17:142–171, 1995.

[35] E. Konofagou and J. Ophir. Precision estimation and imaging of normal and shear components of the 3d strain tensor in elastography. *Physics in Medicine and Biology*, 45:1553–1563, 2000.

[36] K. Hoyt, F. Forsberg, and J. Ophir. Comparison of shift estimation strategies in spectral elastography. *Ultrasonics*, 44:99–108, 2006.

[37] B. J Geiman, L. N Bohs, M. E Anderson, S. M Breit, and G. E Trahey. A novel interpolation strategy for estimating subsample speckle motion. *Phys. Med. Biol.*, 45:1541–1552, 2000.

[38] X. Lai and H. Torp. Interpolation methods for time-delay estimation using cross-correlation method for blood velocity measurement. *IEEE Trans. Ultrason., Ferroelect., Freq. Contr.*, 46:277–290, 1999.

[39] S. Foster, P. Embree, and W. O'Brien. Flow velocity profile via time-domain correlation: error analysis and computer simulation. *IEEE Trans. Ultrason., Ferroelect., Freq. Contr.*, 37:164–175, 1990.

[40] P. de Jong, T. Arts, A. Hoeks, and R. Reneman. Flow velocity profile via time-domain correlation: error analysis and computer simulation. *IEEE Trans. Ultrason., Ferroelect., Freq. Contr.*, 37:164–175, 1990.

[41] H. Torp, X. M. Lai, and K. Kristoffersen. Comparison between cross correlation and auto-correlation technique in color flow imaging. *Proc. IEEE Ultrason. Symp.*, pages 1039–1042, 1993.

[42] B. J. Geiman, L. N. Bohs, M. E. Anderson, S. M. Breit, and G. E. Trahey. A comparison of algorithms for tracking sub-pixel speckle motion. *Proc. IEEE Ultrason. Symp.*, pages 1239–1242, 1997.

[43] S. Langeland, J. D'hooge, H. Torp, B. Bijnens, and P. Suetens. A simulation study on the performance of different estimators for two-dimensional velocity estimation. *Proc. IEEE Ultrason. Symp.*, pages 1859–1862, 2002.

[44] K. Hoyt, F. Forsberg, and J. Ophir. Comparison of shift estimation strategies in spectral elastography. *Ultrasonics*, 44:99–109, 2006.

[45] G. Pinton, J. Dahl, and G. Trahey. Rapid tracking of small displacements with ultrasound. *IEEE Trans. Ultrason., Ferroelect., Freq. Contr.*, 53:1103–1117, 2006.

[46] C. Sumi. Fine elasticity imaging utilizing the iterative rf-echo phase matching method. *IEEE Trans. Ultrason., Ferroelect., Freq. Contr.*, 46:158–166, 1999.

[47] H. Chen and T. Varghese. Noise analysis and improvement of displacement vector estimation from angular displacements. *Medical physics*, 35:2007–2017, 2008.

[48] G. F. Pinton and G. E. Trahey. Continuous delay estimation with polynomial splines. *IEEE Trans. Ultrason., Ferroelect., Freq. Contr.*, 53:2026–2035, 2006.

[49] S. Kim, S. R. Aglyamov, M. O'Donnell, and S. Y. Emelianov. An autocorrelation-based method for improvement of sub-pixel displacement estimation in ultrasound strain imaging. *IEEE Trans. Ultrason., Ferroelect., Freq. Contr.*, 58:838–843, 2011.

[50] E. Konofagou and J. Ophir. A new elastographic method for estimation and imaging of lateral displacements, lateral strains, corrected axial strains and poisson's ratios in tissues. *Ultrasound in Medicine and Biology*, 24:1183–1199, 1998.

[51] C. Simon, P. VanBaren, and E. S. Ebbini. Two-dimensional temperature estimation using disgnostic ultrasound. *IEEE Trans. Ultrasoni., Ferroelect., Freq. Contr.*, 45:989–1000, 1998.

[52] H. Shi and T. Varghese. Two-dimensional multi-level strain estimation for discontinuous tissue. *Physics in Medicine and Biology*, 52:389–401, 2007.

[53] D. Liu and E. S. Ebbini. Real-time 2-d temperature imaging using ultrasound. *IEEE Trans. Biomed. Eng.*, 57:1971–1974, 2010.

[54] J. Luo and E. E. Konofagou. Effects of various parameters on lateral displacement estimation in ultrasound elastography. *Ultrasound in Medicine and Biology*, 35:1352–1366, 2009.

[55] A. Basarab, H. Liebgott, and P. Delachartre. Analytic estimation of subsample spatial shift using the phases of multidimensional analytic signals. *IEEE Transactions on Image Processing*, 18:440–447, 2009.

[56] F. Viola, R. Coe, K. Owen, D. Guenther, and W. Walker. Multi-dimensional spline-based estimator (muse) for motion estimation: Algorithm development and initial results. *Annals of Biomedical Engineering*, 36:1942–1960, 2008.

[57] R. Lopata, M. Nillesena, H. Hansena, I. Gerritsa, T. J., and C. de Korte. Performance evaluation of methods for two-dimensional displacement and strain estimation using ultrasound radio frequency data. *Ultrasound in medicine and biology*, 35:796–812, 2009.

[58] E. S. Ebbini. Phase-coupled two-dimensional speckle tracking algorithm. *IEEE Trans. Ultrason., Ferroelect., Freq. Contr.*, 53:972–990, 2006.

[59] X. Chen, M. Zohdy, S. Y. Emelianov, and M. O'Donnell. Lateral speckle tracking using synthetic lateral phase. *IEEE Trans. Ultrason., Ferroelect., Freq. Contr.*, 51:540–550, 2009.

[60] J. A. Jensen. Field: a program for simulating ultrasound systems. *10th Nordic-Baltic Conf. Biomed. Imag.*, 4:351–353, 1996.

[61] M. O'Donnella, A. R. Skovoroda, B. M. Shapo, and S. Y. Emelianov. Internal displacement and strain imaging using ultrasonic speckle tracking. *IEEE Trans. Ultrason., Ferroelect., Freq. Contr.*, 41:314–325, 1994.

[62] J. Greenleaf, M. Fatemi, and M. Insana. Selected methods for imaging elastic properties of biological tissues. *Annual Review of Biomedical Engineering*, 5:57–78, 2000.

[63] S. Emelianov, X. Chen, M. ODonnell, B. Knipp, D. Myers, T. Wakefield, and J. Rubin. Triplex ultrasound: Elasticity imaging to age deep venous thrombosis. *Ultrasound in Medicine and Biology*, 28:757–767, 2002.

[64] T. Varghese, J. Zagzebski, and J. Jee. Elastography imaging of thermal lesion in the liver in vivo following radio frequency ablation: Preliminary results. *Ultrasound in Medicine and Biology*, 28:1467–1473, 2002.

[65] E. Konofagou, J. Dhooge, and J. Ophir. Myocardial elastography - a feasibility study in vivo. *Ultrasound in Medicine and Biology*, 28:475–482, 2002.

[66] A. Thitaikumar, L. Mobbs, C. Kraemer-Chant, B. Garra, and J. Ophir. Breast tumor classification using axial shear strain elastography: a feasibility study. *Physics in Medicine and Biology*, 53:4809–4823, 2008.

[67] K. Hoyt, K. Parker, and J. Rubens. Real-time shear velocity imaging using sonoelastographic techniques. *Ultrasound in Medicine and Biology*, 33:1086–1097, 2007.

[68] A. Lorenz, H. Sommerfeld, M. Schurmann, S. Philippou, T. Senge, and H. Ermert. A new system for the acquisition of ultrasonic multicompression strain images of the human prostate in vivo. *IEEE Trans. Ultrason., Ferroelect., Freq. Contr.*, 46:1147–1154, 1999.

[69] A. Skovoroda, S. Emelianov, and M. ODonnell. Tissue elasticity reconstruction based on ultrasonic displacement and strain images. *IEEE Trans. Ultrason., Ferroelect., Freq. Contr.*, 42:747–765, 1995.

[70] M. Lubinski, S. Emelianov, and M. ODonnell. Speckle tracking methods for ultrasonic elasticity imaging using short-time correlation. *IEEE Trans. Ultrason., Ferroelect., Freq. Contr.*, 46:82–96, 1999.

[71] D. E. Robinson, F. Chen, and L. S. Wilson. Measurement of velocity of propogation from ultrasonic pulse-echo data, 3-d flow velocity vector estimation with a triple-beam lens transducer-experimental. *Ultrasound Med. Biol.*, 8:413–420, 1982.

[72] C. Kasai, K. Namekawa, A. Koyano, and R. Omoto. Real-time two-dimensional blood flow imaging using autocorrelation technique. *IEEE Trans. Sonics, Ultrason.*, 32:458–463, 1985.

[73] P. M. Embree and W. D. O'Brien. Volumetric blood flow via time-domain correlation: Experimental verification. *IEEE Trans. Ultrasoni., Ferroelect., Freq. Contr.*, 37:176–189, 1990.

[74] T. Loupas, J. T. Powers, and R. W. Gill. An axial velocity estimator for ultrasound blood flow imaging, based on a full evaluation of the doppler equation by means of a two-dimensional autocorrelation approach. *IEEE Trans. Ultrason., Ferroelect., Freq. Contr.*, 42:672–688, 1995.

[75] F. Yeung, S. F. Levinson, D. Fu, and K. J. Parker. Feature-adaptive motion tracking of ultrasound image sequences using a deformable mesh. *IEEE Trans. Medical Imaging*, 17:945–956, 1998.

[76] H. Kanai, Y. Koiwa, and J. Zhang. Real-time measurements of local myocardium motion and arterial wall thickening. *IEEE Trans. Ultrason., Ferroelect., Freq. Contr.*, 46:1229–1241, 1999.

[77] S. I. Rabben, S. Bjaerum, V. Soerhus, and H. Torp. Ultrasound-based vessel wall tracking: an auto-correlation technique with rf center frequency estimation. *Ultrasound in Medicine and Biology*, 28:507–517, 2002.

[78] S. Golemati, A. Sassano, M. Leve, A. Bharath, S. Dhanjil, and A. Nicolaides. Carotid artery wall motion estimated from b-mode ultrasound using region tracking and block matching. *Ultrasound in Medicine and Biology*, 29:387–399, 2003.

[79] M. Cinthio, A. Ryden Ahlgren, T. Jansson, A. Eriksson, H. W. Person, and L. Kjell. Evaluation of an ultrasonic echo-tracking method for measuring of arterial wall movement in two dimensions. *IEEE Trans. Ultrason., Ferroelect., Freq. Contr.*, 52:1300–1311, 2005.

[80] W. Walker, F. Fernandez, and L. Negron. A method of imaging viscoelastic parameters with acoustic radiation force. *Physics in Medicine and Biology*, 45:1437–1447, 2000.

[81] K. Nightingale, M. L. Palmeri, R. W. Nightingale, and G. E. Trahey. On the feasibility of remote palpation using acoustic radiation force. *J. Acoust. Soc. Am.*, 110:625–634, 2001.

[82] F. Viola and W. F. Walker. Radiation force imaging of viscoelastic properties with reduced artifacts. *IEEE Trans. Ultrason., Ferroelect., Freq. Contr.*, 50:736–742, 2003.

[83] R. Nelson M. Palmeri B. Fahey, K. Nightingale and G. Trahey. Acoustic radiation force impulse imaging of the abdomen: Demonstration of feasibility and utility. *Ultrasound in Medicine and Biology*, 31:1185–1198, 2005.

[84] A. Sarvazyan, O. Rudenko, S. Swanson, J. Fowlkes, and S. Y. Emelianov. Shear wave elasticity imaging: a new ultrasonic technology of medical diagnostics. *Ultrasound in Medicine and Biology*, 24:1419–35, 1998.

[85] R. Muthupillai T. Oliphant R. Ehman V. Dutt, R. Kinnick and J. Greenleaf. Acoustic shear-wave imaging using echo ultrasound compared to magnetic resonance elastography. *Ultrasound in Medicine and Biology*, 26:397–403, 2000.

[86] L. Sandrin, M. Tanter, D. Cassereau, S. Catheline, and M. Fink. Low-frequency shear wave beam forming in time-resolved 2d pulsed elastography. *Proceedings of the IEEE Ultrasonics Symposium*, 2:1803–1808, 2000.

[87] S. Chen, M. Urban, C. Pislaru, R. Kinnick, Y. Zheng, A. Yao, and J. Greenleaf. Shearwave dispersion ultrasound vibrometry (sduv) for measuring tissue elasticity and viscosity. *IEEE Trans. Ultrason., Ferroelect., Freq. Contr.*, 56:55–62, 2009.

[88] T. deffieux, J. Gennisson, J. bercoff, and M. Tanter. On the effects of reflected waves in transient shear wave elastography. *IEEE Trans. Ultrason., Ferroelect., Freq. Contr.*, 58:2032–2035, 2011.

[89] J. Luo, R. X. Li, and E. E. Konofagou. Pulse wave imaging of the human carotid artery: an in vivo feasibility study. *IEEE Trans. Ultrason., Ferroelect., Freq. Contr.*, 59:174–181, 2012.

[90] E. Hermeling, K. Reesink, R. Reneman, and A. Hoeks. Measurement of local pulse wave velocity: effects of signal processing on precision. *Ultrasound in Medicine and Biology*, 33:774–781, 2007.

[91] K. Kaluzynski, C. Xunchang, S. Emelianov, A. Skovoroda, and M. ODonnell. Strain rate imaging using two-dimensional speckle tracking. *IEEE Trans. Ultrason., Ferroelect., Freq. Contr.*, 48:1111–1123, 2001.

[92] U. Techavipoo, Q. Chen, T. Varghese, and J. Zagzebski. Estimation of displacement vectors and strain tensors in elastography using angular insonifications. *IEEE Trans. Medical Imaging*, 23:1479–1489, 2004.

[93] H. Eskandari, S. Salcudean, and R. Rohling. Tissue strain imaging using a wavelet transform-based peak search algorithm. *IEEE Trans. Ultrason., Ferroelect., Freq. Contr.*, 54:1118–1130, 2007.

[94] H. Ribbers, R. Lopata, S. Holewijn, G. Pasterkamp, J. Blankensteijn, and C. de Korte. Noninvasive two-dimensonal strain imaging of arteries: validation in phantoms and preliminary experience in carotid arteries in vivo. *Ultrasound in Medicine and Biology*, 33:530–540, 2007.

[95] L. Lvstakken, S. Bjaerum, D. Martens, and H. Torp. Blood flow imaginga new realtime, 2-d flow imaging technique. *IEEE Trans. Ultrason., Ferroelect., Freq. Contr.*, 53:289–299, 2006.

[96] O. Bonnefous and P. Pesque. Time domain formulation of pulse-doppler ultrasound and blood velocity estimation by cross correlation. *Ultrason. Imag.*, 8:73–85, 1986.

[97] L. N. Bohs, B. H. Friemel, B. A. Mcdermott, and G. E. Trahey. A real-time system for quantifying and displaying two-dimensional velocities using ultrasound. *Ultrasound Med. Biol.*, 19:751–761, 1993.

[98] X. Lu, H. Lee, and E. S. Ebbini. Phase-coupled two-dimensional speckle tracking method. *Proc. IEEE Ultrason. Symp.*, pages 1931–1934, 2003.

[99] Y. Wan, D. Liu, and E. S. Ebbini. Simultaneous imaging of tissue motion and flow velocity using 2d phase-coupled speckle tracking. *Proc. IEEE Ultrason. Symp.*, pages 487–490, 2010.

[100] J. Dahl, G. Pinton, M. Palmeri, V. Agrawal, K. Nightingale, and G. Trahey. A parallel tracking method for acoustic radiation force impulse imaging. *IEEE Trans. Ultrason., Ferroelect., Freq. Contr.*, 54:301–312, 2007.

[101] J. Bercoff, M. Tanter, M. Muller, and M. Fink. Study of viscous and elastic properties of soft tissues using supersonic shear imaging. *Proceedings of the IEEE Ultrasonic Symposium*, 2003.

[102] M. Rao, Q. Chen, H. Shi, T. Varghese, E. Madsen, J. Zagzebski, and T. Wilson. Normal and shear strain estimation using beam steering on linear-array transducers. *Ultrasound in Medicine and Biology*, 33:57–66, 2007.

[103] S. Catheline, J.-L. Gennisson, G. Delon, and M. Fink. Measurement of viscoelastic properties of homogeneous soft solid using transient elastography: An inverse problem approach. *J. Acoust. Soc. Am.*, 116:3734–3741, 2004.

[104] L. Sandrin, M. Tanter, D. Cassereau, S. Catheline, and M. Fink. ultrafast compound imaging for 2d motion vector estimation: Application to transient elastography. *IEEE Trans. Ultrason., Ferroelect., Freq. Contr.*, 49:1363–1374, 2002.

[105] L. Capineri, M. Scabia, and L. Masotti. Vector doppler: spatial sampling analysis and presentation techniques for real time systems. *Journal of Electronic Imaging*, 12:489–498, 2003.

[106] S. Wang, W. Lee, J. Provost, L. Jianwen, and E. Konofagou. A composite high-frame rate system for clinical cardiovascular imaging. *IEEE Trans. Ultrason., Ferroelect., Freq. Contr.*, 55:2221–2233, 2008.

[107] C. Papadacci, M. Pernot, M. Couade, M. Fink, and M. Tanter. High-contrast ultrafast imaging of the heart. *IEEE Trans. Ultrason., Ferroelect., Freq. Contr.*, 2:288–301, 2014.

[108] M. Tanter and M. Fink. Ultrafast imaging in biomedical ultrasound. *IEEE Trans. Ultrason., Ferroelect., Freq. Contr.*, 61:102–119, 2014.

[109] I. Cespedes, Y. Huang, J. Ophir, and S. Spratt. Methods for estimation of subsample time delays of digitized echo signals. *Ultrason. Imag.*, 17:142–171, 1995.

[110] F. Viola and W. F. Walker. Comptationally efficient spline-based time delay estimation. *IEEE Trans. Ultrason., Ferroelect., Freq. Contr.*, 55:2084–2091, 2008.

[111] S. L. Marple. Estimating group delay and phase delay via discrete-time analytic cross-correlation. *IEEE Trans. Signal Processing*, 47:2604–2607, 1999.

[112] R. F. Wagner, M. F. Insana, and S. W. Smith. Fundamental correlation lengths of coherent speckle in medical ultrasonic images. *IEEE Trans. Ultrason., Ferroelect., Freq. Contr.*, 35:34–44, 1988.

[113] M. Almekkawy, Y. Adibi, F. Zheng, M. Chirala, and E. Ebbini. Two-dimensional speckle tracking using zero phase crossing with riesz transform. *J. Acoust. Soc. Am.*, 136, 2015.